

UNCLASSIFIED

AD NUMBER
AD847062
NEW LIMITATION CHANGE
TO Approved for public release, distribution unlimited
FROM Distribution authorized to U.S. Gov't. agencies and their contractors; Critical Technology; JAN 1969. Other requests shall be referred to Arnold Engineering Development Center, Arnold AFB, TN.
AUTHORITY
AEDC USAE ltr, 2 Oct 1972

THIS PAGE IS UNCLASSIFIED

AEDC-TR-69-36



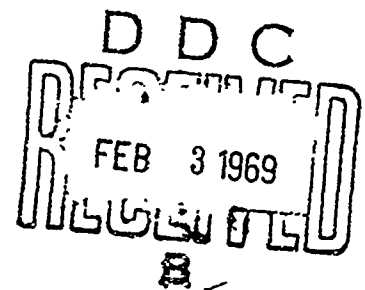
AD847062

**A STUDY OF REAL-GAS EFFECTS
ON BLU'NED CONE FLOWS**

**C. E. Wittliff and T. R. Sundaram
Cornell Aeronautical Laboratory, Inc.**

Buffalo, New York

January 1969



This document is subject to special export controls and each transmittal to foreign governments or foreign nationals may be made only with prior approval of Arnold Engineering Development Center (AETS), Arnold Air Force Station, Tennessee 37389.

**ARNOLD ENGINEERING DEVELOPMENT CENTER
AIR FORCE SYSTEMS COMMAND
ARNOLD AIR FORCE STATION, TENNESSEE**

A STUDY OF REAL-GAS EFFECTS
ON BLUNTED CONE FLOWS

C. E. Wittliff and T. R. Sundaram
Cornell Aeronautical Laboratory, Inc.
Buffalo, New York

This document is subject to special export controls and each transmittal to foreign governments or foreign nationals may be made only with prior approval of Arnold Engineering Development Center (AETS), Arnold Air Force Station, Tennessee 37389.

<u>Figure</u>		<u>Page</u>
26	Correlation of Surface Pressure Distributions for Equilibrium Flow when Free-Stream Temperature is not Duplicated	131
27	Variation of the Dissociation Energy and Dissociation Fraction (in the Body Stream Tube) with Free-Stream Velocity for $h = 250,000$ ft	132
28	Influence of Real-Gas Effects on the Downstream Influence of a Blunt Nose for a Spherically Blunted Slender Cone	133
29	Shock Shape for the Nonequilibrium Flow Past a Spherically Blunted Cone	134
30	Surface Pressure Distribution for the Nonequilibrium Flow Past a Spherically Blunted Cone	135

ABSTRACT

This report presents the results of a study of the combined effects of nose bluntness and real-gas phenomena on blunted slender body flows, with particular emphasis on the flows past spherically blunted cones. One of the primary objectives of the study has been to assess the effects of not matching all the similitude parameters in hypervelocity test flows about the slender bodies that are under consideration. In the first phase of the study, direct comparisons between the flight and wind-tunnel flow fields are made for a blunted slender cone for several flight cases by using a stream-tube computer program. In this part of the study the pressure distribution on the surface of the cone is assumed to be insensitive to nonequilibrium effects. In the second phase of the study, the influence of real-gas effects on blunted slender body flow fields is studied analytically by using a thin-shock-layer approach. It is found that real-gas effects on the pressure distribution and the shock shape for a blunted slender cone are small for the range of free-stream conditions of interest. The implications of various existing similitude laws to hypervelocity testing are discussed briefly, and a restricted similitude applicable to real-gas flows over blunted slender bodies is derived.

This document is subject to special export controls and each transmittal to foreign governments or foreign nationals may be made only with prior approval of Arnold Engineering Development Center (AEDC), Arnold Air Force Station, Tennessee 37389.

NOTICES

When U. S. Government drawings, specifications, or other data are used for any purpose other than a definitely related Government procurement operation, the Government thereby incurs no responsibility nor any obligation whatsoever, and the fact that the Government may have formulated, furnished, or in any way supplied the said drawings, specifications, or other data, is not to be regarded by implication or otherwise, or in any manner licensing the holder or any other person or corporation, or conveying any rights or permission to manufacture, use, or sell any patented invention that may in any way be related thereto.

Qualified users may obtain copies of this report from the Defense Documentation Center.

References to named commercial products in this report are not to be considered in any sense as an endorsement of the product by the United States Air Force or the Government.

ACQUISITION FOR	
REPORT	WRITE SECTION <input type="checkbox"/>
DOC	DIFF SECTION <input checked="" type="checkbox"/>
UNANNOUNCED	<input type="checkbox"/>
JUSTIFICATION	
BY	
DISTRIBUTION/AVAILABILITY CODES	
DIST.	ATAIL and/or SPECIAL
2	

CONTENTS

	Page
FOREWORD	ii
ABSTRACT	iii
LIST OF ILLUSTRATIONS	vii
LIST OF TABLES	ix
NOMENCLATURE	xi
I. INTRODUCTION	1
II. COMPARISON OF WIND TUNNEL FLOWS WITH FLIGHT CONDITIONS	3
III. GENERAL FEATURES OF BLUNT-NOSED SLENDER BODY FLOWS	15
IV. REVIEW OF HYPERSONIC SIMILITUDES	20
A. INVISCID FLOW	20
B. VISCOUS FLOW	23
V. COMPARISON OF FLOWS OVER BLUNTED SLENDER CONES FOR PARTIALLY SIMULATED CONDITIONS	24
A. INTRODUCTION	24
B. METHOD OF FLOW FIELD ANALYSIS	25
1. General Approach	25
2. Blunted Cone Pressure Distributions	26
3. Streamtube Computer Program	28
4. Conical Shock Calculations	28
C. RESULTS OF CALCULATIONS	29
1. Equilibrium Stagnation-Point Conditions	29
2. Body Streamtube, Case I ($U_{\infty} = 15,000$ fps)	32
3. Conical-Shock Calculations, Case I ($U_{\infty} = 15,000$ fps)	34
4. Body Streamtube, Case II ($U_{\infty} = 25,000$ fps)	35
5. Conical-Shock Calculations, Case II ($U_{\infty} = 25,000$ fps)	36
6. Body Streamtube, Case III ($U_{\infty} = 35,000$ fps)	38
7. Conical-Shock Calculations, Case III ($U_{\infty} = 35,000$ fps)	40
D. DRAG, SKIN-FRICTION AND HEAT TRANSFER COMPARISONS	41
1. Pressure Drag	42
2. Viscous Drag	42
3. Skin Friction and Heat Transfer	43
E. SUMMARY	45
VI. ANALYSIS OF THE COMBINED EFFECTS OF NOSE BLUNTNESS AND NONEQUILIBRIUM ON SLENDER-BODY FLOWS	47
A. INTRODUCTORY REMARKS	47
B. REVIEW OF BLUNT NOSED SLENDER-BODY FLOWS	47
C. FORMULATION OF A THEORETICAL MODEL	51
D. RESTRICTED SIMILITUDE APPLICABLE TO REAL-GAS FLOWS PAST BLUNTED SLENDER BODIES	59
E. ANALYSIS OF BLUNT NOSED SLENDER BODY	70
1. The Basic Equations	71
2. Evaluation of the Integral in Eq. VI. 57	76
3. Solution for a Spherically Blunted Cone	81

	F. VISCOUS EFFECTS	88
	G. SUMMARY AND DISCUSSION OF THE RESULTS	93
VII.	CONCLUSIONS	96
	REFERENCES	98

ILLUSTRATIONS

<u>Figure</u>		<u>Page</u>
1	Altitude-Velocity Map of Flight Regime of Interest	105
2	Altitude-Velocity Map Showing Wind Tunnel Performance	106
3	Blunt-Nose Flow Regimes	107
4	Blunt-Nose Chemical-Kinetic Regimes	108
5	Pressure Distribution on Spherical Nose	109
6	Correlation of Ideal Gas and Real Air Pressure Distributions on Spherically Blunted Cones	110
7	Pressure Distribution Along Conical Afterbody at Various Free-Stream Mach Numbers	111
8	Temperature Distribution on 9° Blunted Cone at $U_{\infty} = 15,000$ fps	112
9	Density Distribution on 9° Blunted Cone at $U_{\infty} = 15,000$ fps	113
10	Nitric Oxide Distribution on 9° Blunted Cone at $U_{\infty} = 15,000$ fps	114
11	Atomic Oxygen Distribution on 9° Blunted Cone at $U_{\infty} = 15,000$ fps	115
12	Temperature Distribution on 9° Blunted Cone at $U_{\infty} = 25,000$ fps	116
13	Density Distribution on 9° Blunted Cone at $U_{\infty} = 25,000$ fps	117
14	Molecular Nitrogen Distribution on 9° Blunted Cone at $U_{\infty} = 25,000$ fps	118
15	Nitric Oxide Distribution on 9° Blunted Cone at $U_{\infty} = 25,000$ fps	119
16	Atomic Nitrogen Distribution on 9° Blunted Cone at $U_{\infty} = 25,000$ fps	120
17	Temperature Distribution on 9° Blunted Cone at $U_{\infty} = 35,000$ fps	121
18	Density Distribution on 9° Blunted Cone at $U_{\infty} = 35,000$ fps	122
19	Atomic Nitrogen Distribution on 9° Blunted Cone at $U_{\infty} = 35,000$ fps	123
20	Atomic Nitrogen Ion Distribution on 9° Blunted Cone at $U_{\infty} = 35,000$ fps	124
21a	Comparison of Heat Transfer Distribution on 9° Blunted Cone at $U_{\infty} = 25,000$ fps	125
21b	Comparison of Skin Friction Distribution on 9° Blunted Cone at $U_{\infty} = 25,000$ fps	126
22	Schematic Representation of the Flow Field	127
23	Comparison of the Dissociation Fractions on the Body and Immediately Behind the Shock Wave for Equilibrium Flow	128
24	Comparison of the Density on the Body with the Free-Stream Density	129
25	Correlation of Shock Shapes in Real-Gas Flows when Free-Stream Temperature is not Duplicated	130

<u>Figure</u>		<u>Page</u>
26	Correlation of Surface Pressure Distributions for Equilibrium Flow when Free-Stream Temperature is not Duplicated	131
27	Variation of the Dissociation Energy and Dissociation Fraction (in the Body Stream Tube) with Free-Stream Velocity for $h = 250,000$ ft	132
28	Influence of Real-Gas Effects on the Downstream Influence of a Blunt Nose for a Spherically Blunted Slender Cone	133
29	Shock Shape for the Nonequilibrium Flow Past a Spherically Blunted Cone	134
30	Surface Pressure Distribution for the Nonequilibrium Flow Past a Spherically Blunted Cone	135

TABLES

<u>Table</u>		<u>Page</u>
II-1	Comparison of Flight and Hypothetical Wind Tunnel Conditions, Case I	3
II-2	Comparison of Flight and Hypothetical Wind Tunnel Conditions, Case II	5
II-3	Comparison of Flight and Hypothetical Wind Tunnel Conditions, Case III	6
II-4	Nozzle Nonequilibrium Effects in Hypothetical Wind Tunnel, Cases I - III	6
II-5	Velocity-Altitude Conditions in Full-Duplication Region	7
II-6	Nozzle Nonequilibrium Effects in Hypothetical Wind Tunnel, Cases IV - VIII	8
II-7	Comparison of Flight and 2000-atm Wind Tunnel Conditions	9
II-8	Comparison of Flight and 2000-atm Wind Tunnel Conditions, Case VII	10
II-9	Comparison of Flight and 2000-atm Wind Tunnel Conditions, Case VIII	10
II-10	Comparison of Equilibrium Conditions Behind a Normal Shock Wave in Flight and 2000-atm Wind Tunnel	11
II-11	Comparison of Frozen-Flow Conditions Behind a Normal Shock Wave in Flight and 2000-atm Wind Tunnel	12
II-12	Nozzle Nonequilibrium Effects in 2000-atm Wind Tunnel	13
II-13	Equilibrium and Frozen Flow Conditions Behind a Normal Shock Wave in a Nonequilibrium 2000-atm Wind Tunnel	14
V-1	Comparison of Stagnation-Point Conditions, Case I	30
V-2	Comparison of Stagnation-Point Conditions, Case II	30
V-3	Comparison of Stagnation-Point Conditions, Case III	31
V-4	Comparison of Free-Stream and Conical-Shock Conditions, Case I	34
V-5	Comparison of Free-Stream and Conical-Shock Conditions, Case II	37
V-6	Comparison of Flight and Wind-Tunnel Conditions, Case III	38

<u>Table</u>		<u>Page</u>
V-7	Comparison of Conical-Shock Conditions, Case III	40
V-8	Entropy Layer Swallowing Distance	41
V-9	Pressure Drag Coefficients	42
V-10	Stagnation-Point Heat Transfer	45

NOMENCLATURE

a	speed of sound
c	correction factor
C_μ	Chapman-Rubens viscosity constant
C_D	drag coefficient
C_f	skin-friction coefficient
C_h	heat transfer coefficient
C_p	pressure coefficient, specific heat at constant pressure
D	drag, dissociation energy
d	diameter
e	internal energy
h	enthalpy
h_s	static enthalpy
χ_n	bluntness parameter
ξ	nose drag coefficient
L	length
M	Mach number
p	pressure
Pr	Prandtl number
\dot{q}	heat transfer rate
R	gas constant, radius
r	radius
S	entropy, distance along body surface
T	temperature
\bar{U}	viscous parameter
u	velocity
v	velocity
X	axial distance
x	axial coordinate
X_i	species concentrations
Y	radial distance

r	radial coordinate
\bar{z}	compressibility factor
α	dissociation fraction
β	nose bluntness parameter
γ	specific heat ratio
Δ	bow shock standoff distance
δ	boundary layer
ϵ	$\frac{\gamma-1}{\gamma+1}$
ζ	see Eq. VI-73
θ_c	cone half angle
λ	mean-free-path
μ	viscosity
ν	kinematic viscosity
ρ	density
σ	shock angle
τ	characteristic thickness ratio, shear stress
χ	viscous interaction parameter

Subscripts

adw	adiabatic wall conditions
\bar{b}	base of body
b	conditions at body
e	conditions at outer edge of boundary layer or entropy layer
N, n	nose of body
o	total or stagnation conditions
p	sonic point conditions
s	conditions behind shock wave
st	stagnation-point conditions
w	wall conditions
∞	free-stream conditions

SECTION I INTRODUCTION

In a recent study of hypervelocity flows and similitudes¹ it was pointed out that, in the combined presence of nonequilibrium flow and nose bluntness effects, similitude between two slender body flows is theoretically impossible. That is, the similitude requirements dictate complete duplication of ambient thermo-chemical state, free-stream velocity and vehicle size. However, at high flight velocities and low altitudes it is impossible to duplicate the ambient thermo-chemical state in existing wind tunnels. In view of this state of affairs, it is necessary that the similitude requirements for hypervelocity flows be carefully examined from the standpoint of delineating the more important similarity parameters and determining the degree to which the less important similitude requirements can be relaxed. For the hypervelocity flight regime considered in the study reported in Ref. 1, it was found that there do not exist sufficient experimental data or theoretical solutions to evaluate the sensitivity of various flow quantities to variations in the similitude parameters or to fully determine whether some parameters are less important than others. Thus, the purpose of the present investigation has been to obtain new theoretical solutions for blunted slender bodies with the specific objective of studying the effects of relaxing certain similitude requirements.

There are two phases to the present work. The first phase is concerned with a direct comparison of flight and wind-tunnel flow fields about a blunted slender cone. For this purpose, the hypothetical wind-tunnel performance defined in Ref. 1 has been used. The comparisons are made at several flight conditions for which complete duplication can not be achieved in the wind tunnel, i. e. at low altitudes. Partial results of the study have been reported in Ref. 2. The second phase of the work is concerned with flight conditions at higher altitudes where it is assumed that a wind tunnel could fully duplicate the ambient altitude thermodynamic state if there were no nozzle nonequilibrium effects. Here the emphasis is on an investigation of nonequilibrium flows about blunted slender bodies within the framework of thin shock layer theory and the blast-wave analogy. Both studies are restricted

to bodies at zero angle of attack.

In the following Section (Sec. II) of this report, the flight regime of interest will be defined and related to wind-tunnel performance capabilities. Because of the limitations of existing wind tunnels, a hypothetical wind-tunnel performance is defined which minimizes nozzle nonequilibrium effects over most of the flight region. Test conditions in the hypothetical wind tunnel are compared with flight conditions for various velocities and altitudes. These comparisons include estimates of the effects of nonequilibrium phenomena on the nozzle expansion.

In Sec. III, some of the general features of the flow about blunt-nosed slender bodies are discussed with particular attention to rarefaction effects, viscous interactions and flow chemistry. This is followed by a brief review (Sec. IV) of the similitudes for such flows. The next two sections (Sec. V, VI) are concerned with the two studies carried out as part of this investigation. The concluding section summarizes the general findings of these studies.

SECTION II

COMPARISON OF WIND TUNNEL FLOWS WITH FLIGHT CONDITIONS

In this section the flight region of interest will be defined and related to wind tunnel performance requirements. For the purposes of later comparisons of flight and wind-tunnel flow fields, a hypothetical wind tunnel performance is postulated. Test section conditions in this hypothetical wind tunnel are compared to flight conditions. The effects of nonequilibrium nozzle flow on wind-tunnel test conditions are estimated. Finally, the test conditions available in present-day wind tunnels are compared with flight conditions for several velocities and altitudes.

The hypervelocity flight regime of interest in this study is the altitude range from 50,000 ft. to 250,000 ft. for velocities from 10,000 fps to 36,000 fps (see Fig. 1). This regime encompasses all of the continuous flight corridor lying above 10,000 fps velocity and below 250,000 ft. altitude and all of the reentry corridor for manned satellites and lunar vehicles (except portions of skip trajectories). These flight regions are also shown in Fig. 1. This altitude-velocity map further serves to define the range of values for various similarity parameters and will be referred to frequently in subsequent sections.

The severe requirements that duplication of ambient altitude conditions at hypersonic speeds imposes on a wind tunnel are illustrated in Fig. 2. This altitude-velocity map shows the nozzle reservoir pressures and temperatures necessary for duplicating flight conditions assuming an isentropic expansion of real air in thermodynamic equilibrium. It should be noted that there are few facilities presently operating at reservoir pressures greater than 2000 atm; therefore, reservoir pressures above 4000 atm have not been shown in Fig. 2. In existing facilities velocities greater than 20,000 fps can be obtained, but pressure, temperature and density for altitudes below 250,000 ft. cannot be duplicated simultaneously.

In order to assess the magnitudes of the mismatches that can be expected in a wind tunnel, it was necessary to specify a wind-tunnel performance capability. This was done with due regard to nozzle-flow nonequilibrium effects. In descriptions of recently proposed new facilities, several authors^{3,4} have

adopted a maximum entropy criterion for minimizing nonequilibrium effects in the nozzle flow. This criterion is based on the fact that the nonequilibrium effects on the expansion of air from a stagnant reservoir to high velocity can be correlated in terms of entropy^{5,6}. While specifying a maximum entropy of, say, $S/R = 31.5$ implies that the nonequilibrium effects will be small in the nozzle flow, it also limits the maximum altitude at which full duplication of ambient conditions can be achieved to 190,000 ft. The conclusion is that, if air is expanded in a nozzle from a high temperature, high pressure reservoir, nonequilibrium effects cannot be eliminated when testing at high-altitude, hypervelocity conditions.

The hypothetical wind-tunnel capability postulated in the present study^{1,2} is defined by the full-duplication boundary line shown in Fig. 2. Above this full-duplication boundary, it is assumed that both flight velocity and ambient altitude conditions could be duplicated in the test section if the nozzle expansion remained in thermochemical equilibrium. Below this boundary line it is assumed that the flight velocity and only one of the ambient altitude conditions (e.g., density-altitude or free-stream temperature) can be duplicated. In Ref. 1 it was shown that nozzle nonequilibrium effects on test section velocity and density are negligible below the full-duplication boundary for this hypothetical wind tunnel. Estimates of the nonequilibrium effects on pressure, temperature and Mach number in this partial simulation region are presented in this section.

Above the full-duplication boundary of Fig. 2, duplication of velocity and ambient altitude thermochemical state is compromised by nozzle flow nonequilibrium. The effect on velocity was indicated in Ref. 1. Nonequilibrium effects on the test conditions will be discussed in greater detail later in this section.

For the flow phenomena that are of interest in the present study, the more important parameters to be duplicated in the partial simulation region are the density-altitude (i.e., the free-stream density) and the flight velocity. These two parameters insure the duplication of the fluxes of free-stream mass, momentum and energy provided that $M_\infty \sin \sigma$ (where σ is the shock angle) is sufficiently large so the bow shock wave is everywhere strong.

In Section V a comparison is made of flight and wind-tunnel flow fields about a blunted slender cone. The three flight conditions considered in that study are velocities of 15,000 fps and 25,000 fps at an altitude of 80,000 ft. and 35,000 fps at 180,000 ft. altitude. It can be seen in Fig. 2 that these conditions are substantially beyond the duplication capabilities of the hypothesized wind tunnel. From the performance capability hypothesized in Fig. 2, it is possible to determine the wind-tunnel test conditions when the flight velocity and ambient density altitude are duplicated under the assumption that the nozzle expansion is isentropic and in thermochemical equilibrium. The validity of the isentropic-equilibrium assumption is then evaluated. The flight and wind-tunnel conditions and related parameters for the three cases are compared in the following tables for the case of an equilibrium nozzle flow.

Table II-1

COMPARISON OF FLIGHT AND HYPOTHETICAL WIND TUNNEL CONDITIONS

Case I: $U_{\infty} = 15,000$ fps, 80,000 ft Alt.

PARAMETER	FLIGHT	WIND TUNNEL
VELOCITY, U_{∞} (fps)	15,000	15,000
DENSITY, ρ_{∞} (ama)	3.420×10^{-2}	3.420×10^{-2}
PRESSURE, p_{∞} (atm)	2.765×10^{-2}	8.134×10^{-2}
TEMPERATURE, T_{∞} ($^{\circ}$ K)	220.9	650.0
MACH NUMBER, M_{∞}	15.34	9.042
TOTAL ENTHALPY, $\frac{H_0}{R}$ ($^{\circ}$ K)	3.716×10^4	3.869×10^4
ENTROPY, S/R	26.44	29.14

Table II-2

COMPARISON OF FLIGHT AND HYPOTHETICAL WIND TUNNEL CONDITIONS

Case II: $U_{\infty} = 25,000$ fps, 80,000 ft Alt.

PARAMETER	FLIGHT	WIND TUNNEL
VELOCITY, U_{∞} (fps)	25,000	25,000
DENSITY, ρ_{∞} (ama)	3.420×10^{-2}	3.420×10^{-2}
PRESSURE, p_{∞} (atm)	2.765×10^{-2}	1.513×10^{-1}
TEMPERATURE, T_{∞} ($^{\circ}$ K)	220.9	1209
MACH NUMBER, M_{∞}	25.57	11.25
TOTAL ENTHALPY, $\frac{H_0}{R}$ ($^{\circ}$ K)	1.019×10^5	1.056×10^5
ENTROPY, S/R	26.44	30.99

Table II-3
COMPARISON OF FLIGHT AND HYPOTHETICAL WIND TUNNEL CONDITIONS
Case III: $U_\infty = 35,000$ fps, 180,000 ft ALT.

PARAMETER	FLIGHT	WIND TUNNEL
VELOCITY, U_∞ (fps)	35,000	35,000
DENSITY, ρ_∞ (ama)	4.413×10^{-4}	4.413×10^{-4}
PRESSURE, p_∞ (atm)	4.292×10^{-4}	6.135×10^{-4}
TEMPERATURE, T_∞ (°K)	265.9	380.0
MACH NUMBER, M_∞	32.63	27.34
TOTAL ENTHALPY, $\frac{H_0}{R}$ (°K)	1.990×10^5	1.954×10^5
ENTROPY, S/R	31.25	32.15

It is seen that, in the first two cases, appreciable differences in free-stream pressure, temperature and Mach number exist between the flight and wind-tunnel conditions. Along the lower-boundary of the altitude-velocity map in Fig. 2, the mismatch in static temperature can be as great a factor of 7 for the wind-tunnel performance hypothesized here. This emphasizes the importance of understanding the effects of partial simulation.

Because the free-stream conditions in the wind tunnel tabulated above have been computed under the assumption of an isentropic, equilibrium nozzle flow, it is pertinent to investigate the effects the nonequilibrium phenomena would have on these conditions. Lordi and Mates⁵ have shown that for a given nozzle scale and geometry the nonequilibrium effects on composition and thermodynamic state of the gas could be correlated with reservoir entropy. Thus, their results can be used to estimate the nonequilibrium effects for the present wind-tunnel conditions. These estimates are summarized in the following table.

Table II-4
NOZZLE NONEQUILIBRIUM EFFECTS IN HYPOTHETICAL WIND TUNNEL

	CASE I	CASE II	CASE III
FREE-STREAM PARAMETER	$U_\infty = 15,000$ fps	$U_\infty = 25,000$ fps	$U_\infty = 35,000$ fps
(U_∞) NONEQ/(U_∞) EQ	1.00	0.995	0.993
(p_∞) NONEQ/(p_∞) EQ	1.00	0.815	0.700
(T_∞) NONEQ/(T_∞) EQ	1.00	0.790	0.670
(M_∞) NONEQ/(M_∞) EQ	1.00	1.10	1.21
FREE-STREAM COMPOSITION (MOLES/gm OF MIXTURE)			
NITROGEN, N_2	2.6×10^{-2}	2.6×10^{-2}	2.6×10^{-2}
OXYGEN, O_2	5.3×10^{-3}	5.3×10^{-3}	5.0×10^{-3}
NITRIC OXIDE, NO	3.3×10^{-3}	2.9×10^{-3}	2.6×10^{-3}
ATOMIC OXYGEN, O	1.7×10^{-4}	7.7×10^{-4}	1.7×10^{-3}

Even when nonequilibrium effects are energetically unimportant as in the above three cases, the gas composition can be altered from that of undissociated air, particularly through the formation of nitric oxide, as is shown in Table II - 4. The fact that the wind-tunnel flow composition is altered by the amounts shown in Table II - 4 will not significantly affect the flow about a body if the flow achieves thermochemical equilibrium after passing through the bow shock wave. This is illustrated in Sec. V where the equilibrium stagnation-point conditions are presented for the three foregoing cases (Tables V - 1, V - 2 and V - 3). A similar result is shown in Ref. 7. Furthermore, the effect of nozzle-flow nonequilibrium on free-stream pressure, temperature and Mach number is to decrease the differences between wind tunnel and flight conditions shown in Tables II - 1, - 2, and - 3.

Next, we consider the effects of nonequilibrium nozzle flow in the region above of the full-duplication boundary, Fig. 2. For convenience, we will consider just the five velocity-altitude conditions listed in the following table.

Table II-5
VELOCITY-ALTITUDE CONDITIONS IN FULL-DUPPLICATION REGION

CASE	VELOCITY (fps)	ALTITUDE (ft)
IV	15,000	180,000
V	25,000	180,000
VI	15,000	250,000
VII	25,000	250,000
VIII	35,000	250,000

Using the frozen-enthalpy correlation with entropy given in Ref. 5 and in addition other correlations derivable from the results presented there, estimates have been made of the nonequilibrium effects at the above velocity-altitude conditions. The results are given in the following table.

Table II-6
NOZZLE NONEQUILIBRIUM EFFECTS IN HYPOTHETICAL WIND TUNNEL

FREE-STREAM PARAMETER	CASE IV	CASE V	CASE VI	CASE VII	CASE VIII
(U_∞) NONEQ/ (U_∞) EQ	0.977	0.992	0.945	0.980	0.990
(P_∞) NONEQ/ (P_∞) EQ	0.770	0.770	0.550	0.550	0.550
(T_∞) NONEQ/ (T_∞) EQ	0.758	0.758	0.506	0.506	0.506
(M_∞) NONEQ/ (M_∞) EQ	1.11	1.13	1.29	1.34	1.36
FREE-STREAM COMPOSITION (MOLES/gm OF ORIGINAL AIR)					
NITROGEN, N_2	2.57×10^{-2}	2.57×10^{-2}	2.58×10^{-2}	2.58×10^{-2}	2.58×10^{-2}
OXYGEN, O_2	5.45×10^{-3}	5.45×10^{-3}	4.32×10^{-3}	4.32×10^{-3}	4.32×10^{-3}
NITRIC OXIDE, NO	2.54×10^{-3}	2.54×10^{-3}	2.33×10^{-3}	2.33×10^{-3}	2.33×10^{-3}
ATOMIC OXYGEN, O	1.03×10^{-3}	1.03×10^{-3}	3.53×10^{-3}	3.53×10^{-3}	3.53×10^{-3}

The effects of nozzle-flow nonequilibrium on free-stream velocity (and hence on density also⁵) are not large for any of the above cases and could be suitably compensated by adjustment in the total enthalpy. On the other hand, appreciable effects on pressure and temperature occur, particularly at the higher altitude (Cases VI - VIII). However, the resulting mismatches are not as severe as those occurring at 80,000 ft. due to tunnel performance limitations. The most serious nonequilibrium effect for the above conditions is the alteration of the test-gas composition, particularly at the higher altitude where it is unlikely that thermochemical equilibrium will exist behind a bow shock wave. Thus, the existence of free-stream dissociation will influence the flow-field chemistry about a model. Inger⁸ has investigated the influence of a dissociated free-stream on the flow in the stagnation region. However, his method applies only for highly nonequilibrium free-stream conditions and does not permit isolating the effects of free-stream dissociation from mismatches in free-stream Mach number. On the other hand, Gibson⁹ has suggested a "subtraction rule" for accounting for the effects of free-stream dissociation separate from other effects.

Finally, it is of interest to compare test conditions that might be attainable in present-day wind tunnels with flight conditions for the velocity-altitude cases listed in Table II - 5. For this purpose we select a maximum reservoir pressure capability of 2000 atm and assume that reservoir temperatures

up to 17,000 °K are available. This would provide flow velocities up to 36,000 fps for isentropic, equilibrium nozzle flow.

Inspection of Fig. 2 indicates that, in the absence of nonequilibrium effects, such a wind tunnel would provide full duplication at both altitudes for $U_\infty = 15,000$ fps (Cases IV and VI). The nonequilibrium effects on test conditions for these two cases would be the same as listed in Table II - 6 for our hypothetical wind tunnel. For the remaining cases, the flight and wind-tunnel conditions are compared in the following tables. Since full duplication is not possible for these cases, the wind-tunnel is assumed to operate at $p_o = 2000$ atm and to duplicate free-stream velocity and density. Here, the wind-tunnel conditions are based on an isentropic, equilibrium nozzle flow. The nonequilibrium effects will be discussed subsequently.

Table II-7
COMPARISON OF FLIGHT AND 2000-ATM WIND TUNNEL CONDITIONS
Case V: $U_\infty = 25,000$ fps, 180,000 ft Alt.

PARAMETER	FLIGHT	WIND TUNNEL
VELOCITY, U_∞ (fps)	25,000	25,000
DENSITY, ρ_∞ (ama)	4.413×10^{-4}	4.413×10^{-4}
PRESSURE, p_∞ (atm)	4.292×10^{-4}	4.161×10^{-3}
TEMPERATURE, T_∞ (°K)	265.9	2475
MACH NUMBER, M_∞	23.30	8.325
TOTAL ENTHALPY, H_o/R °K	1.020×10^5	1.137×10^5
ENTROPY, S/R	31.25	38.77

Table II-8
COMPARISON OF FLIGHT AND 2000-ATM WIND TUNNEL CONDITIONS
Case VII: $U_\infty = 25,000$ fps, 250,000 ft Alt.

PARAMETER	FLIGHT	WIND TUNNEL
VELOCITY, U_∞ (fps)	25,000	25,000
DENSITY, ρ_∞ (ama)	2.807×10^{-5}	2.507×10^{-5}
PRESSURE, p_∞ (atm)	2.097×10^{-5}	1.238×10^{-5}
TEMPERATURE, T_∞ (°K)	195.5	1205
MACH NUMBER, M_∞	27.18	10.95
TOTAL ENTHALPY, H_0/R (°K)	1.013×10^5	1.055×10^5
ENTROPY, S/R	33.24	35.05

Table II-9
COMPARISON OF FLIGHT AND 2000-ATM WIND TUNNEL CONDITIONS
Case VIII: $U_\infty = 35,000$ fps, 250,000 ft Alt.

PARAMETER	FLIGHT	WIND TUNNEL
VELOCITY, U_∞ (fps)	35,000	35,000
DENSITY, ρ_∞ (ama)	2.807×10^{-5}	2.897×10^{-5}
PRESSURE, p_∞ (atm)	2.097×10^{-5}	3.842×10^{-5}
TEMPERATURE, T_∞ (°K)	195.5	3100
MACH NUMBER, M_∞	33.05	9.11
TOTAL ENTHALPY, H_0/R (°K)	1.938×10^5	2.235×10^5
ENTROPY, S/R	33.24	45.20

Clearly the mismatches in p_∞ , T_∞ and M_∞ are large for these three cases. The question is whether they are too large to permit simulation of a Mach number independent flow. The simplest test of this is to compare equilibrium and frozen flow conditions behind a normal shock wave. The equilibrium conditions for the flight case are given in Ref. 10. For the 2000-atm wind tunnel they have been calculated. The equilibrium flow results are compared in the following table.

Table II-10
COMPARISON OF EQUILIBRIUM CONDITIONS BEHIND
A NORMAL SHOCK WAVE
IN FLIGHT AND 2000-ATM WIND TUNNEL

PARAMETER	FLIGHT	WIND TUNNEL
CASE I: $U_{\infty} = 25,000$ fps 180,000 FT ALTITUDE		
PRESSURE, p_s (atm)	0.3072	0.3048
DENSITY, ρ_s (ama)	7.273×10^{-3}	6.751×10^{-3}
TEMPERATURE, T_s (°K)	5801	6952
CASE VII: $U_{\infty} = 25,000$ fps 250,000 FT ALTITUDE		
PRESSURE, p_s (atm)	0.01967	.01984
DENSITY, ρ_s (ama)	5.196×10^{-4}	5.101×10^{-4}
TEMPERATURE, T_s (°K)	5959	6622
CASE VIII: $U_{\infty} = 35,000$ fps 250,000 FT ALTITUDE		
PRESSURE, p_s (atm)	0.03837	0.03856
DENSITY, ρ_s (ama)	4.815×10^{-4}	4.491×10^{-4}
TEMPERATURE, T_s (°K)	10,120	10,320

For frozen flow the ideal-gas shock equations are used with the proper values of the specific-heat ratio for the wind tunnel conditions. These are $\gamma = 1.416$, 1.401 and 1.465 for Cases V, VII and VIII, respectively. The frozen flow results are tabulated below.

Table II-11
COMPARISON OF FROZEN-FLOW CONDITIONS BEHIND
A NORMAL SHOCK WAVE
IN FLIGHT AND 2000-ATM WIND TUNNEL

PARAMETER	FLIGHT	WIND TUNNEL
CASE I: $U_{\infty} = 25,000$ fps 180,000 FT ALTITUDE		
PRESSURE, p_s (atm)	0.2719	0.2656
DENSITY, ρ_s (g/cc)	2.624×10^{-3}	2.354×10^{-3}
TEMPERATURE, T_s (°K)	28,310	29,610
CASE VII: $U_{\infty} = 25,000$ fps 250,000 FT ALTITUDE		
PRESSURE, p_s (atm)	0.01730	0.01935
DENSITY, ρ_s (g/cc)	1.673×10^{-4}	1.612×10^{-4}
TEMPERATURE, T_s (°K)	28,260	29,420
CASE VIII: $U_{\infty} = 35,000$ fps 250,000 FT ALTITUDE		
PRESSURE, p_s (atm)	0.03390	0.03300
DENSITY, ρ_s (g/cc)	1.678×10^{-4}	1.405×10^{-4}
TEMPERATURE, T_s (°K)	55,220	53,200

It is observed that for both equilibrium and frozen flow the conditions behind a normal shock wave in the 2000-atm wind tunnel correspond closely to the flight conditions for these three cases when nonequilibrium nozzle flow effects are neglected. Thus Mach number independent flow fields would be quite well duplicated in the wind tunnel if nozzle nonequilibrium effects were not present.

When the flow field is not Mach number independent, one must expect differences as a result of mismatches in the free-stream conditions. For Case VII (Table II-8) the relative free-stream differences between the 2000-atm wind tunnel and flight are nearly the same as those for the high performance hypothetical wind tunnel in Case II (Table II-2). Thus, the results reported for this latter case in Sec. V would be indicative of the relative differences

between such flows in the 2000-atm wind tunnel for Case VII. In Cases V and VIII the free-stream pressures and temperatures in the 2000-atm tunnel are about 10 and 15 times greater than the corresponding flight values; however nozzle nonequilibrium effects will reduce these differences appreciably.

Estimates of the nonequilibrium effects on the free-stream conditions in the 2000-atm wind tunnel have been made using the entropy correlations described previously. The results are summarized in the following table.

Table II-12
NOZZLE NONEQUILIBRIUM EFFECTS IN 2000-ATM WIND TUNNEL

FREE-STREAM PARAMETER	CASE V	CASE VII	CASE VIII
$(U_{\infty})_{\text{NONEQ}} / (U_{\infty})_{\text{EQ}}$	0.99	0.94	0.93
$(\rho_{\infty})_{\text{NONEQ}} / (\rho_{\infty})_{\text{EQ}}$	1.01	1.06	1.07
$(p_{\infty})_{\text{NONEQ}} / (p_{\infty})_{\text{EQ}}$	0.55	0.18	0.10
$(T_{\infty})_{\text{NONEQ}} / (T_{\infty})_{\text{EQ}}$	0.50	0.14	0.075
$(M_{\infty})_{\text{NONEQ}} / (M_{\infty})_{\text{EQ}}$	1.3	2.2	2.6
FREE-STREAM COMPOSITION (MOLES/gm OF ORIGINAL AIR)			
NITROGEN, N_2	2.6×10^{-2}	2.6×10^{-2}	1.6×10^{-2}
OXYGEN, O_2	1.9×10^{-5}	1×10^{-4}	
NITRIC OXIDE, NO	1×10^{-4}	6.3×10^{-4}	3.5×10^{-6}
ATOMIC NITROGEN, N	3.7×10^{-4}	1×10^{-4}	1.9×10^{-2}
ATOMIC OXYGEN, O	1.5×10^{-2}	1.4×10^{-2}	1.5×10^{-2}

When nozzle nonequilibrium effects are accounted for, the large differences in free-stream pressure, temperature and Mach number between flight and wind tunnel are drastically reduced. For example, in Case VIII, the wind-tunnel Mach number is increased from 9.11 to 23.7 compared to a flight value of 38.05. On the other hand, the nozzle nonequilibrium alters the test gas composition in an undesirable manner. In Cases V and VII the test gas is primarily a mixture of molecular nitrogen and atomic oxygen; whereas in Case VIII it is composed of nearly equal parts of molecular nitrogen,

atomic nitrogen and atomic oxygen. Fortunately, large differences in gas composition do not necessarily result in proportionately large effects on pressure, density and temperature. To illustrate this fact, the limiting cases of equilibrium and frozen flow behind a normal shock wave have been computed for the nonequilibrium free-stream conditions of the 2000-atm wind tunnel (Table II-12). The results are shown in Table II-13.

Table II-13
EQUILIBRIUM AND FROZEN FLOW CONDITIONS BEHIND A
NORMAL SHOCK WAVE IN A NONEQUILIBRIUM 2000-ATM WIND TUNNEL

PARAMETER	EQUILIBRIUM	FROZEN FLOW
CASE V: $U_{\infty} = 25,000$ fps 180,000 FT ALTITUDE		
PRESSURE, P_s (atm)	0.3033	0.2446
DENSITY, ρ_s (ama)	6.412×10^{-3}	2.234×10^{-3}
TEMPERATURE, T_s ($^{\circ}$ K)	7135	26,400
CASE VII: $U_{\infty} = 25,000$ fps 250,000 FT ALTITUDE		
PRESSURE, P_s (atm)	0.01828	0.01606
DENSITY, ρ_s (ama)	4.817×10^{-4}	1.565×10^{-4}
TEMPERATURE, T_s ($^{\circ}$ K)	5952	23,120
CASE VIII: $U_{\infty} = 35,000$ fps 250,000 FT ALTITUDE		
PRESSURE, P_s (atm)	0.03495	0.03048
DENSITY, ρ_s (ama)	4.095×10^{-4}	1.384×10^{-4}
TEMPERATURE, T_s ($^{\circ}$ K)	10,200	40,020

Comparison of the equilibrium-flow limit with Table II-10 shows relatively little effect of the dissociated free-stream on conditions behind the shock wave. The differences from the flight case are, however, somewhat larger than when nozzle nonequilibrium effects were not taken into account.

Comparing Tables II-11 and II-13 indicates that in the frozen-flow limit, the effects of nozzle flow nonequilibrium are more pronounced than in the above equilibrium limit - particularly on the temperature T_s . Although a direct comparison with Ref. 8 is difficult, these results are generally in qualitative though not quantitative agreement with Inger's findings.

SECTION III

GENERAL FEATURES OF BLUNT-NOSED SLENDER BODY FLOWS

The slender cone having a blunted nose is of particular interest because it typifies more general blunt-nosed slender bodies. In this section the various features of the flow field about a slightly blunted cone are discussed for the flight region shown in Fig. 1. The important items to be considered are rarefaction effects, viscous effects and flow chemistry. Since these phenomena depend on geometry and scale, the discussion will pertain to the specific body treated in Sec. V. This body has a cone half-angle of 9° and a nose radius of either 0.2 or 1.5 inches. Where a length is needed, a value of 88 inches has been assumed. In discussing the various phenomena listed above, it is convenient to consider the flow in the blunt-nose region separately from the after body flow along the cone. This distinction is reasonable since the flows in these two regions may be quite dissimilar.

Because the flight region of interest (Fig. 1) extends to an altitude of 250 Kft, the first concern is about the possible presence of rarefaction effects. As long as the bow shock wave is thin relative to the shock stand-off distance at the nose and the shock-layer thickness along the cone, the flow may be treated as a continuum fluid and rarefaction effects may be considered unimportant. Hayes and Probstein¹¹ have considered the various rarefaction and viscous interaction flow regimes and have established simple criteria which will be adopted here.

In the region of the blunt-nose, the mean-free-path behind the shock serves as a measure of the shock thickness and the following quantities are all of the same order of magnitude

$$\frac{\lambda_s}{\Delta} \sim \frac{\lambda_\infty}{R_n} \sim \frac{M_\infty}{Re_{R_n, \infty}}$$

where λ_s is the mean-free-path behind the bow shock wave, Δ is the shock stand-off distance, λ_∞ is the mean-free-path in the free-stream, R_n is the nose radius and $Re_{R_n, \infty}$ is Reynolds number based on free-stream conditions and nose radius. A suitable criterion for continuum flow in the nose region is

that these ratios be small compared to unity. Fig. 3 shows results for the two nose radii of interest and indicates the various flow regimes defined by Hayes and Probstein¹¹. For each R_n , the upper bound of the shaded region is defined by λ/R_n and the lower bound by M_∞/Re_{R_n} . This indicates the degree to which these ratios differ. The boundaries of the flow regimes shown in Fig. 3 are based on the criteria of Ref. 11 with the interpretation that $1/10$ is much less than one. Clearly, these boundaries are not distinct as shown in Fig. 3, but should have some width analogous to the shaded areas shown for the two nose radii.

From Fig. 3 it is seen that continuum flow exists at all altitudes of interest for the larger nose radius and below about 225 Kft for the smaller nose radius. It should be pointed out that in the incipient merged layer regime the shock wave is not a thin discontinuity governed by the Rankine-Hugoniot relations even though the flow may be treated as a continuum. Above 225 Kft for the smaller nose radius, the continuum flow concept begins to breakdown.

Having established that rarefaction effects are generally unimportant for the bodies and flight conditions of interest, we next consider the importance of viscous effects. For the flow about the blunt-nose, the regions of important viscous effects are defined in Fig. 3. Considering just the smaller nose radius, it is seen that the boundary layer is thin below 100 Kft. From 100 Kft to about 160 Kft vorticity in the inviscid flow influences the boundary layer. From 160 Kft to about 190 Kft, the shock layer becomes fully viscous although the bow shock may still be considered as a discontinuity. Above 190 Kft, the rarefaction effects on shock structure begin to enter as just described.

Similar viscous interaction effects occur on slender bodies as a result of the relative thicknesses of the boundary layer and the shock layer. These viscous phenomena take the form of weak and strong pressure interactions between the boundary layer and the outer inviscid flow vorticity interaction, transverse curvature effects and ultimately a fully viscous shock layer. For slender bodies having a blunt nose, the inviscid flow consists of an inner region of high entropy emanating from the nearly normal portion of the detached bow shock and an outer region of low entropy flow

which has passed through the oblique portions of the bow shock. Thus, when the boundary layer is thin, it grows within the high entropy layer. Eventually all of the entropy layer is "swallowed" by the boundary layer. Then the outer edge conditions of the boundary layer are governed by the flow passing through a much weaker bow shock. Clearly, the downstream influence of the blunt-nose complicates the problem of delineating these various viscous regimes.

Theoretical studies of these various effects in the flow of an ideal gas about sharp and blunted cones and "power-law" bodies have been reported in Refs. 11 - 19. The more recent of these studies, which are also the most complete in their inclusion of the effects described above, require numerical solutions in order to achieve quantitative results. In view of the limited results reported and the lack of consideration of real-gas effects, only qualitative estimates can be made of the flight conditions for which viscous interactions are important. Based on consideration of the results presented in Refs. 11, 18, and 19, it would appear that for the smaller value of R_N (0.20 in) viscous interaction effects are negligible below an altitude of 100 Kft, become important between 150 Kft and 200 Kft and are dominant at 250 Kft.

Finally, we must consider the nature of the air chemistry for the flight conditions of interest. When the free-stream static temperature is low ($\approx 300^\circ\text{K}$), the equilibrium-air solutions for cones²⁰ indicate that at values of $M_\infty \sin \sigma > 5$ (where σ is the shock wave angle), the temperature and density in the flow behind the bow shock wave differ by 10% or more from the ideal-gas values. For a 9° half-angle cone having blunted nose, real-gas effects would be present throughout the flow field for $M_\infty > 29$. At $M_\infty = 25$, they would be present wherever $\sigma \geq 11.5^\circ$ or over most of the flow field since the asymptotic shock angle is just 10.1° . At $M_\infty = 15$, real-gas effects would be present for $\sigma > 19.5^\circ$. Since the detached bow shock decays to this value within three nose radii and the asymptotic shock angle is 10.4° , the extent of real-gas effects would be much reduced over the two higher Mach number cases but would extend beyond what is typically termed the entropy layer. Thus for the flight cases of interest real-gas effects will not necessarily be restricted

to the region of the blunt nose and the entropy layer emanating from this region. On the other hand, whenever the wind tunnel must resort to partial simulation, the high free-stream temperatures may introduce even more extensive regions of real-gas effects. The situation in this case is much more complex, however, since the high free-stream temperatures are accompanied by lower free-stream Mach numbers than in the flight case. The criterion $M_\infty \sin \sigma > 5$ for real-gas effects is not appropriate when $T_\infty \gg 300^\circ\text{K}$. Some indication of the presence of real-gas effects in the wind tunnel case when none existed in the flight case may be found in conical shock calculations presented in Sec. V.C.

The flow behind the detached bow shock at the nose must be treated as a real-gas over the entire range of flight conditions being considered. The question then becomes one of determining whether the flow may be treated as equilibrium air or whether finite-rate chemical processes (i.e. nonequilibrium phenomena) are important. Criteria for delineating regions of frozen, nonequilibrium and equilibrium chemistry are rather arbitrary.

Harney²¹ and Wittliff et al.¹ have defined different criteria which are compared in Ref. 1 for the flow about a blunt-nose of 1 foot radius. At the boundary between frozen and nonequilibrium chemistry^{1,21} only bimolecular reactions are important. Thus, binary scaling²² can be used to apply Harney's results for a 1-ft nose radius to the radii of present interest.

On the other hand, binary scaling does not govern the approach to equilibrium chemistry. However, the nonequilibrium normal shock wave solutions reported in Ref. 1 have been used to define a distance required to reach equilibrium. If this distance is small compared to the shock standoff distance at a blunt nose, equilibrium flow may be assumed. On this basis, equilibrium flow boundaries have been estimated for the nose radii being considered in the present study.

Fig. 4 shows the boundaries between frozen, nonequilibrium and equilibrium flow for $R_N = 0.2''$ and $1.5''$ as determined by the above methods. For the flight conditions and nose radii of interest, the assumption of frozen flow is restricted to a small low-velocity, high altitude region. At low

altitudes, the assumption of equilibrium flow is valid for a fairly extensive range of velocities. The equilibrium criteria specified in Ref. 1 (namely, that the temperature be within 1% of the equilibrium value) is quite restrictive, however; and equilibrium flow probably can be assumed to exist over a somewhat broader range of conditions than indicated in Fig. 4.

SECTION IV REVIEW OF HYPERSONIC SIMILITUDES

A. INVISCID FLOW

The inviscid flow similitudes that are appropriate to slender bodies are based on hypersonic small-disturbance theory. Tsien²³ showed that for the hypersonic, inviscid, irrotational flow of an ideal gas with constant specific heats past affinely related slender bodies, the requirement of duplication of Mach number, per se, can be relaxed provided that the parameter $M_\infty \tau$ (where τ is a characteristic thickness ratio) is kept constant. Hayes²⁴ showed the equivalence of a steady hypersonic flow over a slender body with an unsteady flow in one less space dimension and thus extended Tsien's result to rotational flow.

Cheng²⁵ extended this classical slender-body hypersonic similitude to include the effects of small nose bluntness and equilibrium real-gas phenomena. Similitude of equilibrium real-gas effects requires duplication of the ambient flow thermodynamic and chemical state (i.e. pressure p_∞ , density ρ_∞ , temperature T_∞ , and species concentrations $X_{i\infty}$) in addition to the hypersonic similarity parameter $M_\infty \tau$. Through application of the blast-wave analogy, Cheng found that for axisymmetric bodies similitude of nose bluntness effects requires duplication of a bluntness parameter

$$K_N \equiv M_\infty^2 C_{D_N}^{1/2} \frac{d_N}{L} \quad (\text{IV-1})$$

where C_{D_N} is the nose drag coefficient, d_N is the diameter of the blunt nose and L is the body length. Cheng states his similitude in the form

$$\frac{p}{p_\infty} = f\left(\frac{x}{L}, \frac{y}{L}; M_\infty \tau, K_N; p_\infty, \rho_\infty, X_{i\infty}\right) \quad (\text{IV-2})$$

with similar expressions for all other flow variables.

It is possible to rewrite the above similitude in the form

$$\frac{p}{\rho_{\infty} U_{\infty}^2 \tau^2} = f\left(\frac{x}{L}, \frac{y}{\tau L}; U_{\infty} \tau, U_{\infty}^2 C_{D_N}^{1/2} \frac{d_N}{L}; T_{\infty}, \rho_{\infty}, X_{\infty}\right) \quad (\text{IV-3})$$

Eqs. (IV-2) and (IV-3) are entirely equivalent when the free-stream thermodynamic state is completely duplicated. However, as mentioned previously, mismatches in free-stream temperature are unavoidable at many altitudes because of wind-tunnel performance limitations. In such cases, the form of the similitude given in Eq. (IV-3) is to be preferred over that given in Eq. (IV-2) since the former (by virtue of the Mach number independence principle) represents the correct similitude when $M_{\infty} \tau \gg 1$, even when the free-stream temperature is not duplicated.

Cheng²⁵ briefly considered the question of extension of the hypersonic similitude to nonequilibrium flows. He suggested that for slender bodies, a nonequilibrium similitude should exist for a two-component reacting gas when $M_{\infty} \tau \gg 1$. The nonequilibrium similitude required that the particle transit time L/U_{∞} be duplicated in addition to $M_{\infty} \tau$, K_N , ρ_{∞} , ρ_{∞} and $X_{i\infty}$. The formal development of the nonequilibrium hypersonic similitude for a single-species diatomic gas has been carried out by Inger²⁶, who reached the same conclusion as Cheng. As in the equilibrium case this similitude contains the very stringent requirement of duplication of the free-stream thermodynamic state; a requirement that can not be satisfied for low-altitude hypervelocity flight even in the hypothetical wind tunnel described in Sec. II. In Sec. VI-D an extremely useful though restrictive similitude is derived in which the requirement of the duplication of the free-stream thermodynamic state can be relaxed.

It should be pointed out that Cheng's nose bluntness parameter does not insure similitude of the flow in the immediate region of the blunt nose, but only provides similitude of the nose-bluntness effects in the flow far downstream of the nose.

The Mach number independence principle for the flow of an ideal gas past a blunt body was first stated by Oswatitsch²⁷. For a perfect gas having a constant specific-heat ratio, the Mach number independence principle specifies that the flow field behind the bow shock wave of a blunt body reaches a limiting configuration as the free-stream Mach number becomes very large. Hayes and Probstein¹¹ have generalized this principle. They show that two geometrically similar flows of a given gas with the same ρ_∞ and U_∞ and large, but different, M_∞ are not merely similar, but are essentially identical behind the bow shock wave. Hence, the independence principle applies to all real fluid effects. It should be emphasized, however, that whenever dissipative processes (i. e., chemical relaxation or viscous phenomena) are present, the bodies must be not merely geometrically similar but identical since particle transit time (L/U_∞) or length scale (L) must be matched in addition to ρ_∞ and U_∞ .

The combined requirements of the Mach number independence principle and hypersonic slender-body similitude dictate that, when the combined effects of nonequilibrium phenomena and nose bluntness are present, complete duplication of free-stream thermo-chemical state, free-stream velocity and body size and shape is necessary. However, for those cases where these requirements cannot be fully satisfied because of wind-tunnel performance limitations, it is preferable to duplicate ρ_∞ , U_∞ and body size.

Clearly, the practical usefulness of similarity laws depends upon their range of applicability. A similitude cannot, by itself, define the limits for which it yields reasonable results. This must be accomplished by correlations of theoretical solutions or experimental data in terms of the similarity parameters. Often, the similitude parameters are applicable over a wider range of Mach numbers and slenderness ratios than might be expected from the assumptions made in their derivations. This is shown, for example, in the correlations presented in Refs. 28 and 29 for the case of an ideal gas. When real gas effects are present, it has been shown^{1,2} that, for slender bodies, the onset of Mach number independence does not occur until the Mach number is significantly higher than in the corresponding ideal-gas case.

B. VISCOUS FLOW

The similitudes that apply to hypersonic flows for cases where transport effects due to viscosity, diffusion, thermal conduction and the like play a role have been reviewed in Ref. 1. In addition Hayes and Probst³⁰ have presented a fundamental description of viscous hypersonic similitude for slender bodies including the implications of the Mach number independence principle for hypersonic boundary layers. A further discussion of the combined effects of nose bluntness, boundary-layer displacement and flow nonequilibrium on slender-body flow fields is given in Sec. VI-F of this report.

For the case of sharp-nosed slender bodies, Hayes and Probst³⁰ note that "it is impossible to find a viscous similitude for a fluid obeying a general equation of state." They go on to point out that when the inviscid flow behaves as a perfect gas and only the boundary-layer flow exhibits real-gas effects, a similitude is possible. The similitude requirements for affinely related bodies are that the following quantities be duplicated:

$$M_\infty \tau, U_\infty, p_\infty, \tau^2 L, h_w/H_\infty$$

and that the gas be the same. Whenever $H_\infty \approx \frac{1}{2} U_\infty^2$, the enthalpy ratio h_w/H_∞ may be replaced by T_w .

In Sec. VI-F the viscous similitudes for blunt-nosed slender bodies are discussed for the case where the boundary layer is thinner than the entropy layer. For cases of interest here, the Mach number independence principle provides similitude of the flow in the region of the blunt nose, even when viscous effects are present, if p_∞ , U_∞ and the nose radius are duplicated. However, the requirement that both p_∞ and ρ_∞ be duplicated implies that T_∞ is duplicated also. Thus, for slender bodies having blunt noses no similitude exists and full duplication is required. An approximate similitude can be found though for plane flows and is presented in Sec. VI-F.

SECTION V

COMPARISON OF FLOWS OVER BLUNTED SLENDER CONES FOR PARTIALLY SIMULATED CONDITIONS

A. INTRODUCTION

We now turn our attention to the flight region below the full duplication boundary of the hypothetical wind tunnel, Fig. 2. The objective of the study is to compare flow fields in flight and in a wind tunnel when complete duplication is unattainable. Consideration is restricted to a blunted slender cone as a typical body shape of interest. The only general solutions for blunted cones are for an ideal gas and involve certain approximations^{31, 32*}. Exact numerical solutions have been reported for both an ideal gas^{33, 34} and equilibrium real air³⁵. In addition, a few numerical solutions for nonequilibrium real air have been calculated (e.g. Ref. 36). These existing solutions were insufficient for the purposes of the present study because none of them correspond to the cases of partial simulation in a wind tunnel being considered here. Thus, in order to obtain a quantitative comparison of flight and wind tunnel flow fields over a slender cone, it was necessary to undertake specific solutions. As indicated in Sec. II this was done for three flight conditions.

In the present study a cone half-angle of 9° was chosen since it is a shape that has been studied extensively (e.g. Ref. 37). In order to investigate nose bluntness effects, nose radii of 0.2 and 1.5 inches were selected. Calculations were made for air with frozen, finite-rate and equilibrium chemistry to assess the importance of real-gas effects. Only the body streamline and a streamline passing through the outer oblique portion of the bow shock wave were considered. These represent the two extremes of the total inviscid flow field.

The free-stream conditions for the flight and wind tunnel cases have been compared in Sec. II. In keeping with the similitude discussion of Sec. IV, U_∞ and θ_c are duplicated in the present calculations rather than $M_\infty \theta_c$. In this section, the method of calculation is described and the detailed results are presented and discussed.

* See Sec. VI B for a further discussion of these analyses.

B. METHOD OF FLOW FIELD ANALYSIS

1. General Approach. The flow field about a blunted slender cone is characterized by a detached bow shock wave at the nose which decays to a conical shock wave far downstream. The flow entering the bow shock near the axis experiences much higher entropy and temperature levels than the flow passing through the more oblique outer portion of the shock. Along the body, the flow is initially dominated by the presence of the blunt nose. However, with increasing distance from the nose, the pressure gradually approaches the equivalent sharp cone value. Rather than attempt an analysis of the complete flow field, comparisons of the flight and wind-tunnel cases have been made for just two streamlines: (1) the streamline passing through the stagnation point; (2) a streamline passing through the conical portion of the shock wave.

Because the body streamline will not differ greatly from adjacent streamlines entering the nearly normal portion of the bow shock, the comparison between flight and wind tunnel for the body streamline will also typify other streamlines in the entropy layer. In addition, Wood et al.³⁶ have shown that a body streamtube calculation based on the pressure distribution for equilibrium flow is in good agreement with an exact method of characteristics solution. The calculation for the conical-shock streamline typifies conditions downstream of the nose where the flow conditions outside the entropy layer approach the sharp cone values.

The body streamtube flow has been calculated using the CAL computer program for the quasi-one-dimensional, inviscid flow of reacting gas mixtures³⁸. One of the capabilities of this program is to compute the flow of a general mixture of reacting gases through a streamtube having a specified pressure distribution. Thus, a first step in the present study was the determination of the pressure distribution on a blunted 9° half-angle cone at the flight and wind-tunnel conditions of interest. In addition, it was necessary to specify initial conditions at the stagnation point. For the latter, thermodynamic equilibrium has been assumed. This assumption is well-justified for the two velocities at 80,000 ft altitude (Fig. 4); however, it is somewhat questionable for the case at 180,000 ft particularly for the smaller nose radius. Since the primary objective of the study is a comparison of flight

and wind-tunnel flow fields, the relative differences between these flows are more important than the absolute values. On this basis, the error introduced in assuming equilibrium flow at 180,000 ft altitude is believed to be acceptable. The actual equilibrium stagnation-point conditions were obtained from an equilibrium normal shock calculation followed by an equilibrium, isentropic compression to the total enthalpy value (i. e. zero velocity).

2. Blunted Cone Pressure Distributions. The pressure distribution was determined from a study of existing flow field solutions. On the spherical nose, the pressure was found to be insensitive to flow chemistry. This is illustrated in Fig. 5 which shows pressure distributions on a spherical nose for an ideal gas ($\gamma' = 1.4$),³³ real air in equilibrium,^{35, 39} and nonequilibrium real air. The nonequilibrium pressure distribution was obtained using the computer program reported in Ref. 40. The results shown in Fig. 5 encompass velocities, altitudes and nose radii appropriate to the present investigation. Although the ideal-gas pressures are slightly higher than the equilibrium air values, no appreciable effect of chemistry on pressure is evident. The faired curve shown in Fig. 5 has been used in the present study.

Along the conical afterbody ideal-gas and equilibrium air pressure distributions do not exhibit the same agreement. This is illustrated in Fig. 6 where theoretical solutions for an ideal gas ($\gamma' = 1.4$)³³ and equilibrium air³⁵ are correlated as $C_p/2\theta_c^2$ versus $(\theta_c^2/\sqrt{\epsilon C_{Dn}})(x/2R_n)$. Distinct differences between the two ideal-gas solutions and the several equilibrium air solutions are readily apparent in this figure. Some comment on this correlation is appropriate here. The exact similitude is of the form

$$\frac{p_w}{\theta_c^2 \rho_\infty U_\infty^2} = \frac{p_w}{\rho_\infty M_\infty^2 \theta_c^2} = f\left(\frac{\theta_c^2}{\sqrt{\epsilon C_{Dn}}} \frac{x}{2R_n}, M_\infty \theta_c, \gamma'_\infty\right) \quad (V-1)$$

If equilibrium real-gas effects are to be included, then γ'_∞ has to be replaced by ρ_∞ , T_∞ and X_{i_∞} . Cheng has shown that in the limits $M_\infty \theta_c \gg 1$ and $\gamma'_\infty \rightarrow 1$, the above similitude becomes:

$$\frac{p_w}{\gamma'_\infty \rho_\infty M_\infty^2 \theta_c^2} = f\left(\frac{\theta_c^2}{\sqrt{\epsilon C_{Dn}}} \frac{x}{2R_n}\right) \quad (V-2)$$

where $\epsilon = \frac{\gamma_\infty - 1}{\gamma_\infty + 1}$. This is the result given by zeroth-order thin shock layer theory. Griffith and Lewis⁴¹ showed that using $C_p/2\theta_c^2$ rather than $p_w/\gamma_\infty p_\infty M_\infty^2 \theta_c^2$ yielded better correlation of experimental data obtained under essentially ideal-gas conditions. When $p_w \gg p_\infty$, we note that $C_p/2\theta_c^2$ reduces to Cheng's parameter. In the limit $M_\infty \theta_c \gg 1$ both parameters properly express the dependence of pressure on $M_\infty \theta_c$. For values of $M_\infty \theta_c$ below the Mach number independent regime, $C_p/2\theta_c^2$ appears to provide better correlation of theoretical solutions and experimental data even though the theoretically proper similitude parameter is $p_w/\gamma_\infty p_\infty M_\infty^2 \theta_c^2$. The effect of a finite value of $M_\infty \theta_c$ can be seen in Fig. 6 by comparing the two ideal-gas solutions for $M_\infty = 10$ and ∞ at $\theta_c = 10^\circ$. The major difference is in the region of the minimum pressure where both the magnitude and the location are different. In contrast, the equilibrium air solutions show the greatest disagreement close to the spherical nose and relatively good agreement near the pressure minimum. When these same solutions were correlated in terms of $p_w/\gamma_\infty p_\infty M_\infty^2 \theta_c^2$ rather than $C_p/2\theta_c^2$, greater scatter was found without any discernable trend due to $M_\infty \theta_c$. The solid curve in Fig. 6 drawn through the equilibrium air correlation was adopted for the present calculations.

After the recompression region downstream of the minimum pressure point, the pressures approach the equivalent sharp cone pressures. The sharp cone pressures have been obtained from a correlation of ideal-gas solutions^{42, 43} and equilibrium air solutions.²⁰ An approximate fairing from the distribution given in Fig. 6 to the sharp-cone pressure for each free-stream Mach number has been used. The final result is shown in Fig. 7 as p/p_0' versus x/R_N . The curves are labeled by Case number (See Sec. II) and whether they correspond to flight (Flt.) or wind tunnel (W. T.) conditions as well as by free-stream Mach number. The pressure distribution for Case III W. T. $M_\infty = 27.34$ has been omitted to avoid cluttering the figure since it lies between the two lower curves. It should be emphasized that these curves do not exactly account for the effect of different values of M_∞ but have inherent in them the scatter observed in Fig. 6.

The final step in specifying the pressure distribution for the computer

program was to fit polynomial functions to the faired curves shown in Figs. 5 and 7 for each value of M_∞ . Each pressure distribution was divided into 8 intervals so that only third-order polynomials were needed.

3. Streamtube Computer Program. The computer program utilized for the body streamtube calculations provides numerical solutions for the quasi-one-dimensional, inviscid flow of chemically reacting gas mixtures as well as the limiting cases of frozen and equilibrium flow³⁸. Vibrational excitation can be either frozen at the initial level or in equilibrium with the translational temperature. The latter option was utilized in the present work. Electronic excitation is assumed to be in equilibrium with the translational temperature also. For the flight cases, calculations were made for frozen, finite-rate, and equilibrium chemistry. Whereas for the wind-tunnel cases, only finite-rate or nonequilibrium chemistry calculations were performed.

The calculations for Case I ($U_\infty = 15,000$ fps) were made with an air model consisting of 8 species (N_2 , O_2 , A_1 , N , O , NO , NO^+ and e^-) and 11 chemical reactions³⁸. This simple air model is justified because the stagnation-point temperature was less than 6000 °K, hence NO^+ was the only significant ionized species. For Case II ($U_\infty = 25,000$ fps), the stagnation-point temperatures approach 9000 °K, and it is necessary to include other ionized species. Consequently, a 12-species, 39-reaction air model was utilized. The additional ionized species were N_2^+ , O_2^+ , N^+ and O^+ . The 12-39 air model was also used for Case III ($U_\infty = 35,000$ fps) where the stagnation-point temperature is somewhat higher than 11,000 °K.

4. Conical-Shock Calculations. Conical-flow solutions have been correlated in terms of the hypersonic similarity parameter $M_\infty \sin \theta_c$ for an ideal gas⁴⁴ and for equilibrium real air.²⁰ In the latter case, correlation obtains only at a fixed free-stream state²⁵ (i.e., at a fixed altitude); this is equivalent to saying that the solutions for equilibrium air can be correlated in terms of $U_\infty \sin \theta_c$ at each altitude (see Sec. II). In the present study, U_∞ and θ_c are duplicated, while $M_\infty \sin \theta_c$ is not.

A conical-flow streamline experiences a discontinuous compression at the shock wave followed by an additional isentropic compression downstream

of the shock. For slender cones at high Mach number, the isentropic compression is small compared to the shock compression. For the range of conditions under consideration here, the pressure on the cone surface is from 6 percent to 13 percent higher than the pressure just behind the conical shock, the density is from 4 percent to 9 percent greater, and the temperature from 1.5 percent to 3.5 percent greater. Thus, for present purposes of comparison of flight and wind-tunnel situations, it is adequate to calculate only the conditions immediately behind the shock. In these calculations, account must be taken of the high free-stream static temperatures occurring in the wind-tunnel cases because they introduce real-gas effects at lower values of

$M_\infty \sin \theta_c$ than predicted by the solutions reported in Ref. 20. Utilizing the fact that the shock angle and pressure are relatively insensitive to real-gas effects, it is possible to use Refs. 20, 42, 43 to obtain solutions for equilibrium air for the wind-tunnel cases. The highest temperature computed for these cases was less than 2300 °K. At such temperatures, any nonequilibrium phenomena will not introduce variations in the flow quantities that are any larger than the already neglected effects of the isentropic compression. Hence, it is sufficient to consider just the equilibrium-air case.

For these conical-shock calculations, any nozzle flow nonequilibrium effects will influence the flow downstream of the conical shock wave. To assess this influence, conical-shock calculations were also made for frozen flow utilizing the estimated nozzle nonequilibrium conditions presented earlier. The results are then compared with the equilibrium air calculations.

C. RESULTS OF CALCULATIONS

1. Equilibrium Stagnation-Point Conditions. Before presenting the results of the streamtube calculations, the initial stagnation-point conditions will be compared. For the flight cases, these results were obtained from Ref. 10 whereas the wind-tunnel results were calculated from an equilibrium normal-shock solution followed by an isentropic compression to the total enthalpy state (i. e., zero velocity). Since the nozzle-flow nonequilibrium effects are not large for these three cases (Table II-4), the wind-tunnel equilibrium free-stream conditions have been used (Tables II-1, -2, -3). The following tables present the pressure, temperature, density and species concentrations (moles/gm of mixture) at the stagnation point for thermochemical equilibrium.

Table V-1
COMPARISON OF STAGNATION - POINT CONDITIONS
Case I, $U_\infty = 15,000$ fps

THERMODYNAMIC QUANTITY	FLIGHT	WIND TUNNEL
PRESSURE, p'_0 (atm)	8.701	8.727
TEMPERATURE, T'_0 (°K)	5472	5650
DENSITY, ρ'_0 (ama)	0.3632	0.3500
SPECIES (MOLES/gm OF MIXTURE)		
N_2	2.573×10^{-2}	2.56×10^{-2}
O_2	2.291×10^{-4}	1.663×10^{-4}
N	1.002×10^{-3}	1.409×10^{-3}
O	1.256×10^{-2}	1.283×10^{-2}
NO	1.467×10^{-3}	1.323×10^{-3}
NO^+ , e	2.423×10^{-6}	3.269×10^{-6}

Table V-2
COMPARISON OF STAGNATION-POINT CONDITIONS
Case II, $U_\infty = 25,000$ fps

THERMODYNAMIC QUANTITY	FLIGHT	WIND TUNNEL
PRESSURE, p'_0 (atm)	24.43	24.50
TEMPERATURE, T'_0 (°K)	8632	8730
DENSITY, ρ'_0 (ama)	0.4814	0.4704
SPECIES (MOLES/gm OF MIXTURE)		
N_2	1.289×10^{-2}	1.209×10^{-2}
O_2	9.153×10^{-6}	8.355×10^{-6}
N	2.767×10^{-2}	2.928×10^{-2}
O	1.401×10^{-2}	1.404×10^{-2}
NO	4.059×10^{-4}	3.804×10^{-4}
e^-	7.88×10^{-5}	8.740×10^{-5}
N_2^+	4.939×10^{-6}	5.580×10^{-6}
O_2^+	8.984×10^{-8}	9.255×10^{-8}
N^+	2.422×10^{-5}	3.004×10^{-5}
O^+	9.088×10^{-6}	1.055×10^{-5}
NO^+	4.051×10^{-5}	4.115×10^{-5}

Table V-3
COMPARISON OF STAGNATION-POINT CONDITIONS
Case III, $U_{\infty} = 35,000$ fps

THERMODYNAMIC QUANTITY	FLIGHT	WIND TUNNEL
PRESSURE, p_o' (atm)	0.6202	0.6199
TEMPERATURE, T_o ($^{\circ}$ K)	11,190	11,230
DENSITY, ρ_o' (ama)	0.0703	0.0698
SPECIES (MOLES/gm OF MIXTURE)		
H_2	2.642×10^{-5}	2.500×10^{-5}
O_2	3.136×10^{-8}	3.047×10^{-8}
N	4.901×10^{-2}	4.885×10^{-2}
O	1.365×10^{-2}	1.363×10^{-2}
NO	1.365×10^{-6}	1.313×10^{-6}
e^-	5.688×10^{-3}	5.883×10^{-3}
H_2^+	2.044×10^{-6}	2.024×10^{-6}
O_2^+	1.704×10^{-8}	1.703×10^{-8}
N^+	4.854×10^{-3}	5.020×10^{-3}
O^+	8.293×10^{-4}	8.573×10^{-4}
NO^+	3.369×10^{-6}	3.297×10^{-6}

In comparing the flight and wind-tunnel conditions it is seen that all of the thermodynamic state variables (p_0' , T_0' , and ρ_0') differ by less than 4 percent for the three cases. This is a direct result of the flow being Mach number independent. On the other hand, mismatches of up to 40 percent occur for the species concentrations but only in the case of species having very small concentrations. These large mismatches result from being in a temperature-density region where certain species concentrations are very sensitive to temperature (e. g., see Ref. 45).

2. Body Streamtube, Case I ($U_\infty = 15,000$ fps). Typical results of the body streamtube calculations for Case I are shown in Figs. 8 - 11. In each figure, the four curves represent the frozen, equilibrium and finite-rate (or nonequilibrium) solutions for the flight case. The symbols in these figures represent the nonequilibrium solutions for the wind-tunnel case. In these figures the results are shown as a function of distance along the cone surface in units of nose radii (S/R_N). When nondimensionalized in this manner, note that the frozen and equilibrium solutions are independent of body nose radius while the nonequilibrium solutions are not.

The temperature (T/T_0') is shown as a function of S/R_N in Fig. 8. Presenting the temperature as T/T_0' masks the effects of the small differences in T_0' between flight and wind tunnel, and emphasizes the differences resulting from the mismatch in M_∞ . Comparing the flight and wind-tunnel nonequilibrium solutions, it is noted that the temperature ratios T/T_0' differ by less than 10 per cent for either nose bluntness even though the free-stream Mach numbers differ by over 40 percent and the pressures along the cone differ by up to 25 percent (Fig. 7). The importance of flow chemistry and its dependence on nose bluntness are clearly evident in Fig. 8 when the flight solutions for frozen, finite-rate and equilibrium flows are compared. Note that along the cone the equilibrium temperature is about 60 percent higher than the frozen-flow temperature. Although equilibrium and frozen solutions are not presented for the wind-tunnel case, they lie about 10 percent above the corresponding flight solutions.

The density distributions (ρ/ρ_0') are shown in Fig. 9. In general, the density follows the same pattern as the temperature except that the

relative levels of the frozen and equilibrium solutions are inverted. Again, the wind-tunnel densities for nonequilibrium flow are within 10 percent of the corresponding flight values.

Along the spherical nose ($S/R_N \leq 1.4$), where the flow is Mach number independent, the wind-tunnel temperatures and densities are essentially identical to the flight values.

Although the velocity distributions are not shown, they increase rapidly along the spherical nose and lie between 60 percent and 70 percent of U_∞ along the conical afterbody for all cases. Typically, the wind-tunnel values lie about 1 percent to 2 percent above the flight case for nonequilibrium flow. The frozen-flow velocities are about 7 percent lower than the equilibrium velocities.

In examining the distributions of species concentrations, it is interesting to note that nonequilibrium distributions are not necessarily bounded by the frozen and equilibrium solutions as are the velocities and thermodynamic state variable (T and ρ). This is the case, for example, for nitric oxide (NO) which is shown in Fig. 10. The nonequilibrium concentrations fall below the frozen level while the equilibrium concentrations lie above the frozen-flow value. A comparison of the flight and wind-tunnel nonequilibrium concentrations indicates that the initial differences are approximately maintained up to the point where the concentrations start to approach equilibrium.

The atomic oxygen (O) concentrations shown in Fig. 11 are an example where the nonequilibrium case is bounded by the frozen and equilibrium distributions. The effect of nose bluntness is quite striking here. For $R_N = 0.2$ in., the oxygen atom concentrations essentially remain frozen at their initial value well downstream of the nose, while for $R_N = 1.5$ in. the concentrations show a steady decrease toward the equilibrium case.

At $U_\infty = 15,000$ fps, molecular nitrogen is relatively undissociated. The total variation from the stagnation-point concentrations is only 4 percent for all cases. The other species (N , O_2 , NO^+ and e^-) do not exhibit any unique behavior and are not presented either.

3. Conical-Shock Calculations, Case I ($U_\infty = 15,000$ fps). The relatively small variation in pressure, density and temperature between the conical shock wave and cone surface has been cited previously as the justification for comparing only the conditions just behind the conical portion of the shock wave for the wind tunnel and flight cases. This comparison is shown in the following table. For convenience, a comparison of some of the free-stream conditions are tabulated also. The subscript "s" refers to equilibrium conditions just behind the shock wave. For Case I, the effect of nozzle-flow nonequilibrium on the thermodynamic state variables is less than 1 percent and has not been considered here.

Table I-4
COMPARISON OF FREE-STREAM AND
CONICAL-SHOCK CONDITIONS
Case I ($U_\infty = 15,000$ fps)

PARAMETER	FLIGHT	WIND TUNNEL
M_∞	15.34	3.042
ρ_∞ (atm)	2.755×10^{-2}	8.134×10^{-2}
T_∞ (°K)	220.9	550.0
U_∞ (fps)	14,760	14,740
ρ_s (atm)	0.1250	0.0858
p_s (atm)	0.2519	0.3008
T_s (°K)	544.0	959.0

The above table indicates appreciable differences exist between the flight and wind tunnel flows downstream of the conical shock. Clearly, this flow is not Mach number independent as was the entropy-layer flow typified by the body streamtube calculation. In the present case, if $M_\infty \sin \theta_c$ rather than $U_\infty \sin \theta_c$ were matched between flight and wind tunnel, the shock ratios such as p_s/p_∞ , ρ_s/ρ_∞ , and T_s/T_∞ would be closely matched also. However, then the temperature behind the shock T_s in the wind tunnel would be about 1500 °K and real-gas effects would begin to be felt.

4. Body Streamtube, Case II ($U_\infty = 25,000$ fps). Typical results of the body streamtube calculations for Case II are shown in Figs. 12 - 16. The figures follow the same format as the set for Case I; namely, the four curves are for the flight cases and the two sets of symbols represent the nonequilibrium wind-tunnel cases ($R_N = 0.2$ in. and 1.5 in.). Again the abscissa in each figure is distance along the cone in units of nose radii (S/R_N).

The temperature distributions (T/T'_0) are shown in Fig. 12. The general features are the same as Case I (Fig. 8); the flight solutions orient themselves in the order equilibrium flow, nonequilibrium flow for the blunter nose ($R_N = 1.5$ in.), nonequilibrium flow for the sharper nose ($R_N = 0.2$ in.), and finally frozen flow. In comparing Case I and Case II, it is noted that for Case II the nonequilibrium solutions lie closer to the equilibrium solution than in Case I and actually attain the equilibrium levels, also the frozen and equilibrium solutions lie farther apart than in Case I. No simple explanation can be given for the closer agreement of the equilibrium and nonequilibrium solutions for Case II. It results from complex differences in the air chemistry for the two cases. Some of these differences will be noted in the discussion of the species concentrations. The larger differences between the frozen and equilibrium solutions in Case II compared to Case I occur because the higher stagnation-point temperature in Case II produces a greater degree of dissociation which is maintained in the frozen flow calculation.

Comparing the flight and wind-tunnel nonequilibrium solutions in Fig. 12, it is observed that the wind-tunnel temperatures are at most about 8 percent higher than the flight values. Referring to Fig. 7, it is noted that the pressures in the wind-tunnel case are 25 percent higher than the flight case and the free-stream Mach numbers differ by a factor of two.

The density distributions (ρ/ρ'_0) for Case II are shown in Fig. 13. The behavior is analogous to that of the temperature. The nonequilibrium solutions do not depart from equilibrium as much as in Case I while the frozen and equilibrium solutions are appreciably farther apart. Along the cone, the density levels in the wind-tunnel case are about 10 percent to 20 percent higher than in the flight case.

Typical species concentrations are shown in Figs. 14 - 16. Molecular nitrogen (N_2) is shown in Fig. 14. It is seen that in Case II, the nonequilibrium concentrations lie between the frozen and equilibrium levels. Also, the wind tunnel concentrations uniformly lie below the corresponding flight values by an amount essentially equal to the initial differences. Finally, the variation of N_2 concentrations along the cone is much greater than in Case I (60 percent versus 4 percent).

The nitric oxide (NO) concentrations, shown in Fig. 15, exhibit a somewhat different behavior from Case I (Fig. 10). The first notable difference is in the equilibrium case. In Case I, equilibrium chemistry resulted in a net production of NO above the initial concentration along the cone, whereas in Case II NO is consumed and falls below the initial concentration. The nonequilibrium solutions show an even greater reduction in NO concentration followed by a return to the equilibrium levels. For the blunter nose, the equilibrium chemistry produces fluctuations in the NO concentrations just downstream of the nose. These are observed in both the flight and wind-tunnel solutions. The agreement between the flight and wind-tunnel solutions is quite good up to about $S/R_N = 2$. After that, larger differences are noted until the final approach to equilibrium.

For Case II, oxygen is essentially fully dissociated and as a result the concentrations vary by less than 4 percent for all cases throughout the flow field. The concentrations lie in the range 1.40×10^{-2} to 1.45×10^{-2} moles/gm of mixture and are not shown.

The atomic nitrogen (N) concentrations are shown in Fig. 16. Like molecular nitrogen, the nonequilibrium concentrations lie between the frozen and equilibrium cases, and approach the equilibrium levels at large values of S/R_N . Also, the initial differences in concentration between the wind-tunnel and flight cases tend to persist throughout the flow. For brevity, the distributions of the other species are omitted.

5. Conical-Shock Calculations, Case II ($U_\infty = 25,000$ fps). For Case II, the differences in T_∞ , p_∞ and M_∞ between wind tunnel and flight are approximately twice as great as in Case I. In addition, the effects of nozzle-flow

nonequilibrium, while small compared to the mismatches in free-stream conditions, are not negligible as they were for Case I. In taking nozzle-flow nonequilibrium effects into account, two limiting cases exist: either the flow equilibrates immediately behind the conical shock or the composition remains frozen at the free-stream values. In both cases, the reduction in free-stream pressure and temperature due to nozzle nonequilibrium is more significant than the increase in M_∞ . As a result, the effect of nozzle-flow nonequilibrium is to improve the agreement between wind tunnel and flight. The following table compares free-stream and conical-shock conditions for the case of equilibrium nozzle flow and, hence, represents the maximum mismatches that could occur.

Table V-5
COMPARISON OF FREE-STREAM AND
CONICAL-SHOCK CONDITIONS
Case II ($U_\infty = 25,000$ fps)

PARAMETER	FLIGHT	WIND TUNNEL
M_∞	25.57	11.25
f_∞ (atm)	2.765×10^{-2}	1.513×10^{-1}
T_∞ (°K)	220.9	1203
U_∞ (fps)	24,625	24,580
ρ_3 (ama)	0.1737	0.1139
p_3 (atm)	0.6536	0.7907
T_3 (°K)	1032	1957

As in Case I, the differences between flight and wind-tunnel conditions are appreciable, although less than the free-stream differences. Again, if

$M_\infty \sin \theta_c$ rather than $U_\infty \sin \theta_c$ were duplicated in the wind tunnel, the shock ratios (p_3/p_∞ etc.) would be much closer. However, the temperature T_3 in the wind tunnel case would then be about 4000 °K and real-gas effects would be important.

6. Body Streamtube, Case III ($U_\infty = 35,000$ fps). Before presenting the calculated results for this case, a strong note of caution in accepting the absolute values as accurate must be made. At 180,000 ft altitude, the relaxation zone behind a normal shock wave at $U_\infty = 35,000$ fps is on the order of 1/2 inch thick¹ which is larger than the shock stand-off distance for both nose radii of interest. Furthermore, Fig. 3 indicates that low-density viscous effects will be present in the flow about the blunt nose. Also viscous interaction effects will exist in the flow along the conical afterbody. Thus, an accurate prediction of such a complex flow must include the combined effects of thermochemical nonequilibrium and viscous interactions both in the region of the blunt nose and along the conical afterbody. Undertaking such a solution was not felt justifiable in view of the relatively small differences between the flight and wind-tunnel free-stream flows at these velocity and altitude conditions (Table II-3). In fact, when the wind-tunnel free-stream conditions are corrected for the estimated nozzle nonequilibrium effects (Table II-4), the flight and wind-tunnel conditions are nearly identical. This is shown in the following table which compares flight conditions with equilibrium and estimated nonequilibrium wind-tunnel conditions.

Table II-6
COMPARISON OF FLIGHT AND WIND-TUNNEL CONDITIONS
Case III $U_\infty = 35,000$ fps 180,000 ft Alt.

PARAMETER	FLIGHT	EQUILIBRIUM WIND TUNNEL	NONEQUILIBRIUM WIND TUNNEL
VELOCITY, U_∞ (fps)	35,000	35,000	35,000
DENSITY, ρ_∞ (slugs)	4.413×10^{-7}	4.413×10^{-7}	4.44×10^{-7}
PRESSURE, p_∞ (atm)	4.292×10^{-7}	6.135×10^{-7}	4.294×10^{-7}
TEMPERATURE, T_∞ (°K)	265.9	380.0	255
MACH NUMBER, M_∞	32.63	27.34	33.1

Thus for Case III the primary difference between flight conditions and the wind tunnel, when nonequilibrium effects are taken into account, is in the composition of the test gas (Table II-4).

In order to show the maximum differences that could be expected for this case, the equilibrium wind-tunnel conditions have been used rather than the estimated nonequilibrium conditions. The body streamtube calculations were made in a manner completely analogous to the two preceding cases. The equilibrium stagnation-point conditions have been compared in Table V-3 and indicate very little difference between flight and wind tunnel. Thus, while the calculated results may not be quantitatively accurate the relative differences are probably representative of the actual flow situation. Typical results for Case III are presented in Figs. 17 to 20. As before frozen, nonequilibrium and equilibrium solutions are shown for the flight case (solid curves) and nonequilibrium solutions only for the wind-tunnel (symbols). The abscissa in each figure again is distance along the cone in units of nose radii.

The temperature distributions (T/T_0') shown in Fig. 17 are very much like those for Case I except that the difference between the frozen and equilibrium solutions is more pronounced. However, the wind-tunnel solutions are essentially identical to the flight solutions. This is to be expected in view of the small differences in free-stream conditions between wind tunnel and flight. Also, we note that the effect of nose radius on the nonequilibrium flow is much smaller for Case III than for Case II (Fig. 12).

The density distributions (ρ/ρ_0') for Case III are shown in Fig. 18. The behavior is very similar to Case II (Fig. 13) except that the wind-tunnel and flight solutions are in much better agreement than in Case II. Again, the very small effect of nose radius on the nonequilibrium flow is noted.

In the assumed equilibrium stagnation region for Case III, nitrogen and oxygen are essentially completely dissociated. Thus, atomic nitrogen is the dominant species and atomic oxygen is the second most abundant. Little recombination occurs in the expansion along the body so that the concentrations of these species do not vary greatly. The atomic nitrogen (N) concentrations are shown in Fig. 19, where it is noted that the total variation is less than 10% of the stagnation-point concentration. For equilibrium and nonequilibrium flow the variation of the concentrations with S/R_N is quite different in Case III than in Case II (Fig. 16). In Case II, both equilibrium and nonequilibrium

solutions showed a decrease in concentration along the body. In Case III, the nonequilibrium solutions show a general increase in atomic nitrogen concentration with increasing S/R_N , while the equilibrium solution yields a very nonmonotonic behavior. Because the atomic oxygen concentrations only vary $\pm 5\%$ from the stagnation-point concentration, they are not shown.

The atomic nitrogen is about 10% ionized at the conditions for Case III and is the largest source of electrons. The atomic nitrogen ion (N^+) concentrations are shown in Fig. 20. Within a distance of 100 nose radii the nonequilibrium concentrations decrease by a factor of 3 to 6 (depending on R_N) below the initial values, whereas the equilibrium solution shows a decrease of well over an order of magnitude. The electron concentrations show a similar behavior.

It can be seen in Table V-3 that the other species are much less abundant; hence, their concentrations are not shown.

7. Conical-Shock Calculations, Case III ($U_\infty = 35,000$ fps). Using the equilibrium wind-tunnel conditions, which provide the largest differences from the flight conditions, the equilibrium conditions behind a conical shock wave have been calculated and are shown in the following table. The differences are seen to be very small.

Table V-7
COMPARISON OF CONICAL-SHOCK CONDITIONS
Case III ($U_\infty = 35,000$ fps)

PARAMETER	FLIGHT	WIND TUNNEL
U_s (fps)	34,500	34,400
ρ_s (ana)	0.00258	0.00251
p_s (atm)	0.0161	0.0167
T_s (°K)	1710	1840

D. DRAG, SKIN-FRICTION AND HEAT TRANSFER COMPARISONS

The results of the preceding calculations can be used to estimate the drag, skin friction and heat transfer to a blunted 9° cone. The total drag consists of pressure drag and skin friction which are in turn influenced by contributions due to viscous interactions. Other influencing factors are boundary layer transition and the question of when the entropy layer near the body is engulfed by the boundary layer. Zakkay and Krause⁴⁶ have given a general expression for predicting this "swallowing" distance X_{SW} . Using their result the swallowing distance has been estimated for the conditions of present interest and is given in the following table.

Table V-8
ENTROPY LAYER SWALLOWING DISTANCE (X_{SW} , FT)

CASE	$R_N = 0.2$ IN		$R_N = 1.5$ IN		X_{SW}/R_N	
	FLIGHT	WIND TUNNEL	FLIGHT	WIND TUNNEL	FLIGHT	WIND TUNNEL
I	2.54	3.74	35	52	278	409
II	2.50	6.1	35	63	273	494
III	0.15	0.15	2.0	2.3	15.9	18.0

We note in all cases the swallowing distance for the wind tunnel case is equal to or greater than the distance for the corresponding flight case. Also, in terms of nose radii the swallowing distance is greater than the range of the results presented in Figs. 8-16 for Cases I and II. Boundary layer calculations based on the body streamtube results can be considered valid for distances less than the swallowing distance.

Clearly, accurate predictions of the total skin friction drag or total heat transfer to a blunted cone must take account of the transition of the boundary layer from laminar to turbulent flow. In the present study, however, our primary objective is a comparison of flight and wind tunnel flow fields. For this purpose we restrict our attention to the laminar boundary layer region only.

1. Pressure Drag. The effect of nose bluntness on the pressure drag of a cone is not dependent on R_N per se but rather on R_N/R_B and on the cone angle. Specifying R_N/R_B for a given cone angle θ_c implies that the length is known. If we take a length of 88 inches, then the nose radii of 0.2 in. and 1.5 in. correspond to $R_N/R_B = 0.015$ and 0.10. For a 9° cone and such small values of R_N/R_B , the pressure drag coefficient is essentially equal to that of a sharp cone⁴⁷ and the length is immaterial. We can then compare the sharp cone pressure drag coefficients for the three flight and wind tunnel cases considered here. As we have seen in Fig. 7 they will not be identical. The pressure drag coefficients obtained from the correlations reported in Ref. 44 are tabulated below.

Table V-9
PRESSURE DRAG COEFFICIENTS

CASE	FLIGHT	WIND TUNNEL
I	0.0528	0.0550
II	0.0518	0.0540
III	0.0516	0.0517

The differences between flight and wind tunnel are only 4% even when the free-stream Mach numbers differ by a factor of 2 (Case II).

2. Viscous Drag. At the low altitude condition (Cases I and II) boundary-layer transition must be considered. Although the local Reynolds numbers and Mach numbers obtained from the body streamtube calculations are such that one would not predict transition, once the entropy layer is swallowed by the boundary layer, transition would be predicted. The present calculations do not permit determining these details. One can make comparisons though for the portion of the cone where the boundary layer remains laminar assuming this region to be governed by the entropy layer.

Taub has correlated a large amount of wind tunnel data for blunted cones⁴⁸. He finds that the drag correlates as C_D versus U , where

$$\bar{C}_D = C_D / (1 + 0.375 \beta^2) \sin^2 \theta_c$$

and

$$\bar{U} = \frac{(1 + 0.4 T_w / T_o') \cos \theta_c}{(1 + 0.375 \beta^2) \sin^2 \theta_c} M_\infty \sqrt{C_x / Re_{L_\infty}}$$

where

$$\beta = \frac{R_n / R_\theta}{\sin \theta_c}$$

Here $C_x = \mu_x T_\infty / \mu_\infty T_x$ where $T_x = \frac{T_o'}{6} (1 + 3 T_w / T_o')$. Based on Taub's correlations, we observe that for the present conditions the drag coefficients obtained in the hypothetical wind tunnel would be the same as in flight if the wall temperature T_w were duplicated.

3. Skin Friction and Heat Transfer. For the laminar boundary layer region on a blunted slender cone, the heat-transfer distribution can be calculated by the local similarity method of Lees⁴⁹. For hypersonic flow over a blunt-nosed cone, Lees gives the ratio of the local surface heat-transfer rate to the stagnation-point heat transfer as

$$\frac{\dot{q}_w}{\dot{q}_o} = \frac{\frac{1}{2} \left(\frac{p}{p_o'} \right) \left(\frac{U_e}{U_\infty} \right) R}{\left[\int_0^S \left(\frac{p}{p_o'} \right) \left(\frac{U_e}{U_\infty} \right) R^2 ds \right]^{1/2}} \frac{\sqrt{R_n}}{\sqrt{\frac{1}{U_\infty} \left(\frac{d U_e}{d s / R_n} \right)_o}} \quad (V-1)$$

where

p = the local static pressure

p_o' = stagnation-point pressure

U_e = local inviscid flow velocity

U_∞ = free-stream velocity

R = cross-sectional radius of the body

S = distance along body surface

R_n = nose radius

$d U_e / d (S / R_n)_o$ = velocity gradient at the stagnation point

The body streamtube calculations can be used to compute \dot{q}_w / \dot{q}_o from Eq. V-1.

The result for Case II, which represents the largest mismatch in free-stream conditions is shown in Fig. 21a. We note that the distributions for equilibrium and frozen-flow differ by only 15 to 20 per cent along the cone. The insensitivity to chemistry is further borne out by the closeness of the nonequilibrium flow curves for the two nose radii. Along the cone wind tunnel values of \dot{q}_w/\dot{q}_∞ are about 10% higher than the flight case.

Use of Eq. V-1 implies a fully catalytic wall. In this case there is little influence of chemical reactions in the boundary layer on surface heat transfer¹. Inger⁵⁰ has shown that blunt bodies having a metallic-type surface behave as very nearly perfectly catalytic at all altitudes below 300,000 ft for $U_\infty = 26,000$ fps. Therefore, the present results are deemed reasonable.

Skin-friction distributions can be obtained from the heat-transfer distributions through the modified Reynolds analogy relation

$$C_H = \frac{1}{2} C_f P_r^{-2/3} \quad (V-2)$$

where

$$C_H = \dot{q}_w / \rho_e U_e (H_{adw} - H_w)$$

$$C_f = \tau_w / \frac{1}{2} \rho_e U_e^2$$

$$P_r = \text{Prandtl number}$$

$$\rho_e = \text{inviscid-flow density at edge of boundary layer}$$

$$H_{adw} = H_e + \frac{1}{2} P_r^{-1/2} U_e^2, \text{ the adiabatic-wall enthalpy}$$

$$H_w = \text{static enthalpy at the wall}$$

$$\tau_w = \text{shear stress at the wall}$$

Computations of C_f based on Eq. V-2 and the results contained in Fig. 21a are shown in Fig. 21b for Case II. The frozen and equilibrium flow distributions are shown only for the flight case with $R_N = 0.2$ in. The corresponding distributions for $R_N = 1.5$ in. can be obtained from these curves by multiplying by the ratio of the stagnation-point heat-transfer rates. The difference between the equilibrium and frozen-flow curves varies between 15% and 25% along the body. The nonequilibrium wind-tunnel results are in good agreement with the corresponding flight case for both nose radii. In these calculations the wall temperatures have been taken as 1000 °K for the flight cases and

300 °K for the wind tunnel cases. Thus, the sensitivity to wall temperature is weak.

The stagnation-point heating rates calculated for Case II are given in the following table.

Table V-10

STAGNATION-POINT HEAT TRANSFER
Case II $U_\infty = 25,000$ fps 80,000 ft Alt.

R_N (IN.)	\dot{q}_o (BTU)/FT ² -SEC	
	FLIGHT	WIND TUNNEL
0.2	19,700	21,900
1.5	7340	8160

The higher heat transfer for the wind tunnel is a result of the higher total enthalpy required to provide velocity and density altitude duplication. It was shown in Ref. 1 that duplicating total enthalpy and density altitude leads to smaller differences in stagnation-point heat transfer. Recalling that \dot{q}_w/\dot{q}_o for the wind tunnel case was about 10% higher than the flight case (Fig. 21a), the higher values of \dot{q}_o in the wind tunnel will result in actual surface heating rates that are about 22% higher in the wind tunnel than in flight.

E. SUMMARY

In this section, a comparison has been made of wind tunnel and flight flow fields about a blunted slender cone at three flight conditions. The effects of flow-field nonequilibrium and nose bluntness have been investigated as well as the effects of appreciable differences in free-stream pressure, temperature and Mach number. A hypothetical wind tunnel performance (Fig. 2) was used to define test-section conditions. The comparisons have been restricted to the body streamtube, to conditions behind the conical portion of the bow shock wave, and to other results derivable from these flow conditions. It has been assumed that the flight free-stream density and velocity were duplicated in the hypothetical wind tunnel and that the bodies were geometrically identical - both requirements of the Mach number independence principle when dissipative

effects are present.

Because ρ_∞ and U_∞ were duplicated, and since the free-stream Mach numbers were fairly large, the Mach number independence principle indicates that the flow in the region of the blunt nose should be the same for both the flight and wind tunnel cases. A comparison of the stagnation-point conditions and the distributions of the various quantities along the spherical nose indicates that this is indeed the case.

In reviewing Cheng's extension of hypersonic small-disturbance similitude to real gases (Sec. IV), we have pointed out that, when the free-stream thermodynamic state is not duplicated, it is preferable to replace Mach number with free-stream velocity in the similitude parameters. Thus, in the present study, $U_\infty \sin \theta_c$ and $U_\infty^2 \sqrt{C_{D_N}} \, d\nu/\chi$ are duplicated rather than $M_\infty \sin \theta_c$ and $K_N = M_\infty^2 \sqrt{C_{D_N}} \, d\nu/\chi$ as given by Cheng. This has resulted in relatively small differences in the flight and wind-tunnel flows along the conical afterbody when the quantities are referenced to stagnation-point conditions rather than free-stream conditions. The overall effects of the large mismatches in p_∞ ,

T_∞ and M_∞ are to produce 25 percent to 35 percent differences in the pressure ratio p/p' , up to 8 percent differences in temperature ratio T/T' and up to 20 percent differences in density ratio ρ/ρ' at a given distance along the conical afterbody (Figs. 7-9, 12, 13, 17, 18).

It may be concluded that the entropy-layer flow is relatively insensitive to mismatches in p_∞ , T_∞ and M_∞ . On the other hand, it has been shown that conditions behind the conical shock wave are much more sensitive to mismatches in the above parameters for the cases considered here.

Finally, the drag, skin friction and heat transfer for the case of a laminar boundary layer growing within the entropy layer have been investigated. Again the flight and wind tunnel solutions show relatively small differences; however, the turbulent boundary-layer case, which most likely is governed by the shock layer flow outside the entropy layer, has not been investigated.

SECTION VI
ANALYSIS OF THE COMBINED EFFECTS OF NOSE BLUNTNES
AND NONEQUILIBRIUM ON SLENDER-BODY FLOWS

A. INTRODUCTORY REMARKS

The purpose of the present section is to develop a theoretical model for the study of the combined effects of nose bluntness and nonequilibrium on slender-body flows. The studies in this section are concerned with flight conditions at higher altitudes where the assumed performance of the hypothetical wind tunnel under consideration is such that it could fully duplicate the ambient altitude thermodynamic state if there were no nozzle nonequilibrium effects. The major part of the present analysis is confined to the treatment of inviscid flows; however, viscous effects are subsequently accounted for through a boundary-layer approach.

One of the primary objectives of the present analysis is to check the influence of nonequilibrium effects on the pressure distributions on blunt nosed slender bodies. It will be recalled that in the phase I part of the present study (which was concerned with flight conditions below the assumed full-duplication boundary), it was assumed that the pressure distribution was insensitive to real-gas effects. However, in the flight regime of present interest this assumption is questionable. For example, Whalen⁵¹ studied the case of a wedge-nosed flat plate and found that freezing through the Prandtl-Meyer expansion would produce pressures on the afterbody that were significantly lower than the pressures for the equilibrium or perfect-gas cases.

B. REVIEW OF BLUNT NOSED SLENDER BODY FLOWS

We will now review the existing theoretical analyses for predicting the flow fields around blunt nosed slender bodies. However, no exhaustive review will be attempted here since several comprehensive reviews of the various aspects of the problem are available (Mirels⁵², Guiraud, Vallee and Zolver⁵³, Hayes and Probstein⁵⁴, Cox and Crabtree⁵⁵, Cheng⁵⁶,

Chernyi³², Sedov⁵⁷, Stanyukovich⁵⁸, Probst⁵⁹ and Lees⁶⁰). On the other hand we will review the analyses that are directly relevant to the present study in some detail.

Most analytical studies of blunt nosed slender bodies are based on either an explicit or implicit use of the hypersonic equivalence principle of Hayes²⁴. In general, use is also made of the hypersonic small disturbance approximations^{61,23} and the Newtonian slender body approximations⁶². The analogy between the flows past blunted slender bodies and the unsteady flows due to strong explosions was pointed out independently by Cheng and Pallone⁶³, and Lees and Kubota⁶⁴. These authors obtained the solutions for steady hypersonic flows past blunted flat plates and cylinders by applying the equivalence principle to the corresponding unsteady flow problems of explosions with cylindrical and spherical symmetries. The solutions to unsteady problems had been obtained earlier by Lin⁶⁵, Taylor⁶⁶, Sedov⁶⁷ and Sakurai⁶⁸. Other authors⁶⁹⁻⁷¹ have studied the unsteady 'similar' flows corresponding to shock waves propagating according to various power laws and the corresponding steady flows past equivalent power-law bodies. An approximate method of solving for flows past power-law bodies has been given by Mirels⁷², and Mirels and Thornton⁷³ have investigated bodies associated with shock shapes which deviate slightly from a power law.

The method of generating solutions for flows past power-law bodies from equivalent unsteady, similar flows is not applicable to the flows past blunted wedges and cones since these flows are basically nonsimilar. That is, the time evolution of the flows in the unsteady cases, and the space evolution of the flows in the steady cases, do not obey similarity requirements. Chernyi^{32, 74-76} and Cheng³¹ have developed approximate methods to study the flows past blunted wedges and cones.

The method used by Chernyi is an integral one in which the conservation relations of mass, momentum and energy are applied in an integral form across the disturbed region between the body and the shock wave. The effect of the blunt nose on the flow downstream of it is assumed to be describable in terms of an energy in the energy conservation equation and an impulse in the normal

momentum conservation equation. He further assumes that the bulk of the disturbed gas is concentrated in a thin region next to the shock wave, and obtains approximate solutions for the flows past blunted wedges and cones. Chernyi^{77, 78} has also described general integral formulations applicable to hypersonic flows containing strong shock waves.

The approach used by Cheng³¹ is somewhat different in that he accounts for the so-called 'entropy layer' in a specific way. The entropy layer consists of those streamlines which have crossed the nearly normal portions of the shock wave and are associated with much larger values of entropy than the streamlines which have crossed the more oblique (and therefore weaker) parts of the shock wave. By making estimates of the relative orders of magnitudes of the various flow quantities within and outside the entropy layer, Cheng was able to reduce the partial differential equations governing the problem to a single ordinary differential equation relating the pressure distribution on the body to the cross-sectional area of the entropy layer. This differential equation can be solved for the shape of the outer edge of the entropy layer (and the body pressure distribution) by assuming that the pressure distribution is related to the shape of the entropy-layer edge through the Newton-Busemann pressure distribution law. Thus Cheng's approach clearly brings out the fact that the influence of a blunt nose on the flow downstream of it appears essentially as a displacement effect.

The analyses of Chernyi and Cheng are both based on thin-shock-layer concepts, that is, both these methods utilize the fact that a major portion of the disturbed gas is concentrated in a thin region close to the shock wave. The thin-shock-layer approximation becomes progressively more accurate as the specific heat ratio, γ , of the gas approaches unity. In fact, as far as the leading approximation for small $\epsilon = (\gamma - 1) / (\gamma + 1)$ and $(M_0)^{-2}$ is concerned, the two analyses are identical; they differ only when higher-order approximations are considered. There seems to be some disagreement in the literature regarding the relative accuracies of the two methods. Thus Cheng³¹ states that Chernyi's method is unlikely to lead to consistent higher-order approximations, while Hayes and Probstein⁵⁴ argue that Cheng's method will be less accurate (than Chernyi's) since he uses the Newton-Busemann

pressure formula in terms of the entropy-layer edge rather than the shock shape. The approach we shall adopt for the present analysis will be a hybrid one incorporating features from both methods.

A method similar to that of Chernyi has also been used by Luniev⁷⁹. Several authors⁸⁰⁻⁸³ have also investigated the validity of the 'blast-wave analogy'. The requirements for the validity of the equivalence principle fail not only in the vicinity of the blunt nose, but also in the high-entropy layer next to the body. Thus, when the effect of a blunt nose on the flow downstream of it is replaced by that of a concentrated energy release at the nose, the density and temperature distributions near the body are predicted incorrectly. However, within the accuracy of the assumptions made by Cheng³¹, the velocity and pressure fields are predicted satisfactorily throughout the whole flow field.

All the analyses described above are applicable only for the perfect-gas case, that is, for the case in which the specific heat ratio is constant throughout the whole flow field. There are very few analyses in the literature which are applicable to the real-gas flows past blunt-nosed slender bodies. Cheng²⁵ has described a similitude for equilibrium real-air flows past slender bodies, and this similitude has been extended to nonequilibrium flows by Inger²⁶. Analyses which are valid for special geometries and simplified flow chemistries have been reported by Luniev⁸⁴, Whalen⁵¹ and Vagallo-Laurin and Bloom⁸⁵.

Analyses of the combined effects of nose bluntness and boundary layer displacement effects have been reported by Cheng³¹, Oguchi⁸⁶ and others. The similitude requirements for viscous slender body flows with and without nose bluntness effects have been considered by Hayes and Probst³⁰, Luniev^{87, 88} and Cheng³¹. Numerical solutions for the blunt-leading-edge problem have been reported by Van Hise⁸⁹ for the perfect-gas case, by Feldman⁹⁰ for the equilibrium flow case and by Curtis and Strom⁴⁰ for the nonequilibrium flow case.

C. FORMULATION OF A THEORETICAL MODEL

In the present section we will formulate a theoretical model to study the combined effects of nose bluntness and flow nonequilibrium on slender body flow fields. The model described is considered to be the one most likely to further qualitative understanding of the problem and at the same time give reasonable quantitative answer. For the inviscid case, following the practice in the perfect-gas analyses, the flow field downstream of the blunt nose is divided into an inner low-density entropy layer near the body and an outer shock layer. The entropy layer consists of streamlines crossing the nearly normal portion of the shock wave in the vicinity of the blunt nose, while the shock layer consists of streamlines crossing the more oblique and weaker parts of the shock wave. It is clear that because of the relatively larger values of the entropy and lower values of the density in the entropy layer, nonequilibrium effects are more likely to be important there. In the proposed simplified model the nonequilibrium effects will be accounted for only in the entropy layer, and the outer shock layer will be assumed to be described by the classical Newtonian shock layer theory.

The accuracy of the assumption that real-gas effects are more important in the entropy layer than in the shock layer can be verified as follows: For the sake of simplicity let us consider the case when the flow is assumed to be in equilibrium everywhere. Then, an estimate of the relative importance of real-gas effects in the entropy and shock layers can be obtained by comparing the dissociation fractions at the body and immediately behind the shock wave for various axial locations. For the purpose of the present study, the dissociation fraction, α , for air can be assumed to be equal to $Z-1$ where Z is the compressibility factor.

Consider the blunt-nosed slender body shown in Fig. 22. The notation that we shall adopt is also shown on this figure. All the flow quantities in the nose region will be denoted by the subscript 'n' while all the quantities on the body and immediately behind the shock wave will be denoted by the

subscripts 'b' and 's', respectively. The symbol 'e' will be used to denote the edge of the entropy layer* while the subscript ' ∞ ' will be used to indicate free-stream values.

Now, because of the equilibrium assumption, the flow will be particle isentropic, and the entropy on the body will be that corresponding to conditions behind a normal shock wave at the same free-stream conditions. Also, for order of magnitude estimates, we may assume that the pressure on the body is of the same order as that behind the shock wave at the same axial location, i. e. $p_b = O(p_s)$. Hence, for a given set of free-stream conditions, an estimate of the dissociation fraction on the body downstream of the blunt nose can be obtained by reading off a Mollier diagram for air the value of α_b corresponding to the pressure p_s and the entropy S_π . Figure 23 shows a comparison of the dissociation fraction on the body and behind the oblique shock wave for various axial locations (corresponding to different values of the local shock angle) and for various free-stream conditions.** It can be seen from the figure that the dissociation fraction on the body is always much larger than the dissociation fraction behind the oblique shock wave, and that the dissociation levels behind the shock wave reach significant levels only at very high velocities and altitudes. Even at the higher velocities and altitudes it can be seen that the dissociation levels in the shock wave are small for local shock inclinations of 20° or less. Thus, for slender bodies the real-gas effects in the shock layer will be small a few nose radii downstream of a blunt nose. On the other hand, real-gas effects will always be relatively more important in the entropy layer (for

* We will not use any explicit specification of the edge of the entropy layer, since this is not necessary within the context of the present analysis. Cox and Crabtree⁵⁵ define the edge of the entropy layer as being composed of that streamline whose local inclination after crossing the shock wave is approximately 20° . Other definitions have also been used in the literature.

** The equilibrium normal shock wave parameters reported in Ref. 91 were used in these calculations. Ref. 91 uses the 1959 ARDC model atmosphere.

the ranges of free-stream conditions under consideration) even for small values of the local shock-wave inclination.

It should be pointed out that, even though the above estimations were made only for the case of fully equilibrium flow, the conclusions will be valid even when the flow is not in equilibrium. This is because in nonequilibrium flow the dissociation fractions on the body will be higher than the corresponding equilibrium values since the relaxation process here is essentially one of recombination. Therefore, at any axial location downstream of the blunt nose, the dissociation fractions in regions close to the body will always be higher than those in regions close to the shock wave. Henceforth we will assume that nonequilibrium effects are important only in the entropy layer and we will approximate the region outside the entropy layer by a constant specific heat ratio, ideal-gas region.

Before we can proceed with estimations of the relative magnitudes of the other flow variables within the entropy and shock layers, it is necessary to formulate a simplified model for the flow chemistry. Because of the extremely complicated nature of physical-chemical processes involved in hypersonic flows past even such simple bodies as spherically blunted slender cones, some simplifying assumptions have to be resorted to. Several such simplifying assumptions have been used in the literature. One of the more commonly used approximations is to assume that the flow remains effectively in equilibrium along each streamline up to some suitably chosen boundary and that the gas composition 'freezes' (and remains frozen) subsequently along each streamline at the value corresponding to that at the boundary. For example, Whalen⁵¹ has studied the hypersonic flow past a wedge-nosed flat plate by assuming that the gas composition is constant along each streamline and is given by the equilibrium value immediately behind the shock envelope. In Refs. 1 and 2 the influence of real-gas effects on the sensitivity of various afterbody flow quantities of a sharp-nosed slender body to mismatches in free-stream conditions was studied by assuming that the flow was in equilibrium in the nose region and subsequently freezes at the junction of the nose and the afterbody. In Ref. 1 this model was termed the equilibrium-frozen model.

When there exists a sharp discontinuity in the body slope in the shoulder region between the nose and the afterbody, then it is logical to assume that the boundary between the equilibrium and frozen flow regions passes through this sharp corner since the flow experiences a rapid expansion in this region. Thus, for the flows past wedge-nosed flat plates or conical-nosed cylinders, one can assume that the flows remain in thermodynamic equilibrium upstream of the expansion fan emanating from the sharp shoulder junction and that they freeze downstream of it. Such a logical choice does not exist when there is no sharply defined boundary between the nose and the afterbody as is the case, for example, with spherically blunted cones.

Vaglio-Laurin and Bloom⁸⁵ have studied the influence of real-gas effects on the flowfields past several typical body shapes by using a simplified model for the flow chemistry. In this model, the authors assume that the flow chemistry remains frozen downstream of the forward facing characteristic that intersects the body at the sonic point; upstream of this characteristic the flow is assumed to remain in chemical equilibrium. Vaglio-Laurin and Bloom also assume that the gas composition remains constant (at the values corresponding to the equilibrium values behind the shock wave) along the streamlines that cross the shock wave downstream of the characteristic mentioned above. With the above assumptions, Vaglio-Laurin and Bloom have integrated the simplified differential equations governing the problem by using the method of characteristics, and they have obtained the distributions of various flow quantities on the body as well as the shock layer.

In support of their sonic-point-freezing assumption, Vaglio-Laurin and Bloom point out that for typical reentry configurations flying at high velocities and at altitudes in excess of 125,000 feet the flows indeed show a strong tendency to freeze at or near the sonic point on the body. Moreover exact numerical calculations, such as the ones performed by Feldman⁹⁰ for an equilibrium flow over a blunt nosed slender body, indicate that the gas close to the body at the sonic point expands drastically as it flows around the body. In fact, Feldman gives an example in which a streamline which is

only a distance of 0.012 nose-radii away from the body upstream of the sonic line eventually ends up 2 nose-radii away from the body when far downstream of the nose. This drastic expansion around and beyond the sonic region will, of course, tend to freeze the flow chemistry along streamlines close to the body beyond the sonic point.

In the present analysis we will assume that the flow chemistry within the entropy layer freezes (and remains frozen) downstream of the sonic point station. It should be recalled here that in the present model the flow outside the entropy layer is assumed to behave like an ideal gas (with a specific heat ratio equal to that of the free stream). On the other hand, in the models used by Whalen⁵¹ and Vaglio-Laurin and Bloom⁸⁵, the authors assume that in addition to the flow being frozen downstream of a specified boundary, the gas composition remains constant (at the values corresponding to equilibrium values immediately behind the shock) along all streamlines that cross even the relatively weaker portions of the shock wave. This difference between the assumptions of the above authors and those of the present model is important since it will be crucial to the analysis that follows.

Having formulated a simplified model for the flow chemistry, we can now proceed to make estimations of the various flow quantities within the entropy layer. One of the crucial assumptions involved in the so-called thin-shock-layer theories is that the density within the entropy layer in general, and on the body in particular, is much smaller than the free-stream density. This assumption can be checked for the present model in fairly general terms without any specific considerations of the nose or body shapes.

Now, for a given set of free-stream conditions, the entropy behind the shock wave, as well as the pressure at the stagnation point, can be determined from equilibrium-normal-shock tables⁹¹. Also, since the flow in the nose region is assumed to be in equilibrium and since the pressure distribution in the nose region is fairly insensitive to real-gas effects, one can calculate the pressure at the sonic point by using the isentropic-expansion relations with the specific heat ratio, γ equal to 1.4. That is, one can use the relation $P_p = 0.528 P_{st}$, where the subscripts 'p' and 'st' refer to the

sonic point and stagnation point, respectively. Since the entropy and the pressure at the sonic point are known, all other state variables can be easily read off a Mollier diagram; in particular, the density and the effective dissociation fraction at the sonic point can be determined.

In the present model the flow within the entropy layer is assumed to freeze downstream of a line passing through the sonic point on the body. Thus the expansion along the body surface will take place with an (constant) effective specific heat ratio determined by the conditions at the sonic point. Following Whalen⁵¹, this effective specific heat ratio will be taken to be

$$\gamma_f = \frac{3\alpha_{s_0} + 7}{\alpha_{s_0} + 5} \quad (\text{VI.1})$$

The density distribution along the body corresponding to a given pressure distribution can then be determined by using the isentropic relation

$$\rho_b = \rho_{s_0} \left(\frac{p_b}{p_{s_0}} \right)^{\frac{1}{\gamma_f}} \quad (\text{VI.2})$$

Fig. 24 shows a plot of the variation of density with the free-stream velocity (at an altitude of 200,000 ft) for the station on the body at which $p_b \approx p_\infty$. It can be seen from the figure that the density at this station is always considerably smaller than the free-stream density. The smallness of the density on the body is, of course, a direct consequence of the large (compared to free stream) value of the entropy along the body streamline. For the same reason, the density within the entire entropy layer will also be much smaller than the free-stream value.

It follows immediately that the low-density entropy layer will be incapable of supporting any transverse pressure gradients, and that the pressure at any axial station within the entropy layer can be taken as equal to the value at the outer edge of the entropy layer. It also follows from simple mass-flow arguments that the cross-sectional area of the shock layer will be much smaller than that of the entropy layer. These are the criteria that are necessary for the successful application of thin-shock-layer methods for the present problem.

Before the proposed model can be utilized to study the problem, it is also necessary to reexamine the validity of the equivalence principle for the present case, since the assumption of its validity is implicit in both the methods of Cheng³¹ and Chernyi⁷⁴⁻⁷⁶. Inger²⁶ has pointed out that the equivalence principle has very general validity within the framework of the assumptions of small-disturbance theory, and that it is valid for nonequilibrium flows irrespective of the form of the equation of state and the reaction rates. The small-disturbance approximations are, of course, based on the assumption that $u \approx u_\infty$ and $\sin \sigma \approx \sigma$. However, as has been pointed out by Whalen⁵¹, the validity of the former of the two assumptions is dependent on the value of the dissociation fraction, since the energy conservation relation can be written in the form

$$\alpha D + \frac{u^2}{2} \approx \frac{u_\infty^2}{2} \quad (\text{VI. 3})$$

Thus the assumption that $u \approx u_\infty$ will be valid only in those regions of the flow in which the energy contained in the dissociation mode is small compared to the free-stream kinetic energy.

Since in the present model real-gas effects are not considered in the shock layer, the assumption $u \approx u_\infty$ will be valid within the shock layer to the same degree of approximation that it is valid in the corresponding ideal-gas case. Cheng³¹ has shown that for the ideal-gas case the assumption $u \approx u_\infty$ will be valid if $\frac{1}{2} \sigma^2 \frac{\gamma-1}{\gamma}$ is negligible compared to unity, where σ can be a typical shock or flow angle. In the present model, the above requirement should also ensure the validity of the equivalence principle within the shock layer. However, it is clear that in regions close to the wall the approximation $u \approx u_\infty$ cannot be valid, since the dissociation fractions in these regions need not be small. However, this per se does not introduce additional complications, since the equivalence principle fails in regions close to the body even in the ideal-gas case. However, as is well known, the pressure field on the body and the shock shape are still predicted correctly in spite of this local failure of the equivalence principle.

To summarize briefly, the proposed model is such that real-gas effects

are included when calculating the displacement effect of the nose bluntness and the resulting effective body shape, but not in calculating the evolution of the shock wave due to this effective body shape. In other words, the outer edge of the entropy layer is related to the body shape including real-gas effects, but the shock-wave shape corresponding to the outer edge of the entropy layer is calculated using the classical Newton-Busemann relations.

The various approximations and restrictions that apply to the present analysis are listed below.

- a) The flow outside the entropy layer is assumed to behave like that of a perfect gas with a specific heat ratio equal to the free-stream value. The flow inside the entropy layer is particle isentropic, but the specific heat ratio is different on different streamlines.
- b) The flow is assumed to remain in chemical equilibrium in the nose region and subsequently freeze along a line passing through the sonic point on the body.
- c) The pressure distribution on the blunt nose is assumed to be given by the modified Newtonian pressure formula.
- d) The free-stream is assumed to be homogeneous in flow properties and undissociated.
- e) The local streamline inclination to the free-stream direction is assumed to be small everywhere except in a small region near the nose.
- f) The vibrational degree of freedom is assumed to remain in equilibrium with the translational temperature within the entropy layer.
- g) The ratio of specific heats is assumed to be sufficiently close to unity so that terms of order $\frac{\gamma-1}{\gamma+1}$ can be neglected.

D. A RESTRICTED SIMILITUDE APPLICABLE TO REAL-GAS FLOWS PAST BLUNTED SLENDER BODIES

As pointed out earlier, a similitude applicable to equilibrium flows past blunt-nosed slender bodies was given by Cheng²⁵, and this was extended to nonequilibrium flows by Inger²⁶. The similitude developed by Cheng requires that for proper similitude between two flows past two geometrically similar bodies, the hypersonic similarity parameter, $u_\infty \gamma$, a bluntness parameter, as well as the free-stream thermodynamic state have to be the same. The last of these conditions is quite stringent, and the free-stream thermodynamic state corresponding to low-altitude, hypervelocity flight cannot be reproduced in existing test facilities, except perhaps in such advanced (and as yet in a developmental stage) facilities as the Isentropic Compression Tube^{92, 93}. Therefore, it would be extremely useful if even a restricted similitude can be developed in which the requirement of the duplication of the free-stream thermodynamic state can be relaxed. Such a similitude will be derived in the present section.

Now Cheng's similitude (for the pressure field) for a blunt-nosed slender body in an equilibrium flow can be written as

$$\frac{p}{p_\infty} = f \left(\frac{x}{L}, \frac{y}{rL}; u_\infty \gamma, u_\infty^{\frac{3+\gamma}{1+\gamma}} k^{\frac{1}{1+\gamma}} \frac{d}{L}, \rho_\infty, T_\infty \right). \quad (\text{VI. 4})$$

In the above equation L is a characteristic body length, γ is the thickness ratio, k is the nose drag coefficient, and the free-stream has been assumed to be undissociated for the sake of simplicity.* The quantity γ is to be taken as zero for two-dimensional flows and unity for axisymmetric flows.

In the above similitude the requirement of duplication of the free-stream temperature becomes unnecessary, by virtue of the Mach-number-

* In principle, free-stream dissociation can be accounted for without additional difficulties. For example, it might be possible to use the 'Subtraction Rule' concept developed by Gibson⁹ in conjunction with the present formulation.

independence principle, in the limit when $u_\infty \tau \rightarrow \infty$ (or more appropriately, when $M_\infty \tau \gg 1$). In this case, the similitude reduces to

$$\frac{p}{\rho_\infty u_\infty^2 \tau^2} = f\left(\frac{x}{L}, \frac{y}{\tau L}; u_\infty \tau, u_\infty^{\frac{3+\gamma}{1+\gamma}} k^{\frac{1}{1+\gamma}} \frac{d}{L}, \rho_\infty\right) \quad (\text{VI. 5})$$

Alternately, when $M_\infty \tau = o(1)$, the real-gas effects become negligible throughout the flow field, and the similitude becomes

$$\frac{p}{p_\infty} = f\left(\frac{x}{L}, \frac{y}{\tau L}; M_\infty \tau, M_\infty^{\frac{3+\gamma}{1+\gamma}} k^{\frac{1}{1+\gamma}} \frac{d}{L}\right) \quad (\text{VI. 6})$$

In the intermediate region where $M_\infty \tau$ is neither so large that the Mach-number independence principle becomes operable, nor so small that real-gas effects can be neglected, the full similitude given by Eq. VI. 4 has to be used. However, it was shown in Section III that for a significant range of free-stream conditions, the real-gas effects are important only in part of the flow field, and that the remainder of the flow field behaves like an ideal gas one. Thus in the flow past a blunt-nosed slender body, the displacement effect due to the blunt nose is influenced by real-gas effects while the evolution of the shock wave due to the resulting effective slender-body shape is not. Heuristically it would appear that the above observation should lead to a simplification of the similitude given in Eq. VI. 4. We will now investigate this possibility.

It should be pointed out here that many of the restrictions that were prescribed for the model formulated in the previous section are not necessary for the derivation of the similitude given below (these restrictions are necessary only for the development of the zeroth-order theory given in the next section). For example, the ratio of the specific heats need not be close to unity, and the nose pressure distribution need not be of any specified form. Also, the derivation given below is not restricted to any specific model for the flow chemistry within the entropy layer. In particular, the analysis will be valid both for the case when the flow is assumed to be in equilibrium throughout the entropy layer, and for the case when the flow is in equilibrium in the nose region and freezes downstream of some point near the nose-afterbody junction. The

above two models have been termed equilibrium-equilibrium and equilibrium-frozen models in Refs. 1 and 2. The primary requirement for the validity of the similitude described below is that real-gas effects be important only in the high-entropy layer close to the body and that they be negligible outside this layer.

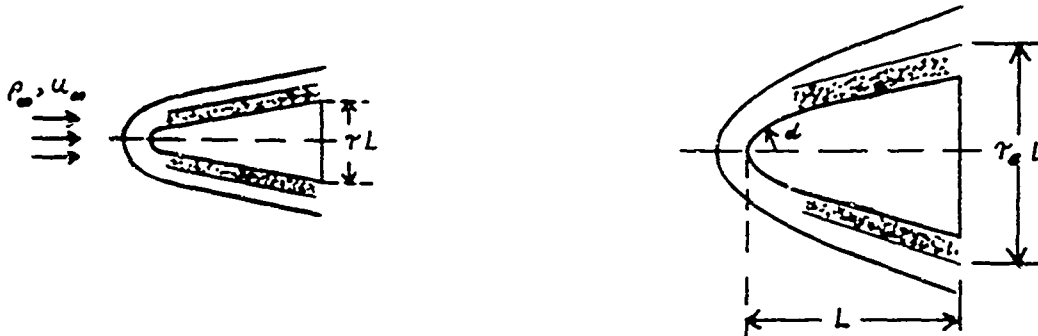
Before we proceed, one other point needs to be made here. Cheng's similitude²⁵ for blunt-nosed slender bodies is based on the postulate that the downstream influence of a blunt nose is equivalent to that of a concentrated force of appropriate magnitude applied at the nose in a direction transverse to the free-stream direction. The magnitude of the force is assumed to be determined uniquely by the nose drag coefficient and is independent of the detailed nose shape. Therefore, like the blast-wave analogy itself, the similitude is necessarily asymptotic in nature and becomes applicable only at a considerable distance downstream of the blunt nose. However, in many practical problems similitude is required not only in the region considerably downstream of the nose, but in the nose region itself. In such cases Eq. VI.4 is, of course, inadequate.

Similitude in the nose region can be assured by invoking the Mach-number-independence principle. Thus, for the nose region one can write (assuming geometrically similar boundaries),

$$\frac{p}{\rho_{\infty} u_{\infty}^2} = f\left(\frac{x}{d}, \frac{y}{d}; \rho_{\infty}, u_{\infty}\right) \quad (\text{VI. 7})$$

The simultaneous requirement of the conditions in Eqs. VI.4 and VI.7 implies that essentially no similitude exists; that is, the quantities ρ_{∞} , T_{∞} , u_{∞} and γ have all to be duplicated simultaneously. The only freedom of choice that exists is in connection with the length scale L , and even this freedom is lost if nonequilibrium effects or viscous effects are important. For such cases, a similitude which relaxes the requirement of the duplication of the free-stream temperature would be of great interest.

Consider two blunt-nosed slender bodies (shown below) which have geometrically similar nose and afterbody shapes, but are characterized



by different nose radii, thickness parameters, characteristic lengths and are immersed in different hypersonic flows. Now, as mentioned earlier, the downstream effect of a blunt nose on the afterbody flow field appears essentially as a displacement effect. This displacement is, of course, dependent on the initial conditions at the nose as well as on the afterbody shape. The conditions at the nose can be made identical for the two cases by requiring that the free-stream density and velocity be the same for both. Then, by virtue of the Mach-number-independence principle, all quantities in the nose region of the two bodies will be not merely similar but identical. In particular, the nose drag (and therefore the energy and impulse imparted to the transverse flow field) will scale in a simple geometric way.

Note that the above statements hold true whether or not the flow in the region of the nose is in chemical equilibrium, and whether or not the flow is assumed to freeze at some point in the neighborhood of the sonic point. Irrespective of the exact nature of the flow chemistry, the displacement effect (which will be assumed to be given by τ_e) due to the blunt nose must be governed solely by the initial conditions at the nose and the afterbody thickness parameter τ . Thus one can write

$$\tau_e = f(\tau, \rho_\infty, u_\infty) . \quad (\text{VI. 8})$$

Moreover, under the assumptions of hypersonic small disturbance theory Eq. VI. 8 can be written as

$$\tau_e = \tau f(\rho_\infty, u_\infty) . \quad (\text{VI. 9})$$

The flow field due to the effective body shape governed by the parameter γ_e can be expressed in terms of the free-stream conditions using the ideal-gas relations alone, since by assumption real-gas effects are negligible outside the entropy layer in the present analysis. In particular, the pressure distribution can be expressed in the form²⁵

$$\frac{p}{p_\infty} = f\left(\frac{x}{L}, \frac{y}{\gamma_e L}; M_\infty \gamma_e, M_\infty^{\frac{3+\gamma}{1+\gamma}} k^{\frac{1}{1+\gamma}} \frac{d}{L}\right). \quad (\text{VI. 10})$$

Eqs. VI. 9 and VI. 10 can be combined to yield

$$\frac{p}{p_\infty} = f\left(\frac{x}{L}, \frac{y}{\gamma L}; M_\infty \gamma, \rho_\infty, u_\infty, M_\infty^{\frac{3+\gamma}{1+\gamma}} k^{\frac{1}{1+\gamma}} \frac{d}{L}\right). \quad (\text{VI. 11})$$

A practically more useful form of Eq. VI. 11 is given by

$$\frac{p}{\rho_\infty u_\infty^2 \gamma^2} = f\left(\frac{x}{L}, \frac{y}{\gamma L}; \frac{\gamma}{T_\infty^{1/2}}, \rho_\infty, u_\infty, M_\infty^{\frac{3+\gamma}{1+\gamma}} k^{\frac{1}{1+\gamma}} \frac{d}{L}\right). \quad (\text{VI. 12})$$

Similar relations can be written down for the shock shape as well as the other flow quantities.

Eq. VI. 12 can have significant applications in wind-tunnel testing, since it affords a means of taking into account mismatches in free-stream temperature in the flows over blunt-nosed slender bodies. It was shown in Ref. 1 that for certain flight conditions the free-stream temperature in a wind tunnel could be as high as a factor of five larger than the corresponding flight value, when the density-altitude and velocity are duplicated in the tunnel. For such cases, Eq. VI. 12 provides a means of obtaining proper similitude between the flight and tunnel flows by choosing the thickness ratio of the afterbody appropriately. As mentioned earlier, the range of free-stream conditions over which the assumption that real-gas effects are important only in the entropy layer (and hence the range of validity of Eq. VI. 12), is significant and certainly nontrivial.

The similitude expressed by Eq. VI. 12 can also be derived in a more

rigorous manner from the basic differential equations governing the flow. For the sake of completeness we will indicate this derivation below.

Under the small-disturbance approximations that

$$\left. \begin{aligned} \frac{v}{u_{\infty}} &= O(\tau) \\ \frac{u}{u_{\infty}} &\equiv -1 + \frac{U}{u_{\infty}} \approx O(\tau^2) \end{aligned} \right\} \quad (\text{VI. 13})$$

and

(where u and v are the perturbation velocity components and U is the total axial velocity) the continuity, momentum and entropy equations can be written in the form

$$u_{\infty} \frac{\partial \rho}{\partial x} + v \frac{\partial \rho}{\partial y} = -\rho \left(\frac{\partial v}{\partial y} + v \frac{\partial v}{y} \right) \quad (\text{VI. 14})$$

$$u_{\infty} \frac{\partial u}{\partial x} + v \frac{\partial u}{\partial y} = -\frac{1}{\rho} \frac{\partial p}{\partial x} \quad (\text{VI. 15})$$

$$u_{\infty} \frac{\partial v}{\partial x} + v \frac{\partial v}{\partial y} = -\frac{1}{\rho} \frac{\partial p}{\partial y} \quad (\text{VI. 16})$$

$$\text{and} \quad u_{\infty} \frac{\partial S}{\partial x} + v \frac{\partial S}{\partial y} = 0 \quad (\text{VI. 17})$$

Note that the form of the first three of the above equations is the same whether or not any real-gas effects are present.

The boundary condition to be satisfied by the above equations at the body is simply that

$$v = u_{\infty} \frac{dY_b}{dx} \quad \text{on} \quad y = Y_b(x) \quad (\text{VI. 18})$$

Since in the present model real-gas effects are assumed to be negligible within the shock layer, the boundary conditions on the quantities v , p and ρ at the oblique shock wave $y = Y_s(x)$ can be written as

$$v = u_{\infty} \left(1 - \frac{\rho_{\infty}}{\rho}\right) \frac{dY_s}{dx} \quad (\text{VI. 19})$$

$$p = p_{\infty} + \rho_{\infty} u_{\infty}^2 \left(1 - \frac{\rho_{\infty}}{\rho}\right) \left(\frac{dY_s}{dx}\right)^2 \quad (\text{VI. 20})$$

$$\text{and} \quad \frac{\gamma}{\gamma-1} \frac{p}{\rho} = \frac{\gamma}{\gamma-1} \frac{p_{\infty}}{\rho} + u_{\infty}^2 \left(1 - \frac{\rho_{\infty}^2}{\rho^2}\right) \left(\frac{dY_s}{dx}\right)^2 \quad (\text{VI. 21})$$

Cheng²⁵ has shown that the downstream influence of the blunt nose can be accounted for within the framework of small-disturbance theory by using the equation

$$D_N = \lim_{x \rightarrow 0^+} \int_{Y_b}^{Y_s} \rho \left(e + \frac{v^2}{2}\right) (2\pi y)^y dy \quad (\text{VI. 22})$$

as the initial condition in the nose region, that is, as $x \rightarrow 0^+$. In the above equation, D_N represents the total inviscid drag of the nose.

The above equations are the same as those given by Cheng²⁵ except for the simplified form of the boundary condition equations at the shock wave in the present case (Eqs. VI. 19 to VI. 21). The system of equations given by Eqs. VI. 14 to VI. 17 and the appropriate boundary and initial conditions will constitute a closed system if the functional dependence of the entropy on the other state variables is prescribed.

Within the shock layer, the entropy can be expressed in terms of the local values of pressure and density using the perfect gas, isentropic relation

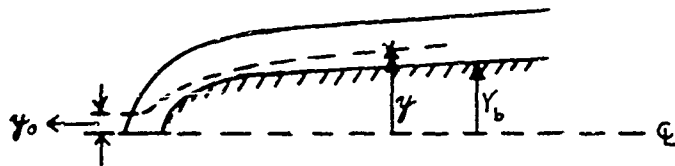
$$e^{\frac{s}{c_v}} = \text{const} \frac{p}{\rho^{\gamma}} \quad (\text{VI. 23})$$

where the value of the constant is unimportant since only changes in entropy from some reference state are of interest here. Thus within the shock layer, the entropy Eq. VI. 17 can be written as

$$\left(u_{\infty} \frac{\partial}{\partial x} + v \frac{\partial}{\partial y}\right) p \rho^{-\gamma} = 0. \quad (\text{VI. 24})$$

Note that Eq. VI. 24 is valid only for $Y_e < y < Y_s$.

For the range given by $Y_b < y < Y_e$, a more general form of the entropy equation is necessary. Now, the entropy at any point in the entropy layer is primarily dependent on the conditions in the nose region. In particular, because of the particle isentropic condition, the entropy at any point is equal to the value corresponding to that on the streamline passing through that point, and this latter quantity is given by its value immediately behind the shock wave. Thus the entropy at any point can be determined if the quantity ' y_0 ' corresponding to that point (see sketch below) can be expressed in terms of other



local variables and the free-stream conditions. The desired type of relation is provided by the mass conservation relation, which is

$$\rho_\infty u_\infty y_0 (\pi y_0)^y = \int_{Y_b}^y (\rho U) (2\pi y)^y dy \quad (\text{VI. 25})$$

where U is the total axial velocity component.

The entropy within the entropy layer can now be expressed in the form

$$S(x, y) = S[\rho(x, y); y_0, \rho_\infty, u_\infty] \quad (\text{VI. 26})$$

Eq. VI. 26 is, of course, a direct consequence of the Mach-number-independence principle.

For the purposes of studying the similitude expressed by the above equations, the transformation

$$x = L \tilde{x}, \quad y = L \gamma \tilde{y}, \quad u = u_\infty \gamma^2 \tilde{u}, \quad v = u_\infty \gamma \tilde{v}, \quad (\text{VI. 27})$$

$$p = p_\infty \tilde{p}, \quad \rho = \rho_\infty \tilde{\rho}$$

is made. Under this transformation Eqs. VI. 14 to VI. 16 become

$$\frac{\partial \tilde{\rho}}{\partial \tilde{x}} + \tilde{v} \frac{\partial \tilde{\rho}}{\partial \tilde{y}} = -\tilde{\rho} \left[\frac{\partial \tilde{v}}{\partial \tilde{y}} + \gamma \frac{\tilde{v}}{\tilde{y}} \right] \quad (\text{VI. 28})$$

$$\gamma(M_\infty T)^2 \left[\frac{\partial \tilde{u}}{\partial \tilde{x}} + \tilde{v} \frac{\partial \tilde{u}}{\partial \tilde{y}} \right] = -\frac{1}{\tilde{\rho}} \frac{\partial \tilde{p}}{\partial \tilde{x}} \quad (\text{VI. 29})$$

$$\gamma(M_\infty T)^2 \left[\frac{\partial \tilde{v}}{\partial \tilde{x}} + \tilde{v} \frac{\partial \tilde{v}}{\partial \tilde{y}} \right] = -\frac{1}{\tilde{\rho}} \frac{\partial \tilde{p}}{\partial \tilde{y}} \quad (\text{VI. 30})$$

The boundary conditions are

$$\tilde{v} = \frac{d\tilde{Y}_b}{d\tilde{x}} \quad \text{on} \quad \tilde{y} = \tilde{Y}_b(\tilde{x}) \quad (\text{VI. 31})$$

and

$$\tilde{v} = \left(1 - \frac{1}{\tilde{\rho}}\right) \frac{d\tilde{Y}_s}{d\tilde{x}} \quad (\text{VI. 32})$$

$$\tilde{p} = 1 + \left(1 - \frac{1}{\tilde{\rho}}\right) \left(\frac{d\tilde{Y}_s}{d\tilde{x}}\right)^2 \gamma(M_\infty T)^2 \quad (\text{VI. 33})$$

$$\frac{\tilde{p}}{\tilde{\rho}} = 1 + \left(1 - \frac{1}{\tilde{\rho}^2}\right) \left(\frac{d\tilde{Y}_s}{d\tilde{x}}\right)^2 (\gamma-1) (M_\infty T)^2 \quad (\text{VI. 34})$$

on $\tilde{y} = \tilde{Y}_s(\tilde{x})$.

The initial condition at the nose given by Eq. VI. 22 becomes

$$\frac{D_N}{e_\infty \rho_\infty (L r)^{1+\gamma}} = \lim_{\tilde{x} \rightarrow 0} \int_{\tilde{Y}_b}^{\tilde{Y}_s} \left(\tilde{\rho} \tilde{e} + (M_\infty r)^2 \frac{r(r-1)}{2} \tilde{\rho} \tilde{v} \right) (2\pi \tilde{y})^\gamma d\tilde{y} \quad (\text{VI. 35})$$

where the specific internal energy 'e' has been nondimensionalized with respect to the free-stream value, given by $e_\infty = \frac{1}{(\gamma-1)} \frac{p_\infty}{\rho_\infty}$.

For the shock layer (that is, for $\tilde{Y}_e < \tilde{y} < \tilde{Y}_s$) the entropy equation becomes

$$\left(\frac{\partial}{\partial \tilde{x}} + \tilde{v} \frac{\partial}{\partial \tilde{y}} \right) \tilde{p} \tilde{\rho}^{-\gamma} = 0 \quad (\text{VI. 36})$$

For the entropy layer (that is, $Y_b < y < Y_e$) the entropy equation is of the form

$$\tilde{S} = \tilde{S}(\tilde{p}; \tilde{y}_e, \rho_\infty, u_\infty) \quad (\text{VI } 37)$$

where

$$\tilde{y}_e (\pi \tilde{y}_e)^3 = \int_{\tilde{y}_b}^{\tilde{y}} (\tilde{\rho} \tilde{U}) (2 \pi \tilde{y})^3 d\tilde{y}. \quad (\text{VI } 38)$$

In Eq. VI 38, the total axial velocity has been nondimensionalized by the free-stream velocity u_∞ , so that $\tilde{U} = \frac{U}{u_\infty}$. (Note that under the small-disturbance assumptions $U \approx u_\infty$ and $\tilde{U} \approx 1$).

In principle, Eqs. VI 28 to VI 38 are sufficient to solve for the entire flow field. The parameters appearing in these equations are

$$\gamma, M_\infty \tau, \frac{D_N}{\rho_\infty e_\infty (L \tau)^{(3+\gamma)}}, \rho_\infty \text{ and } u_\infty. \quad (\text{VI } 39)$$

After some manipulation these parameters can be reduced to

$$\gamma, \frac{\tau}{L^\gamma}, \bar{T}_\infty^{-\frac{(3+\gamma)}{2(1+\gamma)}}, k^{\frac{1}{1+\gamma}} \frac{d}{L}, \rho_\infty \text{ and } u_\infty \quad (\text{VI } 40)$$

where the nose drag coefficient ' k ' is defined as

$$k = D_N / \left(\frac{1}{2} \rho_\infty u_\infty^2 \frac{d}{2} \left(\pi \frac{d}{2} \right)^2 \right). \quad (\text{VI } 41)$$

Since the present analysis is confined to bodies with geometrically similar nose shapes, the nose drag coefficient, k , need not be included in the similitude criteria.

The similitude relation for the pressure distribution can be written in the form

$$\frac{p}{\rho_\infty u_\infty^2 \tau^2} = f \left(\frac{x}{L}, \frac{y}{\tau L}; \tau \bar{T}_\infty^{-1/2}, \frac{d}{L} \bar{T}_\infty^{-\frac{(3+\gamma)}{2(1+\gamma)}}, \rho_\infty, u_\infty \tau \right) \quad (\text{VI } 42)$$

with similar relations being applicable for the other flow variables.

The similitude derived above for a general blunted slender body can be specialized for blunted wedges and cones. For these geometries, the equation of the surface may be written as

$$Y_b \approx \theta_c x \quad (\text{VI. 43})$$

where θ_c is the half-angle of the wedge or cone under consideration and plays the role of γ in the more general case. Since for the wedge or cone case a characteristic body length, L , does not exist, we can eliminate this quantity from the similitude by choosing it to be equal to $d T_\infty^{-(3+\gamma)/2(1+\gamma)}$. Then Eq. VI. 42 becomes

$$\frac{P}{\rho_\infty u_\infty^2 \theta_c^2} = f \left(\frac{x}{d} T_\infty^{-\frac{3+\gamma}{2(1+\gamma)}}, \frac{y}{d} T_\infty^{-\frac{1}{1+\gamma}}, \theta_c T_\infty^{-\frac{1}{2}}, \rho_\infty, u_\infty \right). \quad (\text{VI. 44})$$

Similarly, the shock shape can be expressed in the form

$$\frac{Y_s}{d} T_\infty^{-\frac{1}{1+\gamma}} = f \left(\frac{x}{d} T_\infty^{-\frac{3+\gamma}{2(1+\gamma)}}, \theta_c T_\infty^{-\frac{1}{2}}, \rho_\infty, u_\infty \right). \quad (\text{VI. 45})$$

Note that in Eqs. VI. 42, VI. 44 and VI. 45, the various combinations of the parameters of the problem that have been used are not nondimensional. These equations have been written in the form given mainly to illustrate in a clear manner the effects of a mismatch in free-stream temperature. As mentioned earlier, the effects of mismatches in free-stream temperature are of primary concern in hypervelocity testing. However, if desired, the above equations can be easily rewritten in a more conventional, dimensionally consistent form by making use of the fact that products and ratios of similitude parameters are also similitude parameters. Thus, Eq. VI. 44 can also be written as

$$\frac{P}{\rho_\infty u_\infty^2 \theta_c^2} = f \left(\frac{x}{d} M_\infty^{-\frac{3+\gamma}{1+\gamma}}, \frac{y}{d} M_\infty^{-\frac{2}{1+\gamma}}, M_\infty \theta_c, \rho_\infty, u_\infty \right). \quad (\text{VI. 46})$$

In order to verify the similitude given above, some numerical solutions have been carried out using the computer program developed by Curtis and Strom⁴⁰. The calculations were performed for a spherically blunted cone immersed in an equilibrium hypersonic flow of 25,000 ft/sec velocity and a free-stream density corresponding to 250,000 ft altitude. Two cases were considered. In the first case, the free-stream temperature chosen was that corresponding to the atmospheric value at an altitude of 250,000 ft, and the cone half-angle for this case was 9° . In the second case, the free-stream temperature was chosen to be a factor of four higher than the value corresponding to an altitude of 250,000 ft (as mentioned earlier, for the flight conditions that are being considered here mismatches in the free-stream temperature of this order are likely to occur in most hypersonic test facilities). The similitude derived above indicates that for proper similitude between the two cases, the cone half-angle for the second case has to be chosen as 18° .

The calculated results are shown in Figs. 25 and 26 correlated in terms of the similitude derived above.* Figure 25 illustrates the shock shape, while Fig. 26 illustrates the calculated surface pressure distribution. It can be seen that in spite of the fairly large mismatches in the free-stream temperature the correlations obtained are fairly good.

E. ANALYSIS OF BLUNT-NOSED SLENDER BODY

In the present section we will analyze the hypersonic flow past a blunt-nosed slender body using the approximate physical-chemical model developed in Section C. The essential features of this model are that the hypersonic small-disturbance approximations are made throughout the flow field except in a region close to the blunt nose, and that the flow field is divided roughly into two regions (a high entropy region close to the body where real-gas effects

* The authors express their thanks to Dr. J. Curtis of the Aerodynamic Research Department for performing these calculations.

are included and a relatively low entropy region close to the shock wave where the gas behavior is assumed to be ideal).

1. The Basic Equations. The method of analysis used in the present section (which closely follows the methods of Cheng³¹ and Chernyi^{74, 75}) is essentially integral in nature; that is, the partial differential equations governing the problem are reduced to a single ordinary differential equation by making various assumptions regarding the transverse distributions of various quantities within the disturbed region of the flow. Here, we shall start with a consideration of the energy conservation integral for the transverse flow field including the contributions due to the blunt leading edge. The energy integral for the present problem may be written as⁵⁴

$$u_{\infty} \frac{D_N}{2} + u_{\infty} \int_0^x \frac{dY_b}{dx} (\pi Y_b)^2 dx = \int_{Y_b}^{Y_s} \left\{ \rho U e + \rho (U - u_{\infty}) \frac{p}{\rho} + \frac{1}{2} [(U - u_{\infty})^2 + v^2] \rho U \right\} (\pi y)^2 dy - \rho_{\infty} Y_s \frac{(\pi Y_s)^2}{1+\gamma} \rho_{\infty} u_{\infty} \quad (\text{VI. 47})$$

where e is the specific internal energy of the gas. Eq. VI. 47 expresses the conservation of energy for an observer who is fixed in the undisturbed fluid.

In Eq. VI. 47 the specific internal energy e is given by

$$e = \frac{1}{\gamma-1} \frac{p}{\rho} \quad (\text{VI. 48})$$

for $Y_e < y < Y_s$, and

$$e = -\frac{1}{\gamma_f-1} \frac{p}{\rho} + h_D \quad (\text{VI. 49})$$

for $Y_b < y < Y_e$, where h_D is the energy contained in the dissociation mode (within the entropy layer) and γ_f is the frozen-flow specific heat ratio corresponding to the local value of the dissociation fraction.

If in Eq. VI. 47 the small-disturbance approximation $U \approx u_{\infty}$ is made, one obtains

$$\frac{D_N}{2} + \int_0^x p_b \frac{dY_b}{dx} (\pi Y_b)^{\gamma} dx = \int_{Y_b}^{Y_s} \rho \left(e + \frac{1}{2} w^2 \right) (\pi y)^{\gamma} dy - \frac{p_{\infty}}{\gamma-1} Y_s \frac{(\pi Y_s)^{\gamma}}{1+\gamma} \quad (\text{VI. 50})$$

The second term on the left-hand side of Eq. VI. 50 represents the contribution of the afterbody drag to the overall momentum balance. In the large Mach number regime, the second term in the right-hand side of Eq. VI. 50 may be neglected. Then Eq. VI. 50 can be written in the form

$$\frac{D_N}{2\pi^{\gamma}} + \int_0^x p_b \frac{dY_b}{dx} Y_b^{\gamma} dx = \int_{Y_b}^{Y_s} \rho \left(e + \frac{1}{2} w^2 \right) y^{\gamma} dy \quad (\text{VI. 51})$$

This relatively simple expression will form the basis for much of the following analysis.

Before we proceed, a point of clarification is in order here. As mentioned earlier, the analyses of Cheng³¹ and Chernyi^{74, 75} have considerable similarities, and both analyses use an equation of the form given by Eq. VI. 51. However, in his analysis, Cheng³¹ neglected the afterbody and kinetic energy integrals since these are of higher order (in the parameter $\frac{\gamma-1}{\gamma+1} + \frac{1}{M^2 \theta^2}$) than the remaining terms. On the other hand, Chernyi included these terms in his analysis. The pressure distributions calculated by Cheng³¹ for blunted wedges and cones show an oscillatory behavior far downstream of the nose, whereas the ones calculated by Chernyi^{74, 75} do not. Cheng³¹ notes that while this oscillatory behavior is not unbelievable, it is of doubtful physical reality. Hayes and Probstein⁵⁴ point out that the oscillatory behavior in Cheng's results may be caused by the neglect of the kinetic-energy terms.

In the present analysis, following Cheng, we will neglect the afterbody and kinetic-energy integrals since this is consistent with small disturbance approximations and with the other assumptions involved in the present model. However, later we will briefly indicate the application of Chernyi's method to the present problem.

When the afterbody and kinetic-energy integrals are neglected in Eq. VI. 51,

and when the resulting expression is combined with Eqs. VI. 48 and VI. 49, one obtains

$$\frac{D_N}{2\pi^y} - \int_{Y_b}^{Y_e} \rho h_D y^y dy = \int_{Y_b}^{Y_e} \frac{p}{\tau_f - 1} y^y dy + \int_{Y_e}^{Y_s} \frac{p}{\tau - 1} y^y dy . \quad (\text{VI. 52})$$

Since the pressure in the entropy layer is of the same order of magnitude as that in the shock layer and since the lateral extent of the shock layer is small compared to that of the entropy layer (that is, $Y_s - Y_e \ll Y_e - Y_b$), the second term in the right-hand side of Eq. VI. 52 can be neglected compared to the first. Moreover, as shown earlier, the pressure inside the entropy layer is equal (at each axial location) to that at its outer edge. Therefore Eq. VI. 52 reduces to

$$\frac{D_N}{2\pi^y} - \int_{Y_b}^{Y_e} \rho h_D y^y dy = p_e \int_{Y_b}^{Y_e} \frac{y^y}{\tau_f - 1} dy . \quad (\text{VI. 53})$$

The second term in the left-hand side of Eq. VI. 53 merely represents the total energy that is frozen out of the flow within the entropy layer, and by the assumptions of the present model (that is, 'freezing' of the flow along a line passing through the sonic point) this quantity must be independent of the distance downstream of the nose. Thus, as noted by Whalen⁵¹, one of the principle influences of real-gas effects on blunt-nosed slender-body flows is to cause an effective reduction in the nose bluntness and hence also its downstream influence. The net energy introduced into the transverse flow field by the nose bluntness is determined by the effective drag D_N' , defined by

$$\frac{D_N'}{2\pi^y} = \frac{D_N}{2\pi^y} - \lim_{x \rightarrow 0^+} \int_{Y_b}^{Y_s} \rho h_D y^y dy . \quad (\text{VI. 54})$$

Note that this quantity is always positive since the right-hand side of Eq. VI. 53 is always positive.

A net drag coefficient k' can be defined by the relation

$$k' = D_N' / \left(\frac{1}{2} \rho_\infty u_\infty^2 d \left(\pi \frac{d}{4} \right)^y \right) . \quad (\text{VI. 55})$$

However, note that unlike in the equivalent ideal-gas case, \mathcal{L}' is not independent of the free-stream state and velocity since the amount of energy that is frozen out at the nose as chemical energy is a function of the free-stream conditions.

The pressure, p_e , at the outer edge of the entropy layer can be related to the free-stream conditions and the shape of the outer edge of the entropy layer through the Newtonian-plus-centrifugal pressure formula

$$p_e(x) = \rho_\infty u_\infty^2 \left(\gamma_e'^2 + \frac{\gamma_e \gamma_e''}{1+\gamma} \right) \quad (\text{VI. 56})$$

where the primes denote differentiation with respect to the axial coordinate, x .

Finally, Eqs. VI. 54-56 can be combined with Eq. VI. 53 to give

$$\left(\gamma_e'^2 + \frac{\gamma_e \gamma_e''}{1+\gamma} \right) \int_{\gamma_b}^{\gamma_e} \frac{2\gamma'}{\gamma_f - 1} d\gamma = \mathcal{L}' \left(\frac{d}{2} \right)^{1+\gamma} \frac{1}{2^\gamma} \quad (\text{VI. 57})$$

Eq. VI. 57 is the fundamental equation which determines the rate of growth of the entropy layer and thus, also, the displacement effect of the blunt nose on the afterbody flow field including the effects of flow nonequilibrium.

As mentioned earlier (and as can be seen from Eq. VI. 57), one of the principle effects of flow nonequilibrium on the afterbody flow field appears through a net reduction in the energy release at the nose to the transverse flow field. Moreover, the effective drag coefficient \mathcal{L}' (unlike the equivalent ideal-gas drag coefficient \mathcal{L}) is a function of the free-stream conditions, and in general it decreases with increasing free-stream velocity. That is, at high velocities the amount of energy that is frozen out as chemical energy by the rapid expansion of the flow in the shoulder region is a significant fraction of the energy that is introduced into the transverse flow field by the blunting. Thus when real-gas effects are included, the downstream influence of a blunt nose can be significantly smaller than that calculated using ideal-gas theories.

Another important consequence of real-gas effects on the downstream influence of a blunt nose appears in Eq. VI. 57 through the integral on the left-hand side. It can be seen from this integral that the local rate of growth of the entropy layer is influenced by the distribution of the frozen-flow specific heat ratio, γ_f , within the entropy layer. The local value of the frozen-flow specific heat ratio (which is related to the local value of the dissociation fraction, α) is, of course, a function of the details of the flow field in the nose region. Thus when real-gas effects are present the rate of evolution of the entropy layer and the afterbody pressure distribution cannot be determined independently of the details of the nose shape.

In ideal-gas theories of blunted slender body flows, it is assumed that the effects of the blunt nose on the afterbody flow field can be represented by an appropriate concentrated force applied at the nose; the details of the nose shape are assumed to be of little importance. Even though this so-called 'blast-wave analogy' leads to erroneous results for the density and entropy distributions near the afterbody; it is known that the afterbody pressure field and the shock wave shape are predicted correctly. However, it can be seen from Eq. VI. 57 that when real-gas effects are present even the afterbody pressure field and shock shape cannot be solved for independently of the details of the flow in the nose region. This point has been mentioned earlier by Cheng³¹.

Eq. VI. 57 is also consistent with the similitude derived in the previous section according to which similitude between two blunted slender body flow fields can be obtained only if the flows in the nose region of the two cases are also similar. Thus even if it were possible for two slender bodies with different nose shapes to have the same values of the effective drag coefficient, C_D' , over at least a small range of free-stream conditions, it is highly unlikely that the two bodies will also have similar distributions of the frozen-flow specific heat ratios within their entropy layers. Therefore, 'blast-wave analogy' in the usual sense (that is, in the sense that the downstream influence of a blunt nose can be considered to be independent of the detailed nose shape) is not applicable to the present case.

2. Evaluation of the Integral in Eq. VI. 57. Before quantitative answers can be obtained from Eq. VI. 57, the integral appearing in its left-hand side has to be evaluated explicitly. However, as mentioned above, this task cannot be accomplished without knowing the details of the flow in the nose region. On the other hand, consistent with the integral nature of the analysis one can assume various profile shapes for the distribution of the effective frozen-flow specific heat ratio within the entropy layer. Any arbitrary constants used in the profile-shape equations can be evaluated by using the appropriate boundary conditions and (or) various integral conservation equations.

The simplest assumption one can make to evaluate the integral in Eq. VI. 57 is to assume that the entropy layer can be characterized by an average frozen-flow specific heat ratio, $\bar{\gamma}_f$. Then, the integral can be evaluated immediately, and Eq. VI. 57 reduces to

$$\left(Y_e^{1+\nu} - Y_b^{1+\nu} \right) \left(Y_e'^2 + \frac{Y_e Y_e''}{1+\nu} \right) = \bar{\epsilon} \mathcal{K}' \left(\frac{d}{2} \right)^{1+\nu} \quad (\text{VI. 58})$$

$$\text{where} \quad \bar{\epsilon} = \frac{\bar{\gamma}_f - 1}{2} \approx \frac{\bar{\gamma}_f - 1}{\bar{\gamma}_f + 1} \quad (\text{VI. 59})$$

Equation VI. 58 is identical to the equation given by Cheng³¹ for the ideal-gas case except that in the present case both $\bar{\epsilon}$ and \mathcal{K}' are functions of the free-stream conditions. Moreover, note that in the present case $\bar{\epsilon}$ may be a function of \mathcal{K} . In the present approximation each axial station in the entropy layer is assumed to be characterized by an average frozen-flow specific heat ratio; however, this average specific heat ratio may vary from station to station.*

Since the value of the frozen flow specific heat ratio depends only on the local value of the dissociation fraction, α , the value of the average specific heat ratio at any station can be determined by matching for the two cases the value of the total energy contained in the dissociation mode at that

* The shock layer is, of course, assumed to be characterized by a constant (ideal gas) value of the specific heat ratio.

station. That is, the value of the average specific heat ratio $\bar{\gamma}_f$ is assumed to be such that the dissociation energy it represents is equal to that corresponding to the actual distributions of the flow quantities at the station under consideration. Thus, the condition determining $\bar{\gamma}_f$ is represented by

$$\int_{Y_b}^{Y_s} \rho \alpha (2\pi y)^3 dy = \bar{\alpha} \int_{Y_b}^{Y_s} \rho (2\pi y)^3 dy. \quad (\text{VI. 60})$$

The left-hand side of Eq. VI. 60 is, of course, independent of the axial position and is equal to the value at the nose.

Now, within the accuracy of the small disturbance approximation $U \approx u_\infty$, the integral conservation of mass is governed by the equation

$$\rho_\infty Y_s (\pi Y_s)^3 = \int_{Y_b}^{Y_s} \rho (2\pi y)^3 dy. \quad (\text{VI. 61})$$

Thus Eqs. VI. 60 and VI. 61 can be combined together to yield

$$\lim_{x \rightarrow 0^+} \int_{Y_b}^{Y_s} \rho \alpha (2\pi y)^3 dy = \rho_\infty Y_e (\pi Y_e)^3 \bar{\alpha}. \quad (\text{VI. 62})$$

To be consistent with our previous approximations, the approximation $Y_s \approx Y_e$ has been made in Eq. VI. 62. The average specific heat ratio, $\bar{\gamma}_f$, is related to the average dissociation fraction, $\bar{\alpha}$, through the relation

$$\bar{\gamma}_f = \frac{3\bar{\alpha} + 7}{\bar{\alpha} + 5}. \quad (\text{VI. 63})$$

Equations VI. 58, 59, 62 and 63 determine the shape of the entropy layer (for a given body shape, Y_b) in terms of the integral in the left-hand side of Eq. VI. 62. Note that the above integral also determines the value of the effective drag coefficient, k' (see Eq. VI. 54). Thus in principle, given sufficient details near the nose for the evaluation of the above integral, one can solve for the shock shape and the body-surface pressure distribution. The evaluation of this integral will be discussed later.

It is appropriate here to consider other possible approximations that can be used in conjunction with Eq. VI. 57. The simplest of these is to assume that the whole entropy layer can be characterized by a single average value (independent of x) of the specific heat ratio which is given by the arithmetic mean of the values at the inner and outer edges of the entropy layer. Thus,

$$\bar{\gamma}_f = \frac{\gamma_b + \gamma}{2} \quad (\text{VI. 64a})$$

or alternately,

$$\bar{\epsilon} = \frac{\epsilon_b + \epsilon}{2} \quad (\text{VI. 64b})$$

Of course, apart from its very attractive simplicity, the assumption embodied in Eqs. VI. 64a and b does not really have a sound rational basis.

Another possible assumption is to take the transverse distribution of the effective frozen-flow specific heat ratio within the entropy layer to be a linear function of the cross-sectional area of the flow field. Thus, one can write

$$\gamma_f = \gamma + (\gamma_b - \gamma) \frac{Y_e^{y''} - \gamma^{y''}}{Y_e^{y''} - Y_b^{y''}} \quad (\text{VI. 65})$$

The choice of the cross-sectional area of the flow field as the appropriate parameter is prompted by the fact that in all blunted slender-body flow analyses the lateral coordinate always enters in the form $y^{1/2}$ or its derivative (this quantity is of course proportional to the cross-sectional area of the flow field). The above property has been exploited by Ladyzhenskii⁹⁴ who derived an area rule for blunted, slender three-dimensional bodies which have the same axial distribution of body cross-sectional area.

Note that Eq. VI. 65 satisfies the appropriate boundary conditions at the inner and outer edges of the entropy layer. Equation VI. 65 can be regarded as being composed of the zeroth and first-order terms in the small parameter $(\frac{\gamma_b - \gamma}{\gamma})$ and, in principle, more terms can be included if desired. However, for air, the parameter $(\frac{\gamma_b - \gamma}{\gamma})$ has a possible maximum value of only about 0.19. Thus, the errors involved in the terms neglected in Eq. VI. 65 would presumably be no more than $0 (\frac{\gamma_b - \gamma}{\gamma})^2$, or of the order of four percent.

Therefore inclusion of additional terms in Eq. VI. 65 does not appear to be worthwhile.

When Eq. VI. 65 is introduced in Eq. VI. 57, one obtains

$$\left(\gamma_e^\nu - \gamma_b^\nu\right) \left(\gamma_e'^2 + \frac{\gamma_e \gamma_e''}{1+\nu}\right) = k' \left(\frac{d}{2}\right)^{1+\nu} \frac{\gamma_b - \gamma}{2} \left(\log_e \frac{\gamma_b - 1}{\gamma - 1}\right)^{-1}. \quad (\text{VI. 66})$$

Equation VI. 66 represents the 'pressure-area' relation governing the entropy layer of any arbitrary plane or axisymmetric blunted slender body.

Equation VI. 66 reduces to the corresponding ideal-gas relation given by Cheng³² in the limit $\gamma_b \rightarrow \gamma$ (or more appropriately $\gamma_b - \gamma \ll \gamma - 1$) since

$$\lim_{\gamma_b \rightarrow \gamma} \left[\frac{\gamma_b - \gamma}{2} \left(\log_e \frac{\gamma_b - 1}{\gamma - 1}\right)^{-1} \right] \sim \frac{\gamma_b - \gamma}{2} \left(\frac{\gamma_b - \gamma}{\gamma - 1}\right)^{-1} = \frac{\gamma - 1}{2} \approx \epsilon. \quad (\text{VI. 67})$$

Several approximate methods have been discussed above to simplify the basic equation (Eq. VI. 57) governing the entropy layer. All these methods were based on simplifying assumptions on the nature of the transverse distribution of the various flow quantities within the entropy layer. Of the three methods described, those represented by Eqs. VI. 62 and VI. 66 are likely to be more accurate than that represented by Eq. VI. 64 since the former are based on rational simplifications and satisfy appropriate boundary and conservation conditions. Other approximations are possible, of course, but we shall confine our attention to the three given above and discuss them in more detail for the specific case of a spherically-blunted slender cone. In particular, we will discuss Eq. VI. 66 in some detail since it clearly illustrates the various effects of real-gas phenomena.

Eq. VI. 66 can be rewritten in the more convenient form with $\nu = 1$

$$\left(\gamma_e^2 - \gamma_b^2\right) \left(\gamma_e'^2 + \frac{\gamma_e \gamma_e''}{2}\right) = \frac{\gamma - 1}{2} k \frac{d^2}{4} \left[\frac{k'}{k} \left(\frac{\gamma - 1}{\gamma_b - \gamma} \log_e \frac{\gamma_b - 1}{\gamma - 1}\right)^{-1} \right] \quad (\text{VI. 68})$$

The above equation is identical to the corresponding ideal-gas equation except for the terms occurring on the right-hand side within the parenthesis. Let

$$c^2 = \frac{k'}{k} \left(\frac{\gamma-1}{\gamma_b-1} \log_e \frac{\gamma_b-1}{\gamma-1} \right)^{-1} \quad (\text{VI. 69})$$

Obviously, c^2 represents a correction factor which accounts for the real-gas effects. It can be seen from Eq. VI. 68 that influence of real-gas effects on the flow field can be visualized as being that due to a change in the nose radius from d to an effective value of cd .

The value of the correction factor is governed by two different effects. The first effect, which is represented by the factor k'/k , arises because only part of the energy introduced into the transverse flow field by the blunt nose is felt by the afterbody flow field, the rest being frozen out of the flow as dissociation energy. Since the quantity k'/k is always less than unity, the influence of this effect is to cause an apparent reduction of the nose diameter as far as the afterbody flow field is concerned. The second effect, which is represented by the parenthesized term in Eq. VI. 69, arises from the fact that the effective frozen flow specific heat ratio within the entropy layer is higher than the corresponding ideal-gas value. This factor can be rewritten in the form

$$\frac{\tau}{\log_e(1+t)} \quad ; \quad t = \frac{\gamma_b-1}{\gamma-1} \quad (\text{VI. 70})$$

For air, the quantity t has a maximum possible value of 0.667. Therefore, the second factor in Eq. VI. 69 is always greater than unity, its maximum value for air being around 1.3.

Thus it appears that the effect of the increased specific heat ratio within the entropy layer is to cause an increase in the downstream influence of the blunt nose, the effect being manifested as an apparent increase in the nose diameter of up to 14%. Hence the two effects appearing in Eq. VI. 69 display opposing trends in their influence on the slender-body flow field. However, the first effect is usually the dominant one, and the influence of real-gas effects on slender-body flows is in general to reduce the downstream influence of the blunt nose.

3. Solution for a Spherically Blunted Cone. For a cone, the body surface is represented by the equation $Y_b = \theta_c x$ where θ_c is the cone half-angle. For this case, Eq. VI.68 can be transformed to the form

$$(\bar{z}^2 - \zeta^2) \left(\bar{z}'^2 + \frac{\bar{z} \bar{z}''}{2} \right) = 1 \quad (\text{VI. 71})$$

where
$$\bar{z} = 2 \theta_c \frac{Y_c}{cd} \left(\frac{2}{\gamma-1} \cdot \frac{1}{k} \right)^{1/2} \quad (\text{VI. 72})$$

$$\zeta = 2 \theta_c^2 \frac{z}{cd} \left(\frac{2}{\gamma-1} \cdot \frac{1}{k} \right)^{1/2} \quad (\text{VI. 73})$$

The solution of the ordinary differential Eq. VI. 71 has been given by Cheng³¹. It can be seen clearly from Eqs. VI. 71-73 that the influence of real-gas effects (contained in the parameter c) is to reduce the length scale for the downstream influence, this length scale being represented by

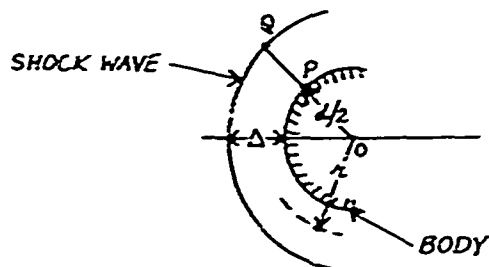
$$\bar{\kappa} = \frac{cd}{\theta_c^2} \left(\frac{\gamma-1}{2} \cdot k \right)^{1/2} \quad (\text{VI. 74})$$

In order to calculate the real-gas correction factor, c , the frozen-dissociation-energy integral mentioned earlier (see Eqs. VI.54 and VI.62) has to be evaluated. The value of this integral, of course, depends on the details of the flow field in the nose region. Now, if a numerical solution were available for the nose region (that is for the flow past a sphere) for the free-stream conditions of interest, then c can be computed from this and the solution can be continued over the afterbody with the help of Eq. VI.71. However, if a numerical solution is not available, then additional assumptions are necessary to evaluate c .

Firstly, in the nose region the shock wave will be assumed to be parallel to the body surface. Numerical calculations show that this assumption is fairly accurate for spherically shaped bodies. This assumption is sufficiently accurate for the present purpose since it is consistent with the Newtonian-flow assumption, $\epsilon \ll 1$, used in other simplifications. Secondly, numerical

calculations also show that the pressure distribution on a blunt body is influenced very little by real-gas effects. Therefore, the drag coefficient of the spherical nose will be taken to be equal to 0.92.

Let us consider the spherical nose shown below. Let the shock stand-off distance be denoted by the symbol Δ . Then since we have



assumed that the shock wave and the body surface are parallel to each other in the region of interest, the thickness of the shock layer will be equal to Δ everywhere in the region of the nose.

For a spherical nose, the dissociation-energy integral can be written in the convenient form

$$I_D \equiv \int_P^Q \rho h_D (2\pi r) dr = \int_{d/2}^{d/2 + \Delta} \rho h_D (2\pi r) dr \quad (\text{VI. 75})$$

where P is the sonic point and Q is the point on the shock wave radially opposite to P . By assuming that the quantity ρh_D has a suitably defined average over the shock layer between P and Q , Eq. VI. 75 can be reduced to

$$I_D = \pi \overline{\rho h_D} \Delta (d + \Delta) . \quad (\text{VI. 76})$$

Eqs. VI. 54 and VI. 76 can be combined together to yield

$$k' = k - \frac{\overline{\rho h_D}}{\frac{1}{2} \rho_\infty u_\infty^2} \frac{\Delta}{d/2} \left(2 + \frac{\Delta}{d/2} \right) . \quad (\text{VI. 77})$$

Now, for the conditions of present interest the dissociation fraction at Q is usually quite small; in other words, $h_{DQ}/u_\infty^2 \ll 1$ *. Within the accuracy of the present analysis we can neglect (h_{DQ}/u_∞^2) compared to unity and write Eq. VI. 77 as

$$h' = h - \frac{\rho_P h_{DP}}{\rho_\infty u_\infty^2} \frac{\Delta}{d/2} \left(2 + \frac{\Delta}{d/2}\right) \quad (\text{VI. 78})$$

where h_{DP} represents the dissociation energy in the body streamtube and is a constant downstream of the sonic point, P .

The method of calculating α_P (the dissociation fraction at the sonic point) has been described earlier. Essentially one assumes that the pressure in the nose region is insensitive to real-gas effects, so that the pressure at the sonic point may be written as $p_P = 0.528 p_{st}$. Since the entropy along the body streamline is also known, all other state variables at the sonic point can be obtained immediately from a Mollier diagram. However, the value of h_{DP} cannot be obtained in a simple manner from the value of α_P since air cannot be represented by a single, constant dissociation energy. That is, if one writes

$$h_D = \alpha D, \quad (\text{VI. 79})$$

then D is not a characteristic constant for air (as it is for a simple ideal dissociating gas, for example).

The value of h_D can be obtained from the energy equation along the body streamline. The energy equation can be written as

* One of the common definitions of the outer edge of the entropy layer is that it is the streamline for which $(d\gamma/dx) \sim 1$ at the shock. Also, for a sphere the sonic point lies between 40° and 50° from the axis. Therefore, it can be seen that this approximation is consistent with our earlier assumption that real-gas effects are negligible outside the entropy layer.

$$h_o = \frac{\gamma}{\gamma-1} \frac{P_o}{\rho_o} + \frac{1}{2} u_o^2 = \frac{\gamma_f}{\gamma_f-1} \frac{P}{\rho} + \frac{1}{2} u^2 + h_D \quad (\text{VL } 80)$$

where h_o is the total enthalpy of the flow. At the sonic point, $P_p = 0.528 P_{sr}$ and $u^2 = (\gamma_f P_p / \rho_p)$. Thus Eq. VL 80 can be written as

$$\frac{h_{Dp}}{u_o^2} = 2.5 M_o^{-2} \left[1 + 0.2 M_o^2 - 0.0752 \gamma_f \frac{\gamma_f+1}{\gamma_f-1} \frac{P_{st}/P_o}{\rho_p/\rho_o} \right] \quad (\text{VL } 81)$$

From this the value of the dissociation energy frozen in the body streamtube can be calculated for any given free-stream conditions.

The variations of h_{Dp}/u_o^2 and d_b/u_o^2 with the free-stream velocity are shown in Fig. 27 for an altitude of 250,000 ft.* It can be seen from this figure that a significant fraction of the free-stream kinetic energy remains frozen along the body stream tube. It can also be seen that the value of D varies significantly over the range of free-stream conditions of interest. The dip that is observed in both the curves around a free-stream velocity of 16,000 ft/sec is due to more or less complete dissociation of oxygen, while at this point nitrogen dissociation is still relatively unimportant.

It can be seen from Eq. VI. 76 that the value of the shock stand-off distance has also to be known in order to evaluate the frozen-dissociation-energy integral. In ideal-gas flows various approximate methods (such as the constant-density and thin-shock-layer approximations) exist for determining the shock stand-off distances on blunt bodies. However, simple formulae for the shock stand-off distance do not exist when real-gas effects are present. In the present analysis we will use the expression for the shock

* The subscript b has been used earlier to denote values on the afterbody. Note that since α_p and h_{Dp} are both constant downstream of the sonic point, the subscripts P and b can be used interchangeably for these variables.

stand-off distance given by the constant-density approximation (for the ideal-gas case), with the density ratio being interpreted as that corresponding to an equilibrium shock wave. The consistency between the constant density and Newtonian approximations has been pointed out by Hayes and Probstein⁵⁴. Thus, since the Newtonian approximation has been used in Section C as the basis for the ordering of the various quantities, it is consistent to use the constant density approximation to evaluate the shock stand-off distance in Eq. VI.78. Therefore, we will assume that

$$\frac{\Delta}{d/2} \approx \frac{\rho_\infty}{\rho_s} \left[1 - \left(\frac{8}{3} \frac{\rho_\infty}{\rho_s} \right)^{1/2} \right] \quad (\text{VI.82})$$

With the help of Eqs. VI.81 and 82, the quantity ℓ'/ℓ can now be calculated from Eq. VI.78. The variations of the quantities $c_1 (= \ell'/\ell)$, $c_2 (= \frac{\gamma-1}{\gamma_b-1} / \log_e \frac{\gamma_b-1}{\gamma-1})$ and $c (= \sqrt{c_1 c_2})$ with the free-stream velocity are shown in Fig. 28 for a spherical nose for an altitude of 250,000 ft. It can be seen that the opposing behaviors of c_1 and c_2 are such that the value of c remains close to unity over the range of free-stream velocities considered. Clearly the length scale for the downstream influence of the blunt nose (as defined by Eq. VI.74) is reduced by real-gas effects by less than ten percent over the range of free-stream conditions under consideration.

The pressure distribution and shock shape (as given by Eqs. VI.71 and 56) corresponding to the conditions $U_\infty = 25,000$ f.p.s., $h = 250,000$ ft and $\theta_c = 9^\circ$ are shown in Figs. 29 and 30. The value of c for these conditions was very close to unity, and the real-gas distributions are indistinguishable from the ideal-gas ones. For the sake of comparison the results obtained by the computer program of Ref. 40 are also shown on Figs. 29 and 30. Even in the numerical calculations the ideal and nonequilibrium flow solutions are found to be almost identical.

Before proceeding further let us consider the two other approximations that were suggested for simplifying Eq. VI.57. The only influence on the above results of using the approximation suggested in Eq. VI.64 in place of

the one given in Eq. VI.65 is to slightly modify the value of the parameter C_2 . It is found that the difference in the value of C_2 predicted by the two approximations is in general less than one percent. Thus even the crude approximation that is represented by Eq. VI.64 gives fairly accurate results.

The other approximation that was suggested is represented by Eqs. VI.59 and 62. Equation VI.62 can be simplified in a manner similar to that used in simplifying Eq. VI.75, with the result one can write

$$\bar{\alpha} \left[\frac{Y_e(x)}{d} \right]^2 = \frac{1}{2} \left(\frac{\rho_b}{\rho_\infty} \right) \frac{\Delta}{d/2} \left(2 + \frac{\Delta}{d/2} \right) \alpha_b \quad (\text{VI.83})$$

Again, the only effect of using the above approximation (instead of that given in Eq. VI.65) will be to modify the value of C_2 . However, in the present case C_2 will be a function of x , and Eqs. VI.83 and VI.71 have to be solved simultaneously. On the other hand, it does not appear that this procedure will drastically modify the qualitative conclusion (namely, that real-gas effects do not markedly influence the pressure distribution and shock shape) reached above. Therefore, the rather tedious procedure involved in carrying out the simultaneous solution of Eqs. VI.83 and VI.71 has not been attempted here.

As mentioned earlier, the procedure used above to account for real-gas effects can also be used in conjunction with Chernyi's method. In Chernyi's method no explicit account is taken of the entropy layer, the major assumption being that a major bulk of the gas that crosses the shock wave is contained in a thin layer next to the shock envelope. The energy and momentum-integral equations are written in the form

$$\frac{D'_N}{2} + \int_0^x p_b \frac{dY_b}{dx} (\pi Y_b)^y dx = \frac{1}{2} \rho_\infty u_\infty^2 \frac{(\pi Y_s)^y Y_s}{1+y} \left(\frac{dY_s}{dx} \right)^2 + p_b(x) \int_{Y_b}^{Y_s} \frac{(\pi y)^y}{y_f - 1} dy \quad (\text{VI.84})$$

$$\text{and} \quad \rho_\infty u_\infty^2 (\pi Y_s)^y Y_s \left(\frac{dY_s}{dx} \right) = \int_0^x p_b (2 \pi Y_s)^y dy. \quad (\text{VI.85})$$

Equations VI.84 and 85 determine the shock shape and the afterbody pressure distribution. The integral on the right-hand side of Eq. VI.84 can be determined using Eq. VI.65. Thus even within the framework of Chernyi's

analysis real-gas effects can be accounted for in a fairly simple manner. The details of the analysis are straightforward and will not be shown here.

Now, it should be pointed out that the accuracy of integral methods depends quite critically on the appropriate choice of the profiles chosen for representing the distribution of the flow quantities. The success of integral methods in boundary layer theory is, to a large measure, due to the appropriate choice of profiles. For example, the demonstrated success of the Lees-Reeves⁹⁵ method in treating separated flows is partly due to the use of the Cohen-Reshotko⁹⁶ similar family of profiles. Therefore, even in the present case an integral method based on the similar solution profiles for power law piston motions^{57, 69-71} would seem to hold promise.

The possibility of using similar solution profiles with integral methods has been suggested by Chernyi⁷⁸ and Mirels⁵² for the ideal-gas problem. However, these suggestions have not been exploited so far. A possible approach to the study of the combined effects of nonequilibrium and bluntness on the flows over slender bodies using integral methods based on similar solution profiles will be described below. Like in the integral methods of boundary layer theory, one can assume for the present case that at any given axial station the distributions of all the flow variables normal to the body are given by the similar solution profiles^{57, 69-71} corresponding to some unspecified values of the power-law index and the specific-heat ratio. The power-law index and specific-heat ratio characterizing the profiles are of course assumed to vary from one axial station to another, this variation itself being a part of the solution sought. This approach is equivalent to describing the flow at each axial station with an average value of the specific-heat ratio, with the average specific-heat ratio being different for different axial positions. The variation of the power-law index and the average specific-heat ratio with axial position can be determined from the various conservation equations and the shock relations.

Of course, like in all other integral methods the above approach would involve considerable numerical calculations. However, incorporation of some of the assumptions of thin shock layer theory into the above scheme might lead

to useful and tractable solutions. As mentioned earlier, the use of the similar solution profiles to describe the distribution of at least some of the flow quantities will lead to considerably better results than using any other simple profiles. An investigation of this area would be worthwhile.

F. VISCOUS EFFECTS

We will now consider the combined effects of nose bluntness, boundary layer displacement and flow nonequilibrium on slender-body flow fields. Viscous effects can be incorporated into the inviscid analyses given above by the model proposed by Cheng³¹. In this model a thin and distinct boundary layer is assumed to exist submerged within the entropy layer. In particular, the eventual 'swallowing' of the entropy layer by the boundary layer (which is known to occur at high altitudes) is not accounted for. An accounting of this phenomenon does not seem possible within the scope of integral methods. In addition to the assumptions made by Cheng³¹, in the present case it has been assumed that the chemical composition inside the boundary layer remains frozen.

We will first consider the similitude for blunt-nosed slender bodies when both viscous and real-gas effects are present. The viscous hypersonic similitude for slender bodies without nose bluntness has been given by Hayes and Probstein³⁰ and Luniev⁸⁷, while the similitude including the effects of nose bluntness has been given by Cheng³¹ and Luniev⁸⁸. The above similitudes show that for hypersonic viscous flows past slender bodies which have similar shapes and surface-temperature distributions of the form

$$\left. \begin{array}{l} \frac{Y_w}{\tau L} \\ \frac{T_w}{T_o} \end{array} \right\} = g\left(\frac{x}{L}\right) \quad (\text{VI. 86})^*$$

* In the present section, the subscript w denotes quantities at the wall, while the subscript b denotes the inner edge of the entropy layer.

The similitude parameters (in addition to those that are relevant to the corresponding inviscid-flow case) are the Prandtl number, Pr , and the quantity γRe_w , where

$$Re_w = \frac{\rho_w u_w L}{\mu_w} \quad (VI. 87)$$

The quantity Re_w has to be evaluated at some suitable reference point on the body.

The requirement of the equality of the parameter γRe_w for similarity between two flows is merely a statement of the condition that the distribution of the displacement thicknesses on the two (affinely related) bodies must follow the same affine law as their thickness distributions. Thus, the basic requirement for similarity can be stated as

$$\frac{\delta^*}{\gamma L} = f\left(\frac{x}{L}\right) \quad (VI. 88)$$

For a linear viscosity-temperature relation of the form

$$\frac{\mu_w}{\mu_\infty} = C \frac{T_w}{T_\infty} \quad (VI. 89)$$

the requirement expressed by Eq. VI. 88 reduces to the condition that the parameter

$$\bar{\gamma} = \frac{M_\infty^3 \sqrt{C}}{\gamma Re_\infty} \quad (VI. 90)$$

must be an invariant, while for a general viscosity law of the form $\mu \sim T^\omega$, the condition is that the quantity $M_\infty^{2+\omega} / \gamma Re_\infty$ must be invariant.

With the above remarks in mind we now turn our attention to the extension of the similitudes given in Section VI. D to include viscous effects. Now, if the flow in the nose region of a blunted slender body is required to be simulated, then similarity can be obtained by means of the Mach-number-independence principle. As pointed out earlier, the Mach-number-independence principle is applicable even when viscous effects are included; however, now

the appropriate length scale of the nose has to be duplicated in addition to the free-stream density and velocity. Thus, for the nose region one can write

$$\left. \begin{array}{l} \frac{p}{\rho_{\infty} u_{\infty}^2} \\ \frac{\rho}{\rho_{\infty}} \\ \frac{c_p T}{u_{\infty}^2} \\ \frac{\mu}{\rho_{\infty} u_{\infty} d} \\ \frac{U}{u_{\infty}} \end{array} \right\} = f\left(\frac{x}{d}, \frac{y}{d}; \rho_{\infty}, u_{\infty}, d\right). \quad (\text{VI. 91})$$

When the parameters on the right-hand side of Eq. VI. 91 are the same for two flows, then they are not merely similar but essentially identical.

Now, the solution of a hypersonic boundary layer is completely determined if the appropriate initial conditions, the wall conditions and the quantities p_b , $H_b (= h_{\infty})$, and U_b at the outer edge of the boundary layer are duplicated.* The appropriate initial conditions are, of course, given by Eq. VI. 91 while the requirements at the wall are the no-slip condition and the wall-temperature specification. Moreover, under the hypersonic small disturbance approximation, $U_b \approx u_{\infty}$ and $H_{\infty} \approx \frac{1}{2} u_{\infty}^2$. Thus in a manner completely analogous to Eq. VI. 8, the evolution of the boundary layer displacement thickness can be written in the form

$$\frac{\delta^*}{L} = f\left(\frac{x}{L}; \rho_{\infty}, u_{\infty}, d, \frac{T_w}{T_o}, \gamma, p_b\right) \quad (\text{VI. 92})$$

* For a blunt-nosed slender body the subscript b refers to the outer edge of the boundary layer which is the same as the inner edge of the entropy layer.

where T_o is the stagnation temperature of the flow.

Under the hypersonic small disturbance approximation, Eq. VI. 92 reduces to the form

$$\frac{\delta^*}{L} = \gamma f \left(\frac{\chi}{L} ; \rho_\infty, u_\infty, d, \frac{T_\infty}{T_o}, \frac{p_b}{\rho_\infty u_\infty^2 \gamma^2} \right) . \quad (\text{VI. 93})$$

In the above derivation, consistent with the classical boundary layer approach, we have assumed that the pressure distribution can be specified arbitrarily and that it is part of the conditions that are specified. However, in the present case there is an interaction between the boundary-layer growth and the pressure field, and it is precisely this interaction that we are seeking to simulate.

Clearly, the pressure distribution at the outer edge of the boundary layer of a blunt-nosed slender body will be determined by an equation of the form given by Eq. VI. 11, but with an effective body shape parameter $\left(\gamma + \frac{\delta_R^*}{L} \right)$ in place of γ . Here δ_R^* is the value of the displacement thickness at some conveniently chosen reference point (the mid-chord of a wing, for example). Thus, one can write

$$\frac{p_b}{p_\infty} = f \left\{ \frac{\chi}{L} ; M_\infty \gamma \left(1 + \frac{\delta_R^*}{\gamma L} \right), \rho_\infty, u_\infty, M_\infty^{\frac{3+\gamma}{1+\gamma}} k^{\frac{1}{1+\gamma}} \frac{d}{L} \right\} . \quad (\text{VI. 94})$$

For bodies with similar noses, the nose drag coefficient k can be dropped from the similitude and Eqs. VI. 93 and VI. 94 can be combined together to give

$$\frac{\delta^*}{\gamma L} = f \left\{ \frac{\chi}{L} ; M_\infty \gamma, M_\infty^{\frac{3+\gamma}{1+\gamma}} \frac{d}{L}, \frac{T_\infty}{T_o}, \rho_\infty, u_\infty, d \right\} . \quad (\text{VI. 95})$$

Thus, it can be seen from Eq. VI. 95 that for the hypersonic viscous flows past blunt-nosed slender bodies which obey Eq. VI. 86 the only additional (that is, not included in the corresponding inviscid case) requirement for similarity is the duplication of the nose length scale.

Finally, the similitude relations for the surface pressure, shock shape

and the heat-transfer rate can be written in the form

$$\left. \begin{array}{l} \frac{\dot{q}_w}{\rho_\infty u_\infty^2 \tau^2} \\ M_\infty Y_s / L \\ M_\infty^3 C_N \end{array} \right\} = f\left(\frac{x}{L}; M_\infty \tau, M_\infty^{\frac{1+\beta}{1-\beta}} \frac{d}{L}, \rho_\infty, u_\infty, d\right). \quad (\text{VI. 96})$$

In Eq. VI. 96 the boundary layer assumption $p_w \approx p_b$ has been made, and the parameters β , ω and Pr (which are usually included in general viscous similitudes) are not included since we are assuming here that only flows of the same gas are being studied; these parameters can be included if desired.

Unfortunately no solutions have been available to us for testing the accuracy and the range of validity of the above similitude. However, since the basic premise on which the similitude is based (namely, that real-gas effects are important only in that part of the flow field which is very near the body) has been verified for the inviscid case, one can expect that the viscous similitude will be valid over approximately the same range of conditions as the corresponding inviscid similitude.

Cheng has also developed a theory for the combined influence of boundary-layer displacement and leading edge effects on slender body flow fields. Cheng's development is based on the observation that the local flat-plate similarity approximation is consistent with thin-shock-layer concepts. Starting with the above observation, Cheng included boundary layer displacement effects into Eq. VI. 57 (for the plane flow case, $\eta = 0$) by replacing Y_t by Y_w where

$$Y_t = Y_w + \delta^* \quad (\text{VI. 97})$$

where the displacement thickness δ^* is related to the wall temperature and the free-stream conditions through the Newton-Busemann pressure formula given in Eq. VI. 56. Cheng's analysis is valid only for plane flows since

transverse curvature effects (which are often dominant in axisymmetric flows) are not included. Since we are mainly concerned with axisymmetric flows, we have not pursued the generalization of Cheng's viscous flow case to include real-gas effects.

G. SUMMARY AND DISCUSSION OF THE RESULTS

The combined effects of nose bluntness and chemical nonequilibrium phenomena on slender body flow fields was studied by using a simplified model for flow chemistry. The model was based on the observation that over a significant range of free-stream conditions real-gas effects are more important within the high entropy layer near the body than outside it. Thus in the model that was used, real-gas effects were neglected in the thin layer close to the shock wave (and outside the entropy layer), and the gas behavior in this region was assumed to be ideal with a constant specific heat ratio equal to that of the free stream.

It was also assumed that the flow in the nose region was effectively in equilibrium and that the flow freezes along a line passing through the sonic point on the body due to the rapid expansion in the region of nose-afterbody junctions. Under this approximation, the entropy layer is characterized by different values of entropy and effective (frozen) specific-heat ratio along each streamline.

Based on the above model, the effects of real-gas phenomena on blunted slender body flow fields was studied using a zeroth-order thin-shock-layer theory; that is, quantities of the order of $\frac{\gamma-1}{\gamma+1}$ and $(M\theta)^{-2}$ were assumed to be negligible. The analysis was essentially an extension of the theory developed by Cheng³¹ for the corresponding ideal-gas case. It was found that the effect of real-gas phenomena on the downstream influence of a blunt nose can be thought of as causing a net apparent reduction in the nose diameter.

The real-gas correction factor for the nose diameter was found to be influenced by two different effects, one due to the smaller amounts of momentum and energy that are imparted to the transverse flow field in the real-gas

case than in the corresponding ideal-gas case, and the other due to an increased value of the average specific heat ratio within the entropy layer. The first effect tends to reduce the downstream influence of the blunt nose while the second effect tends to increase the downstream influence. Therefore, the value of the correction factor remains close to unity over the range of free-stream conditions of interest, and the shock shape and the pressure distribution on the body were found to be influenced very little by the presence of real-gas effects.

To check the above conclusion, numerical computations were carried out for both ideal and real-gas flows over blunted slender cones by using the computer program developed by Curtis and Strom⁴⁰. The numerical results confirmed that, for the free-stream conditions under consideration, the effects of real-gas phenomena on the surface-pressure distributions and shock shapes on blunted slender bodies are indeed quite small.

The above conclusion is in contrast to the result obtained by Whalen⁵¹ who found that the pressure distributions on wedge-nosed flat plates were significantly influenced by real-gas effects. In fact, Whalen concluded that the blast-wave phenomena may be essentially eliminated when real-gas effects are present. A somewhat analogous conclusion was reached in Refs. 1 and 2 in connection with the study of the sensitivities of afterbody flow quantities on wedge-nosed flat plates to mismatches in free-stream conditions. In Refs. 1 and 2 it was found that the pressure immediately downstream of the nose-afterbody junction (of a wedge-nosed flat plate) was considerably smaller than the corresponding ideal-gas value, so that it would appear that in this case the downstream influence of the blunt nose would be significantly reduced by the presence of real-gas effects.

Therefore, we can conclude that the effect of real-gas phenomena on the downstream influence of a blunt nose will depend on the shape of the nose. This is not surprising since real-gas effects are essentially nonsimilar, and the flow downstream of the nose cannot be expected to be independent of the details of the flow in the nose region when real-gas effects are present. In general, it appears that when there is a smooth junction between the nose and the afterbody (such as in a spherically blunted cone), real-gas effects do not

significantly influence either the surface pressure distribution or the shock shape. On the other hand, when the junction between the nose and the afterbody is a sharp corner (such as in a wedge-nosed flat plate or a flat-plate slender body), it appears that real-gas effects will significantly reduce the downstream influence of the blunt nose, and in some cases altogether eliminate the blast-wave effect.

A restricted similitude applicable to real-gas flows past blunt-nosed slender bodies was also derived using the concept that over a significant range of free-stream conditions real-gas effects are important only within the entropy layer and not outside it. It was found that the requirement of the duplication of the free-stream temperature (which is part of the similitudes given by Cheng²⁵ and Inger²⁶) can be relaxed provided that the nose-shape and the free-stream velocity are duplicated. This similitude is especially useful when similitude is required not only in the region of the afterbody but also in the nose region. For the above case the requirements imposed by the similitudes given by Cheng²⁵ and Inger²⁶ would imply that there is essentially no similitude; that is all conditions have to be duplicated. The similitude is found to be valid for the viscous case also provided that the characteristic length scale of the nose is duplicated.

SECTION VII CONCLUSIONS

In the present study, we have examined the similitude requirements for hypervelocity, slender-body flows when nonequilibrium and nose-bluntness effects are present. For such flows, it has been shown by Cheng and Inger that proper similitude requires, among other things, complete duplication of the free-stream thermo-chemical state. However, in many cases, the reservoir conditions required to duplicate all the similitude parameters simultaneously in a wind tunnel are so severe as to make partial simulation the only recourse. Therefore the present study has been concerned primarily with the effects of mismatches in certain free-stream conditions on slender-body flow fields.

Two related studies have been carried out. In the first study, direct comparisons between the flight and wind-tunnel flow fields were made for a blunted slender cone by assuming a hypothetical wind-tunnel performance. The pressure distribution on the cone was assumed to be uninfluenced by real-gas effects, and the influence of real-gas effects on the other flow quantities was calculated by using a streamtube computer program. The second study consisted of an analytical investigation of real-gas effects on blunted slender body flows by using a thin-shock-layer approach. This study was based on a simplified model for the flow chemistry in which real-gas effects were included in the high entropy, low density layer near the body but was neglected in the high density, lower entropy layer near the shock wave.

In the first study it was found that, at the free-stream conditions under consideration, the flow in the vicinity of the blunt nose is Mach number independent even when real-gas effects are present. Thus the flow within the entropy layer (that is, the layer consisting of streamlines that have crossed the nearly normal portions of the shock wave) also remains Mach number independent. On the other hand, the flow in the outer portion of the shock layer (which consists of streamlines that have crossed the more oblique parts of the shock wave) is more sensitive to mismatches in free-stream temperature, and is analogous to the sharp-nosed slender body case. Thus the amount of

nose bluntness has an important bearing on the similitude characteristics since it determines the relative extents of the entropy layer and the outer regions of the shock layer. In the spherically blunted slender cone cases considered for $R_N = 1.5$ in., the flow along the cone is dominated by the blunt nose and, hence, is insensitive to mismatches in M_∞ . However, for $R_N = 0.2$ in., the flow over most of the conical afterbody will behave as a sharp-nosed body and mismatches in M_∞ can be important. In both cases the effects of nonequilibrium phenomena are as large or larger than the differences between the flight and wind-tunnel flow fields. Thus, it is important to match body scale as well as U_∞ so that L/U_∞ is duplicated.

In the second study, which was based on thin-shock-layer concepts, it was found that the effect of real-gas phenomena on the downstream influence of a blunt nose can be thought of as causing an apparent reduction in the diameter of the nose. However, it was found that the effect was fairly small for spherically blunted cones over the range of free-stream conditions that were considered. However, it appears that the effect of real-gas phenomena on blunted slender body flows will be a function of the details of the nose shape. Thus, it is likely that real-gas effects would be quite significant for bodies with flat noses, or where there is a sharp corner at the nose-afterbody junction.

A new similitude applicable to real-gas flows over blunted slender bodies was also derived. This similitude has the advantage that the duplication of the free-stream temperature (which is required by existing real-gas similitudes) has been relaxed. The extension of the similitude to include viscous effects is also given.

The present study serves to illustrate some of the problems associated with partial simulation of the hypervelocity flows. An analysis of the type reported here should be made for each hypervelocity wind tunnel in order to delineate the flight conditions that can be simulated in a given facility. In this regard it should be reiterated that the hypothetical wind-tunnel performance assumed here far exceeds that of existing facilities, having been selected in order to minimize nozzle-flow nonequilibrium effects.

REFERENCES

1. Wittliff, C.E., Sundaram, T.R., Rae, W.J. and Lordi, J.A., "Study of High-Density Hypervelocity Flows and Similitudes." AEDC-TR-67-72, April 1967.
2. Wittliff, C.E. and Sundaram, T.R., "A Study of Hypervelocity Slender-Body Flows and Similitudes Including the Effects of Nonequilibrium and Nose Bluntness." AIAA Paper No. 68-14, January 1968.
3. Leonard, R.L. and Rose, P.H., "Feasibility of a High-Performance Aerodynamic Impulse Facility." AIAA Journal 6, 3, pp. 448-457, March 1968.
4. Warren, W.R. and Marston, C.H., "A High Density, High Velocity Equilibrium Free-Stream Shock Tunnel Concept." AIAA Paper No. 68-17, January 1968.
5. Lordi, J.A. and Mates, R.E., "Nonequilibrium Expansions of High-Enthalpy Air Flows." ARL 64-206, November 1964. (Also AIAA Journal 3, 10, pp. 1972-1974, October 1965.)
6. Harris, C.J. and Warren, W.R., "Correlations of Nonequilibrium Chemical Properties of Expanding Air Flows." G. E. Rept. R64SD92, December 1964. (Also AIAA Journal 4, 6, pp. 1148, June 1966.)
7. Burke, A.F., Curtis, J.T. and Boyer, D.W., "Nonequilibrium Flow Considerations in Hypervelocity Wind Tunnel Testing." CAL Rept. AA-1632-Y-1, May 1962.
8. Inger, G.R., "Viscous and Inviscid Stagnation Flow in a Dissociating Hypervelocity Free Stream." Proc. HTFMI, Stanford Univ. Press, 1962.
9. Gibson, W.E., "The Effect of Ambient Dissociation on Equilibrium Shock-Layers." ARL 64-42, March 1964. (Also I.A.S. Paper No. 63-70, January 1963.)
10. Lewis, C.H. and Burgess, E.G., III, "Altitude-Velocity Table and Charts for Imperfect Air." AEDC-TDR-64-214, January 1965.
11. Hayes, W.D. and Probstein, R.F., Hypersonic Flow Theory, 1st Edition, Academic Press, New York, 1959.
12. Probstein, R.F., "Interacting Hypersonic Laminar Boundary-Layer Flow Over a Cone." Div. of Eng., Brown Univ., Tech Rept. No. AF 2798/1, March 1955.

13. Probst, R. F. and Elliot, D., "The Transverse Curvature Effect in Compressible Axially Symmetric Laminar Boundary-Layer Flow." J. Aero. Sci. 23, 3, pp. 208-224, 236, March 1956.
14. Yasuhara, M., "Axisymmetric Viscous Flow Past Very Slender Bodies of Revolution." J. Aero. Sci. 29, 6, pp. 667-679, 688, June 1962.
15. Stewartson, K., "Viscous Hypersonic Flow Past a Slender Cone." Physics of Fluids 7, 5, pp. 667-675, May 1964.
16. Solomon, J. M., "Axisymmetric Laminar Boundary Layers With Very Large Transverse Curvature." NOL TR 66-225, February 1967.
17. Grabow, R. M., "Turbulent Boundary Layer Displacement Effects in Hypersonic Flow." von Karman Inst. Fluid Dyn. TN-34, May 1967.
18. Mirels, H. and Ellinwood, J. W., "Hypersonic Viscous Interaction Theory for Slender Axisymmetric Bodies." AIAA Paper No. 68-1, January 1968.
19. Marchand, E. O., Lewis, C. H., and Davis, R. T., "Second-Order Boundary-Layer Effects on a Slender Blunt Cone at Hypersonic Conditions." AIAA Paper No. 68-54, January 1968.
20. Romig, M. F., "Conical Flow Parameters for Air in Dissociation Equilibrium: Final Results." Convair SRL Research Note 14, January 1958.
21. Harney, D. J., "Chemical Kinetic Regimes of Hypersonic Flight Simulation." AEDC-TDR-63-3, January 1963.
22. Gibson, W. E., "Dissociation Scaling for Nonequilibrium Blunt-Nose Flows." AEDC-TDR-62-25, February 1962.
23. Tsien, H. S., "Similarity Law of Hypersonic Flow." J. Math. & Phys. 25, pp. 247-251, 1946.
24. Hayes, W. D., "On Hypersonic Similitude." Quart. Appl. Math. 5, 1, pp. 105, 106, April 1947.
25. Cheng, H. K., "Similitude of Hypersonic Real-Gas Flows Over Slender Bodies with Blunted Noses." J. Aero. Sci. 26, 9, pp. 575-585, September 1959.
26. Inger, G. R., "Similitude of Hypersonic Flows Over Slender Bodies in Nonequilibrium Dissociated Gases." AIAA Journ. 1, 1, pp. 46-53, January 1963.
27. Oswatitsch, K., "Similarity Laws for Hypersonic Flow." Royal Inst. for Tech., Tech. Note No. 16, Stockholm, 1950.

28. Ehret, D. M. , Rossow, V. J. and Stevens, V. I. , "An Analysis of the Applicability of the Hypersonic Similarity Law to the Study of the Flow About Bodies of Revolution at Zero Angle of Attack." NACA TN 2250, December 1950.
29. Bertram, M. H. , "Correlation Graphs for Supersonic Flow Around Right Circular Cones at Zero Yaw in Air as a Perfect Gas." NASA TN D-2339, June 1964.
30. Hayes, W. D. , and Probstein, R. F. , "Viscous Hypersonic Similitude." J. Aero/Space Sci. 26, p. 815, 1959.
31. Cheng, H. K. , "Hypersonic Flow with Combined Leading-Edge Bluntness and Boundary-Layer Displacement Effect." CAL Rept. No. AF-1285-A-4, August 1960. (Also J. Aero. Sci. 28, 5, pp. 353-381, 410, May 1961.)
32. Chernyi, G. G. , Introduction to Hypersonic Flow, Academic Press, New York, 1961.
33. Ellett, D. M. , "Pressure Distributions on Sphere Cones." Sandia Corp. Rept. RR-64-1796, January 1965.
34. Roberts, J. F. , Lewis, C. H. and Reed, M. , "Ideal Gas Spherically Blunted Cone Flow Field Solutions at Hypersonic Conditions." AEDC-TR-66-121, August 1966.
35. Jenkins, B. Z. , "Real Gas Flow Field Properties Around Blunt Cone, Vol. II." U. S. Army Missile Command Rept. RF-TR-63-18, December 1963.
36. Wood, A. D. , Springfield, J. F. and Pallone, A. J. , "Chemical and Vibrational Relaxation of an Inviscid Hypersonic Flow." AIAA Journal 2, pp. 1697-1705, October 1964.
37. Edenfield, E. E. , "Comparison of Hot Shot Tunnel Force, Pressure, Heat-Transfer and Shock Shape Data with Shock Tunnel Data." AEDC-TDR-64-1, January 1964.
38. Lordi, J. A. , Mates, R. E. and Moselle, J. R. , "Computer Program for the Numerical Solution of Nonequilibrium Expansions of Reacting Gas Mixtures." CAL Rept. No. AD-1689-A-6, October 1965.
39. Lomax, H. and Inouye, M. , "Numerical Analysis of Flow Properties Around Blunt Bodies Moving at Supersonic Speeds in an Equilibrium Gas." NASA TR-R-204, July 1964.
40. Curtis, J. T. and Strom, C. R. , "Computations of the Nonequilibrium Flow of a Viscous, Radiating Fluid About a Blunt Axisymmetric Body." AFFDL-TR-67-40, June 1967.

41. Griffith, B. J. and Lewis, C. H., "A Study of Laminar Heat Transfer to Spherically Blunted Cones and Hemisphere-Cylinders at Hypersonic Conditions." AEDC-TDR-63-102, June 1963.
42. Kopal, Z., "Tables of Supersonic Flow Around a Cone." MIT Dept. Elect. Eng. Tech. Rept. No. 1, 1947.
43. Sims, J. L., "Supersonic Flow Around Right Circular Cone, Tables for Zero Angles of Attack." NASA SP-3004, 1964.
44. Bertram, M. H., "Correlation Graphs for Supersonic Flow Around Right Circular Cones at Zero Yaw in Air as a Perfect Gas." NASA TND-2339, June 1964.
45. Fenter, F. W. and Gibbons, H. B., "The Thermodynamic Properties of High Temperature Air." Chance Vought Research Center Rept. RE-IR-14, June 1961.
46. Zakkay, V. and Krause, E., "Boundary Conditions at the Outer Edge of the Boundary Layer on Blunted Conical Bodies." ARL 62-386, July 1962.
47. Cleary, J. W., "An Experimental and Theoretical Investigation of the Pressure Distribution and Flow Fields of Blunted Cones at Hypersonic Mach Numbers." NASA TND-2969.
48. Taub, P. A., "Hypersonic, Low-Density Sphere and Cone Drag Correlations." AIAA Journal, 6, p. 1577, Aug. 1968.
49. Lees, L. "Laminar Heat Transfer Over Blunt-Nosed Bodies at Hypersonic Flight Speeds." Jet Propulsion, 26, pp. 259-269, April 1956.
50. Inger, G. R., "Nonequilibrium Hypersonic Stagnation Flow with Arbitrary Surface Catalycity Including Low Reynolds Number Effects." Int. Journ. Heat and Mass Transfer, 9, pp. 755-772, 1966.
51. Whalen, R. J., "Viscous and Inviscid Nonequilibrium Gas Flows." J. Aero/Space Sci. 29, p. 1222, October 1962.
52. Mirels, H., "Hypersonic Flow Over Slender Bodies Associated with Power-Law Shocks." Advances in Appl. Mechanics, Vol. 7, p. 1, 1962.
53. Guiraud, J. P., Vallee, D., Zolver, R., "Bluntness Effects in Hypersonic Small-Disturbance Theory." Basic Developments in Fluid Dynamics, Vol. I (ed: M. Holt), p. 127, Academic Press, New York, 1965.

54. Hayes, W. D., and Probstein, R. F., Hypersonic Flow Theory, Vol. I Inviscid Flows, Academic Press, New York, 1967.
55. Cox, R. N., and Crabtree, L. F., Elements of Hypersonic Aerodynamics, Academic Press, New York, 1965.
56. Cheng, H. K., "Recent Advances in Hypersonic Flow Research." AIAA Journ. 1, 295, 1963.
57. Sedov, L. I., Similarity and Dimensional Methods in Mechanics, (Transl: M. Holt), Academic Press, New York, 1959.
58. Stanyukovich, K. P., Unsteady Motion of Continuous Media, (Transl: M. Holt), Academic Press, New York, 1960.
59. Probstein, R. F., "Recent Soviet Advances in Inviscid Hypersonic Aerodynamics." Aerospace Engineering, July 1961.
60. Lees, L., "Recent Developments in Hypersonic Flow." Jet Propulsion 27, p. 1162, 1957.
61. VanDyke, M. D., "A Study of Hypersonic Small-Disturbance Theory." NACA Rep. 1194, 1954.
62. Cole, J. D., "Newtonian Flow Theory for Slender Bodies." J. Aero. Sci. 24, p. 448, 1957.
63. Cheng, H. K., and Pallone, A. J., "Inviscid Leading-Edge Effect in Hypersonic Flow." J. Aero. Sci. 23, p. 700, 1956.
64. Lees, L., and Kubota, T., "Inviscid Hypersonic Flow over Blunt-Nosed Slender Bodies." J. Aero. Sci. 24, p. 195, 1957.
65. Lin, S. C., "Cylindrical Shock Waves Produced by Instantaneous Energy Release." J. Appl. Phys. 25, p. 54, 1954.
66. Taylor, G. I., "The Formation of a Blast Wave by a Very Intense Explosion." Proc. Roy. Soc. London, A201, p. 159, 1950.
67. Sedov, L. I., "Propagation of Strong Blast Waves." Prikl. Math. Mekh. 10, p. 241, 1946.
68. Sakurai, A., "On the Propagation and Structure of the Blast Wave." J. Phys. Soc. Japan 8, p. 662, 1953. Also 9, p. 256, 1954.
69. Grigorian, S. S., "Cauchy's Problem and the Problem of the Piston for One-Dimensional, Nonsteady Motions of a Gas (Automodel Motion)." PMM Jour. Appl. Math. and Mech. 22, p. 244, 1958.

70. Kochina, N. N. , and Mel'nikova, N. S. , "On the Steady Motions of Gas Driven Outwards by a Piston, Neglecting Counter Pressure. " PMM Jour. Appl. Math. and Mech. 22, p. 622, 1958.
71. Adamski, V. B. , and Popov, N. A. , "The Motion of a Gas under the Action of a Pressure on a Piston Varying According to a Power Law. " PMM Jour. Appl. Math. and Mech. 23, p. 3, 1959.
72. Mirels, H. , "Approximate Analytical Solutions for Hypersonic Flow Over Slender Power-Law Bodies. " NASA TRR-15, 1959.
73. Mirels, H. , and Thornton, P. R. , "Effect of Body Perturbations on Hypersonic Flow Over Slender Power-Law Bodies. " NASA TRR-45, 1959.
74. Chernyi, G. G. , "Effect of Slight Blunting of the Leading Edge of a Profile on Flow at High Supersonic Speeds. " Akad. Nauk SSSR Doklady 116, p. 197, 1956.
75. Chernyi, G. G. , "Flow Past a Thin Blunt-Nosed Cone at High Supersonic Speed. " Dokl. Akad. Nauk SSSR, 115, p. 681, 1957. English Transl: Royal Aircraft Establishment Transl. No.
76. Chernyi, G. G. , "Effect of Slight Blunting of Leading Edge of an Immersed Body on the Flow Around it at Hypersonic Speeds. " Izv. Akad. Nauk SSSR, otd. Tech. Nauk, 1958, No. 6, p. 54, NASA Tech. Transl. No. F-35, 1960.
77. Chernyi, G. G. , "Application of Integral Relationships in Problems of Propagation of Strong Shock Waves. " PMM J. Appl. Math. Mech. 24, p. 159, 1960.
78. Chernyi, G. G. , "Integral Methods for the Calculation of Gas Flows with Strong Shock Waves. " PMM J. Appl. Math. Mech. 25, p. 138, 1961.
79. Luniev, V. V. , Hypersonic Flows Around Thin Blunted Power-Law Shapes. " PMM J. Appl. Math. Mech. 26, p. 572, 1962.
80. Sychev, V. V. , "On the Theory of Hypersonic Gas Flows with a Power-Law Shock Wave. " PMM J. Appl. Math. Mech. 24, p. 756, 1960.
81. Sychev, V. V. , "On the Theory of Hypersonic Flow Over Blunt-Nosed Slender Bodies. " Advances in Aeronautical Sciences, Vol. 3, 1962.
82. Yakura, J. K. , "Theory of Entropy Layers and Nose Bluntness in Hypersonic Flow. " Hypersonic Flow Research (ed: F. R. Riddell) p. 421, Academic Press, New York, 1962.

83. Guirard, J. P., "Asymptotic Theory of Hypersonic Flow." Fundamental Phenomena in Hypersonic Flow (ed J. Gordon Hall), p. 70. Cornell Univ. Press, 1966.
84. Luniev, V. V., "Motion of a Slender Blunted Body in the Atmosphere with High Supersonic Speed." ARS Journal 30, p. 414, 1960.
85. Vaglio-Laurin, R., and Bloom, M. H., "Chemical Effects in External Hypersonic Flows." Hypersonic Flow Research (ed F. R. Riddell), Academic Press, New York, 1962. (Also AFOSR 1273 (PIBAL Rept. 640)), 1961.
86. Oguchi, H., "The Blunt-Leading-Edge Problem in Hypersonic Flow." AIAA Journal 1, p. 361, 1963.
87. Luniev, V. V., "On the Similarity of Hypersonic Viscous Flows Around Slender Bodies." PMM J. Appl. Math. Mech. 23, p. 273, 1959.
88. Luniev, V. V., "The Law of Similitude for Viscous Hypersonic Flow Around Blunted Slender Bodies." PMM J. Appl. Math. Mech. 25, p. 1050, 1961.
89. Van Hise, V., "Analytic Studies on Induced Pressures on Long Bodies of Revolution with Varying Nose Bluntness at Hypersonic Speeds." NASA Tech. Rept. No. R-78, 1961.
90. Feldman, S., "Numerical Comparison Between Exact and Approximate Theories of Hypersonic Inviscid Flow Past Slender Blunt Nosed Bodies." ARS Journ. 30, p. 463, 1960.
91. Whitliff, C. E. and Curtis, J. T., "Normal Shock Wave Parameters in Equilibrium Air." CAL Rept. No. CAL-111, November 1961.
92. Stoddard, F. J., Hertzberg, A. and Hall, J. G., "The Isentropic Compression Tube: A New Approach to Generating Hypervelocity Test Flows with Low Dissociation." Aerospace Research Labs Report No. 67-0133, 1967.
93. Daiber, J., Stoddard, F. J., Thompson, H. M., and Rehm, R. J., "Research on Advanced Gasdynamic Facilities." CAL Rept. No. AD-1716-A-9, 1966.
94. Ladyzhenskii, M. D., "Hypersonic Area Rule." Inzh. zh 1 159, 1961 (Transl. in AIAA J. 1, 2296, 1963).
95. Lees, L. and Reeves, B. L., "Supersonic Separated and Reattaching Flows: Part I." AIAA J., 1907, 1964.
96. Cohen, C. B., and Reshotko, E., "Similar Solutions for the Compressible Laminar Boundary Layer with Heat Transfer and Pressure Gradient." NASA Rept. 1273, 1956.

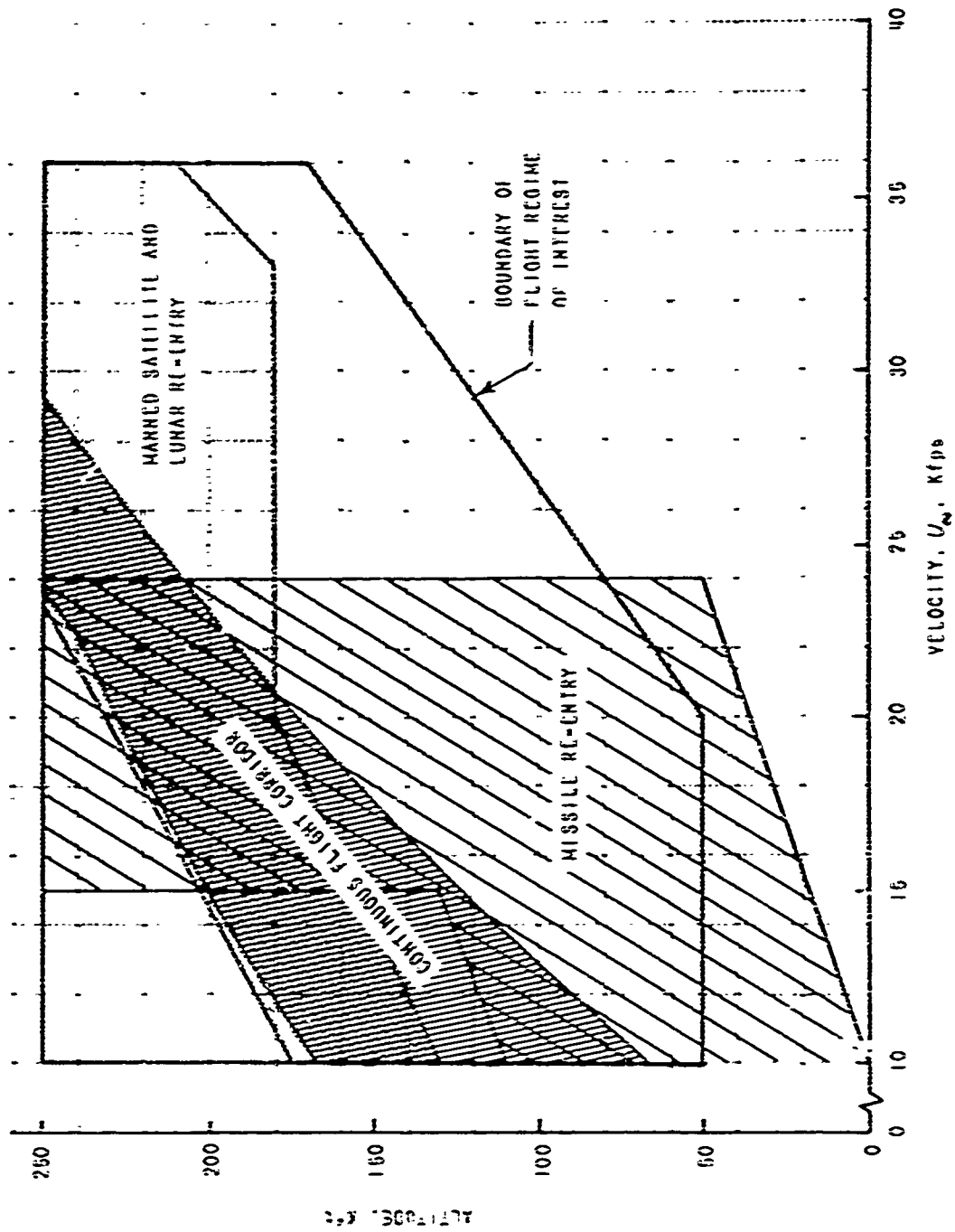


Fig. 1 Altitude-Velocity Map of Flight Regime of Interest

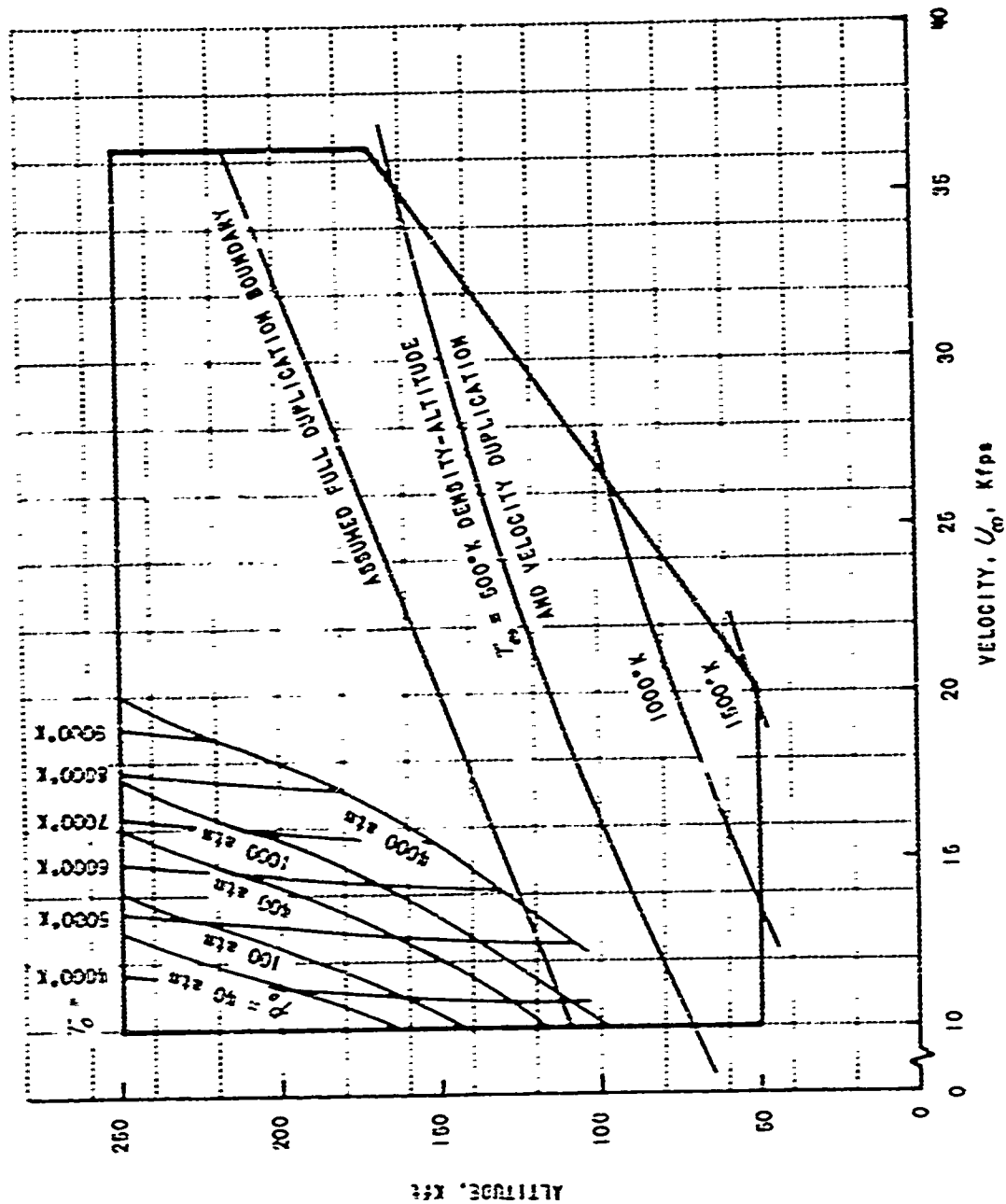


Fig. 2 Altitude-Velocity Map Showing Wind Tunnel Performance

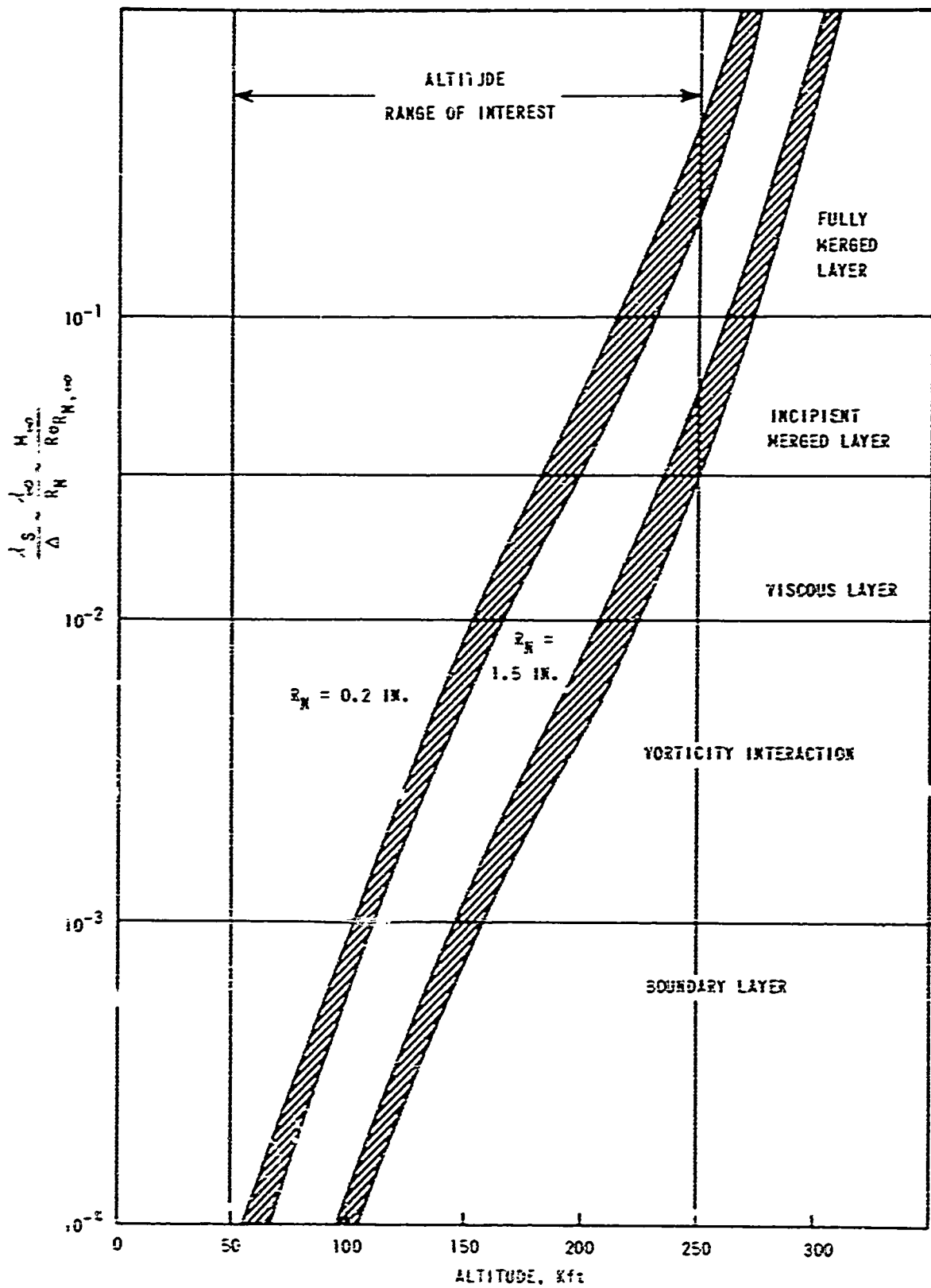


Fig. 3 Blunt-Nose Flow Regimes

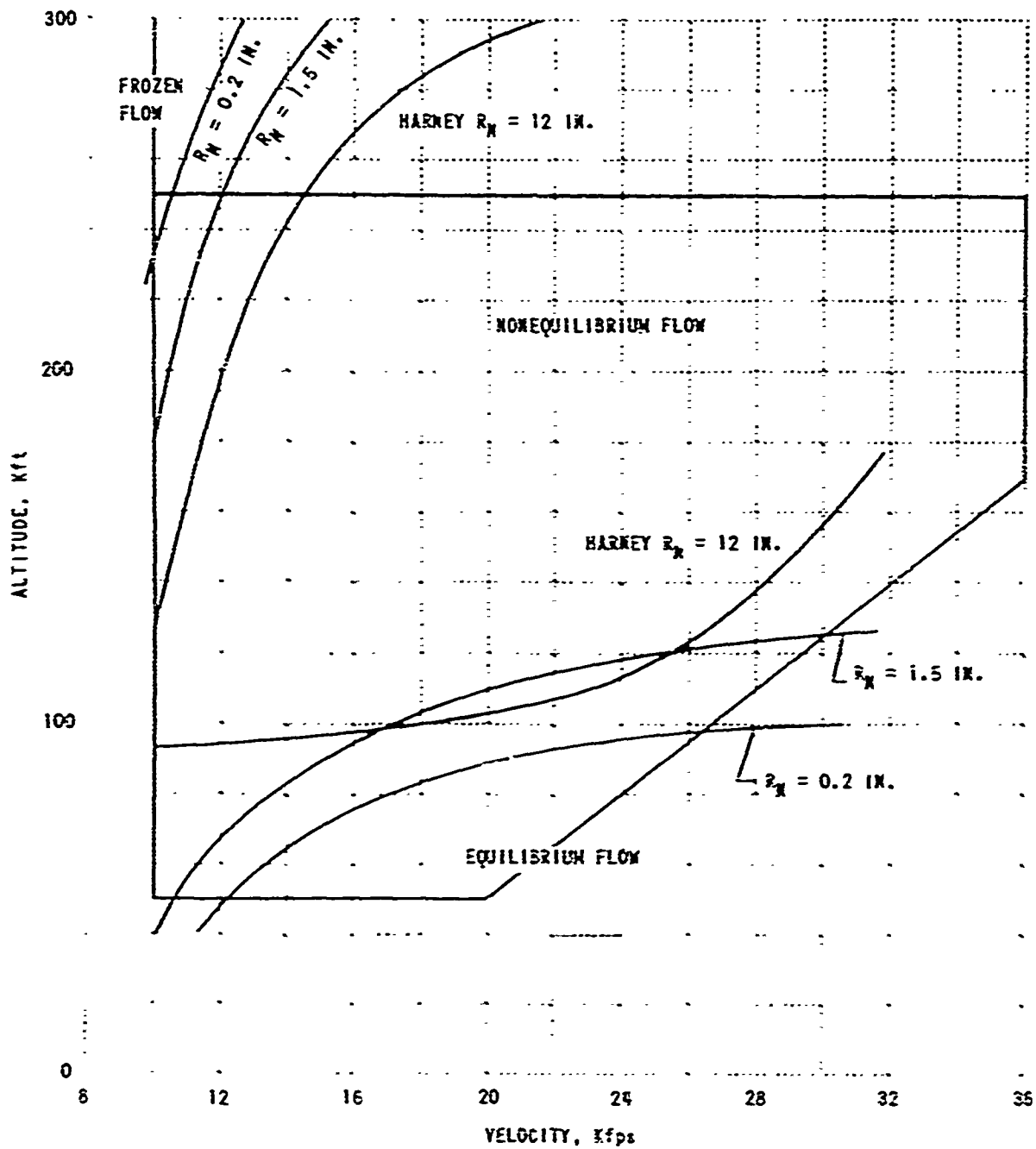


Fig. 4 Blunt-Nose Chemical-Kinetic Regimes

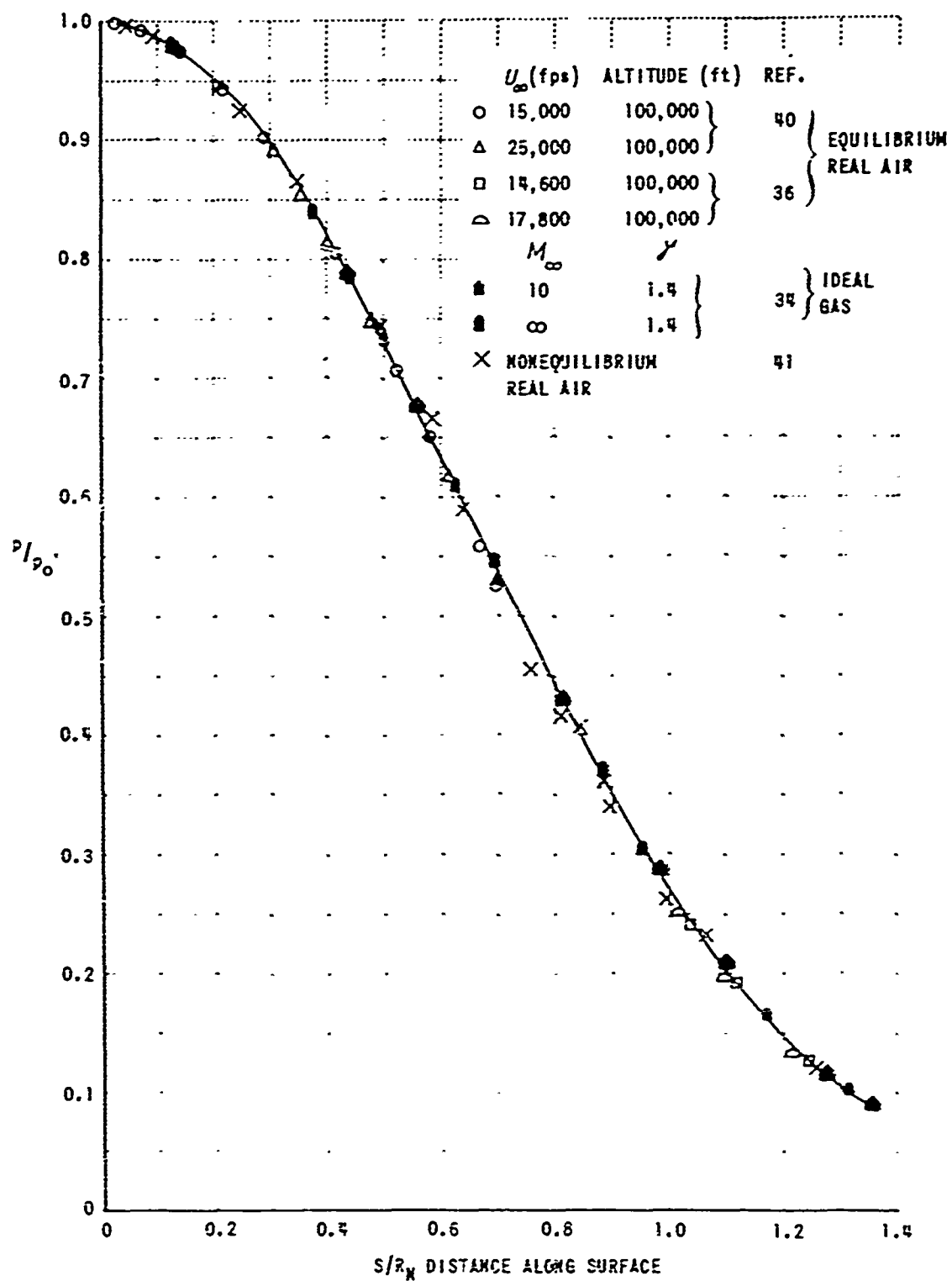


Fig. 5 Pressure Distribution on Spherical Nose

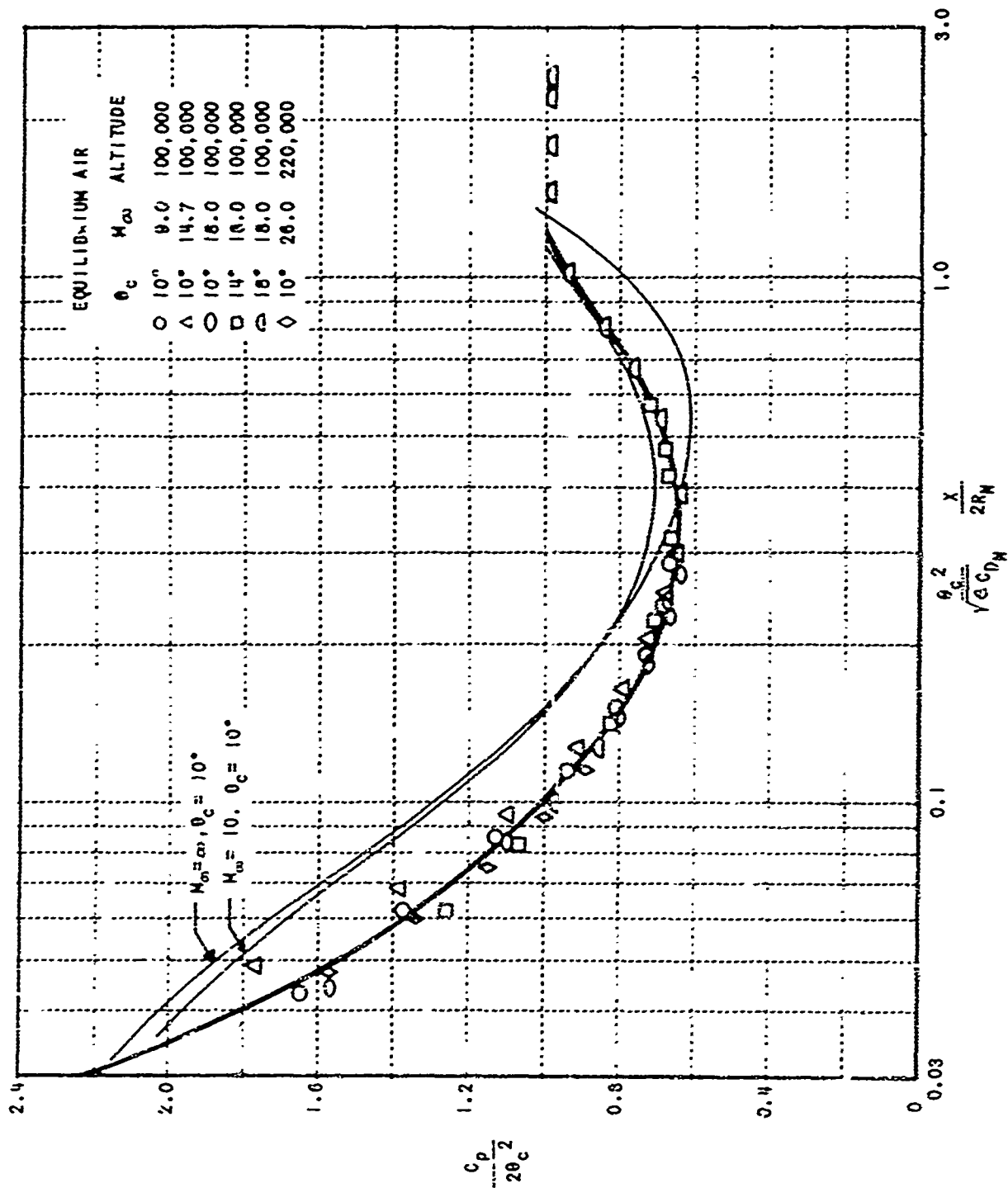


Fig. 6 Correlation of Ideal Gas and Real Air Pressure Distributions on Spherically Blunted Cones

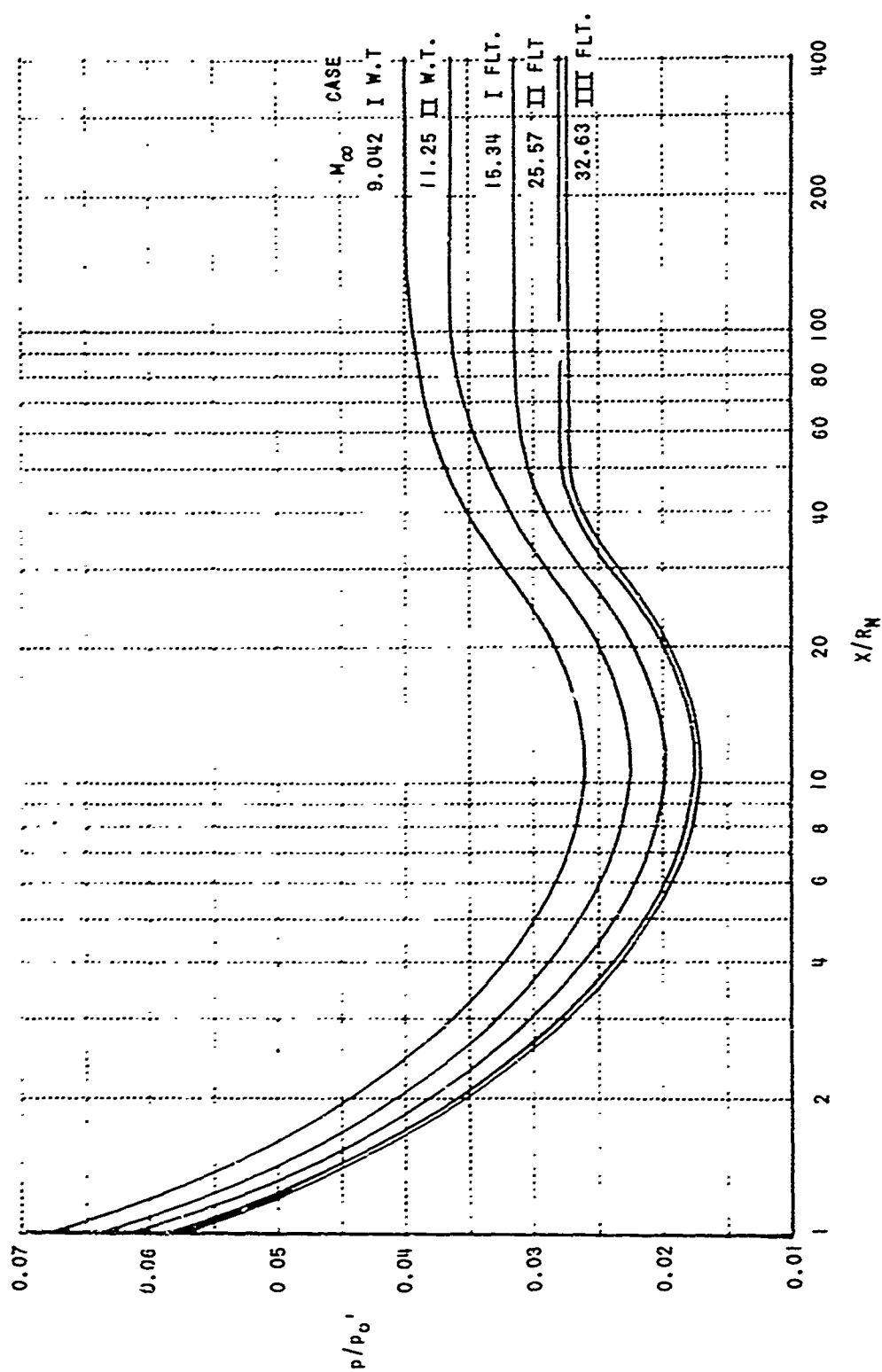


Fig. 7 Pressure Distribution Along Conical Afterbody at Various Free-Stream Mach Numbers

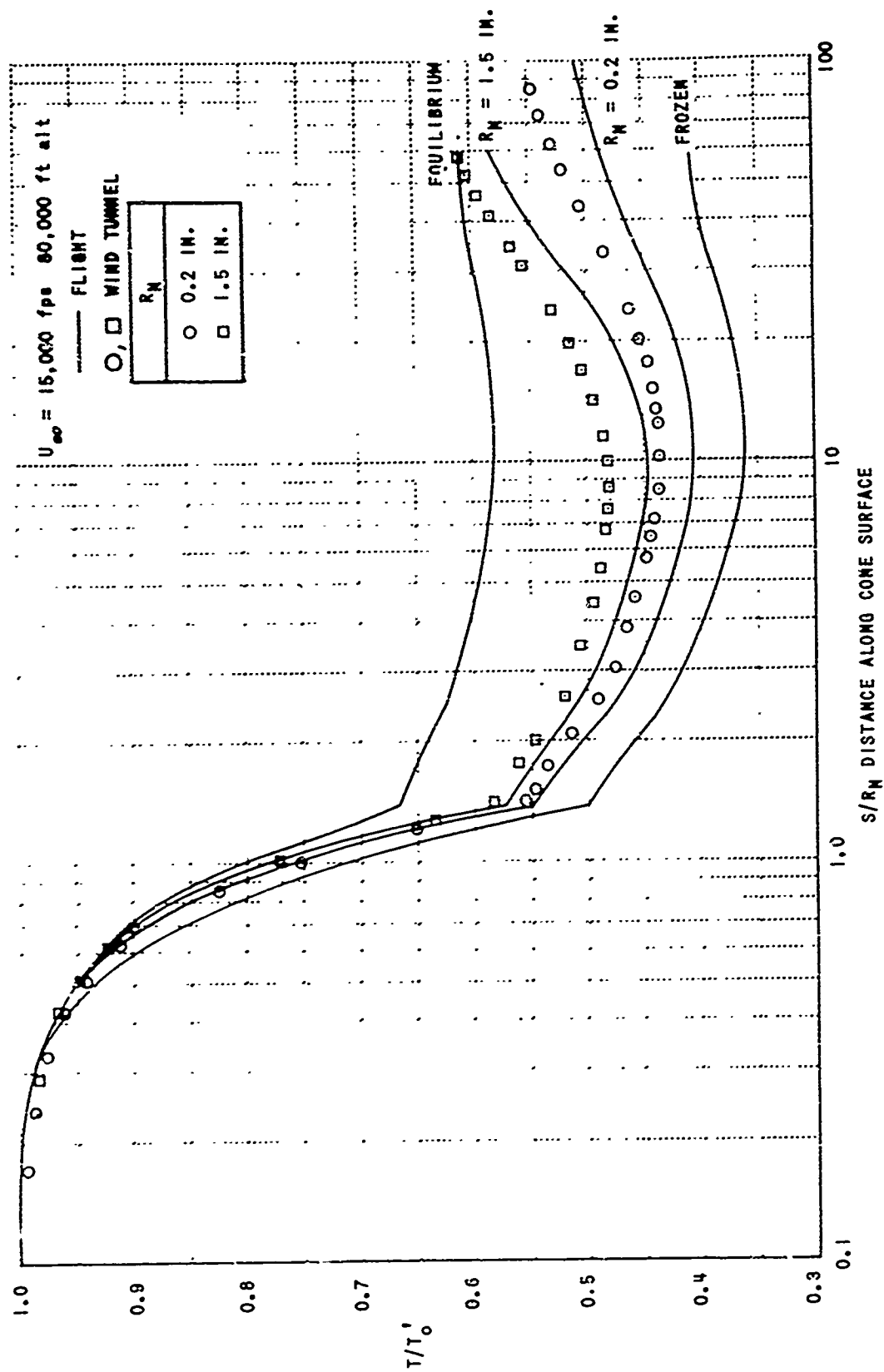
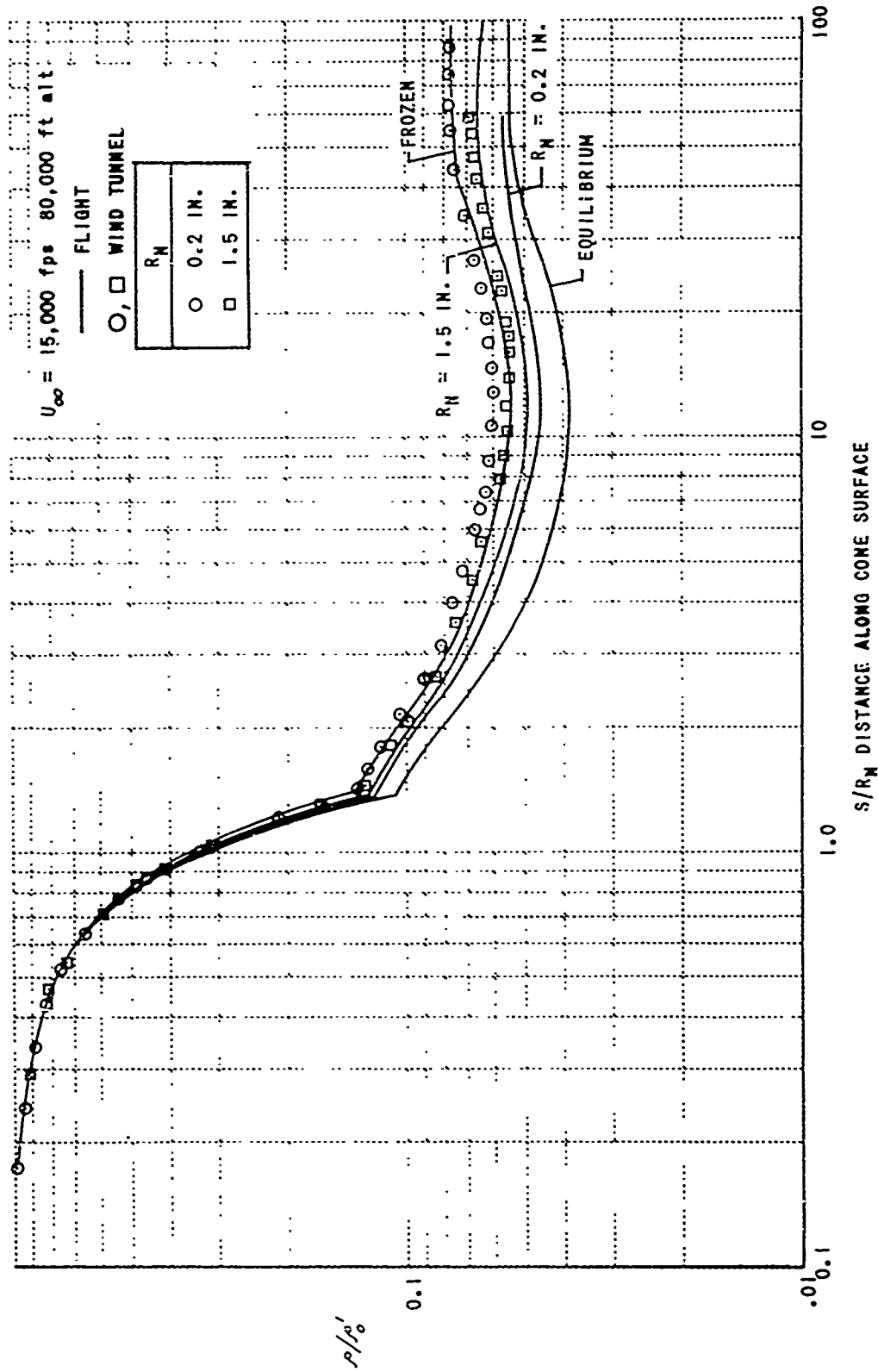


Fig. 8 Temperature Distribution on 9° Blunted Cone at $U_{\infty} = 15,000 \text{ fps}$

Fig. 9 Fig. 9 Density Distribution on 9° Blunted Cone at $U_\infty = 15,000$ fps

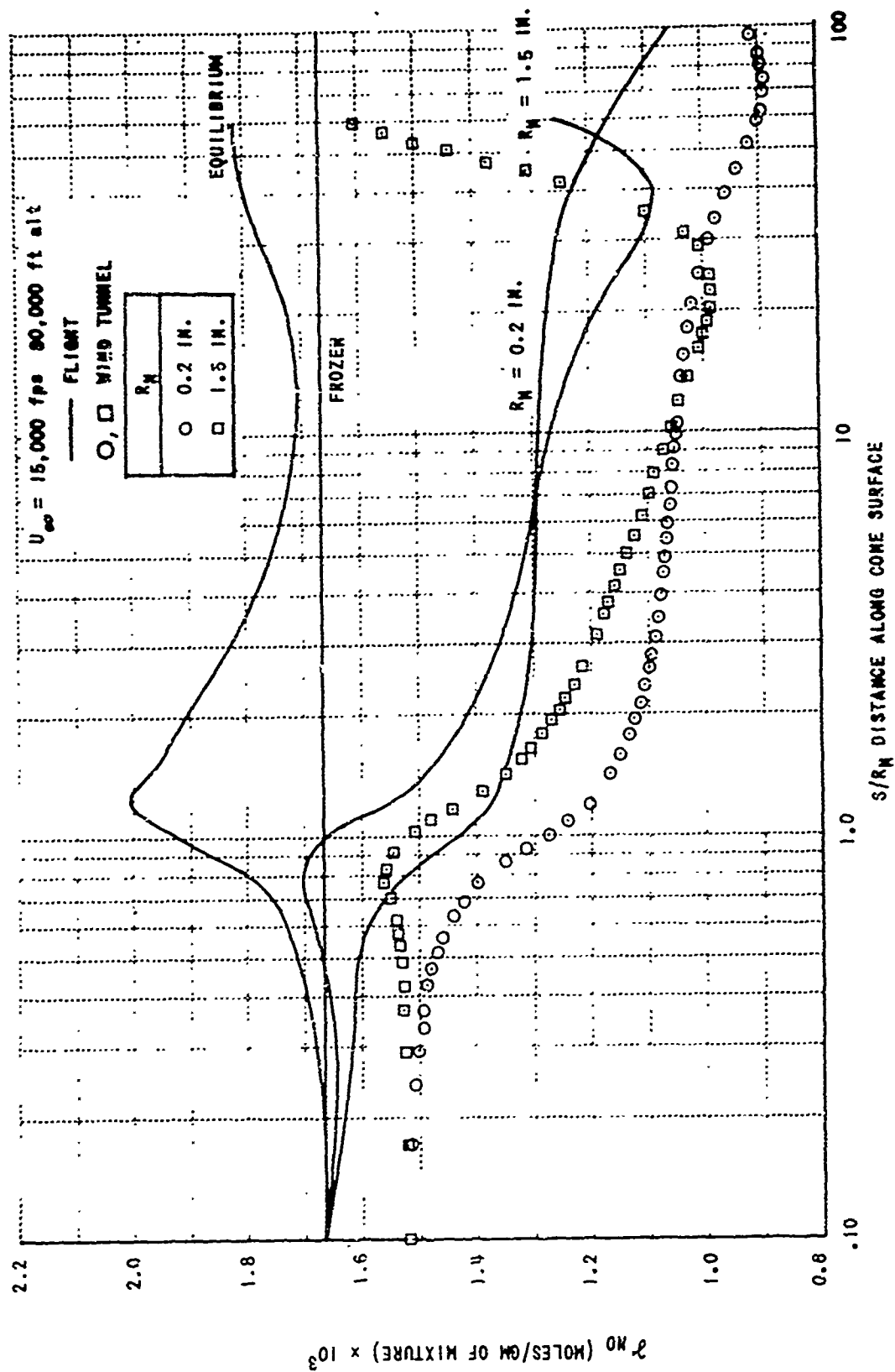
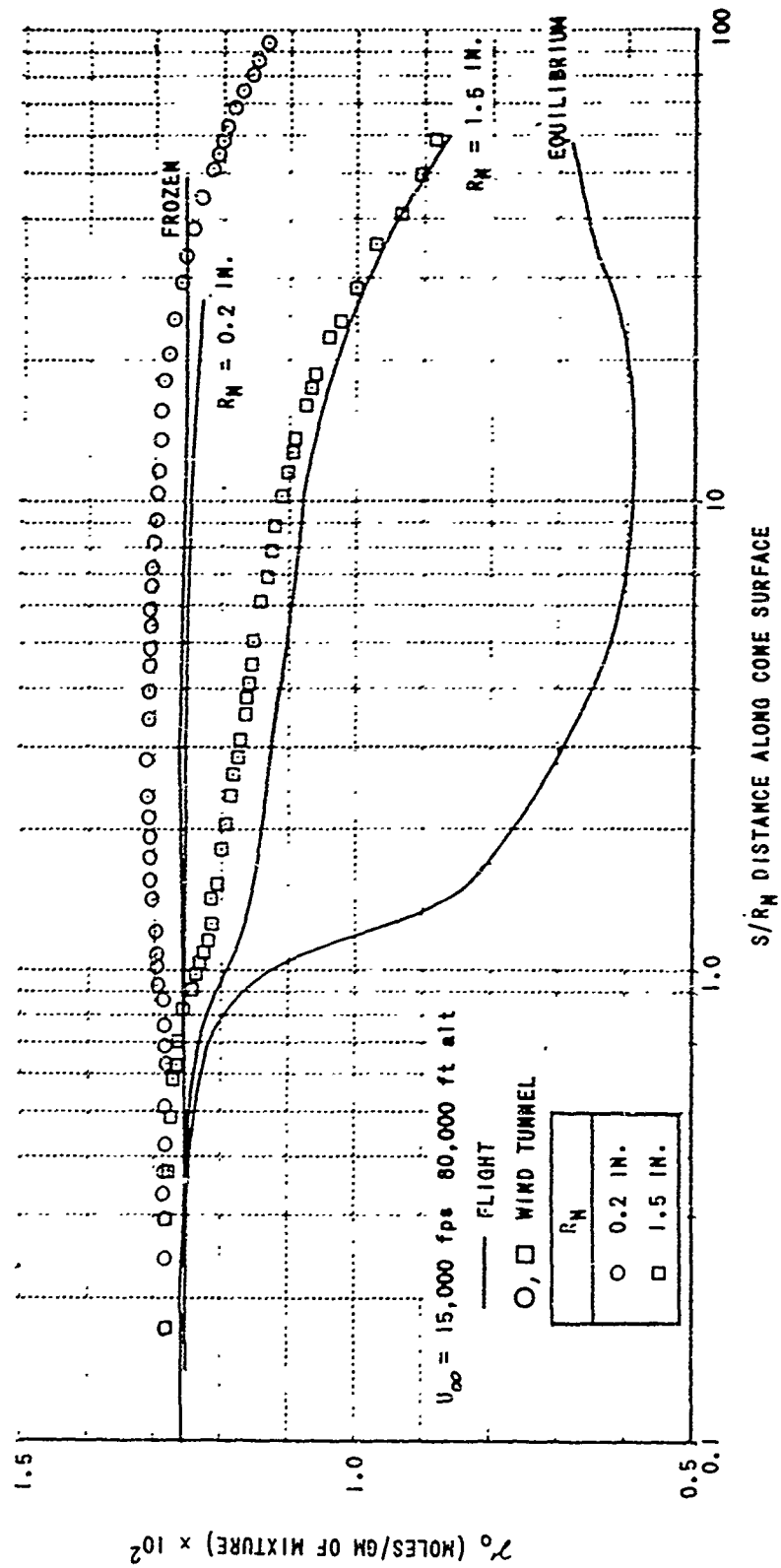


Fig. 10 Nitric Oxide Distribution on 9° Blunted Cone at $U_{\infty} = 15,000 \text{ fps}$

Fig. 11 Atomic Oxygen Distribution on 9° Blunted Cone at $U_\infty = 15,000 \text{ fps}$

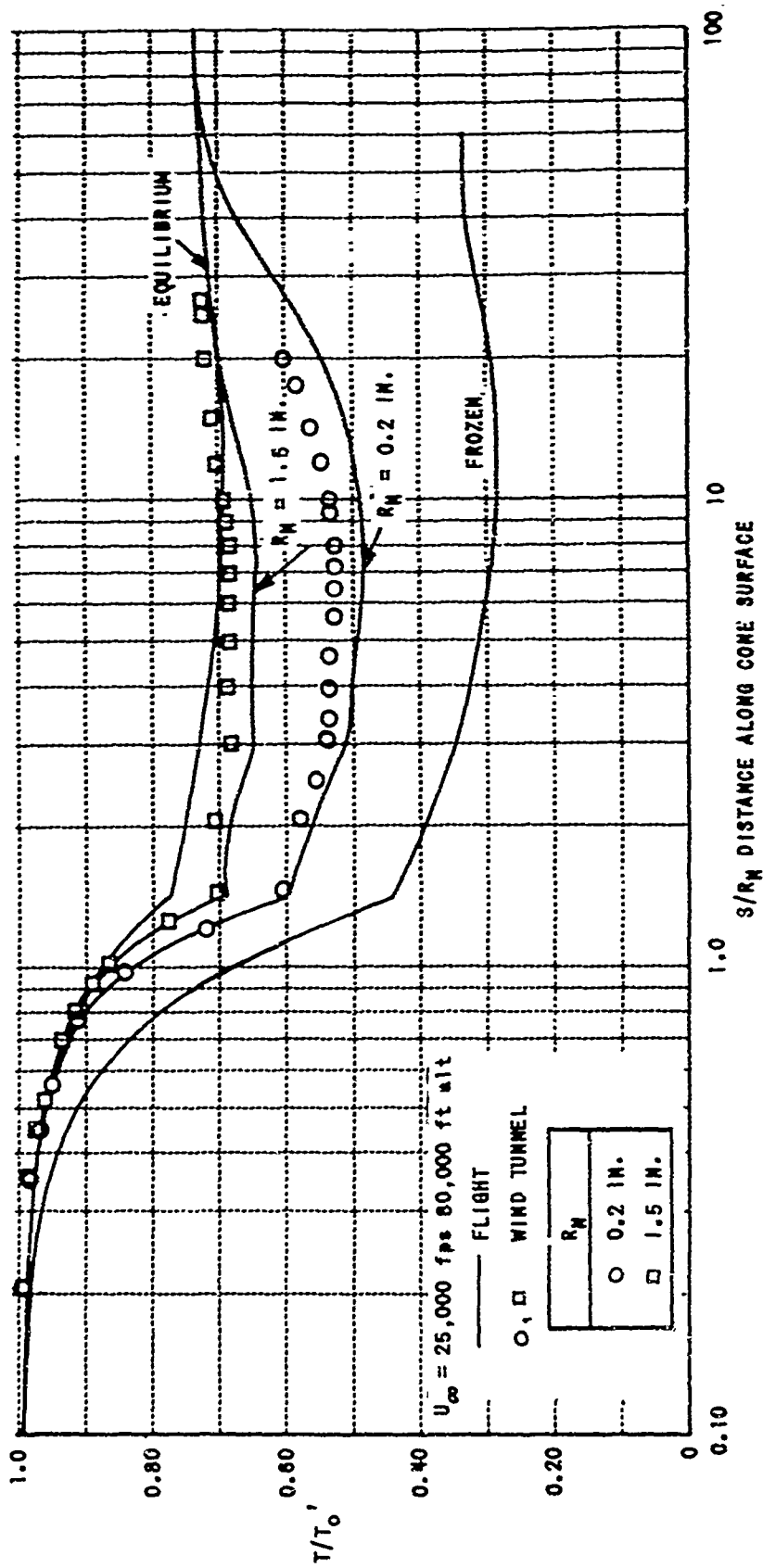
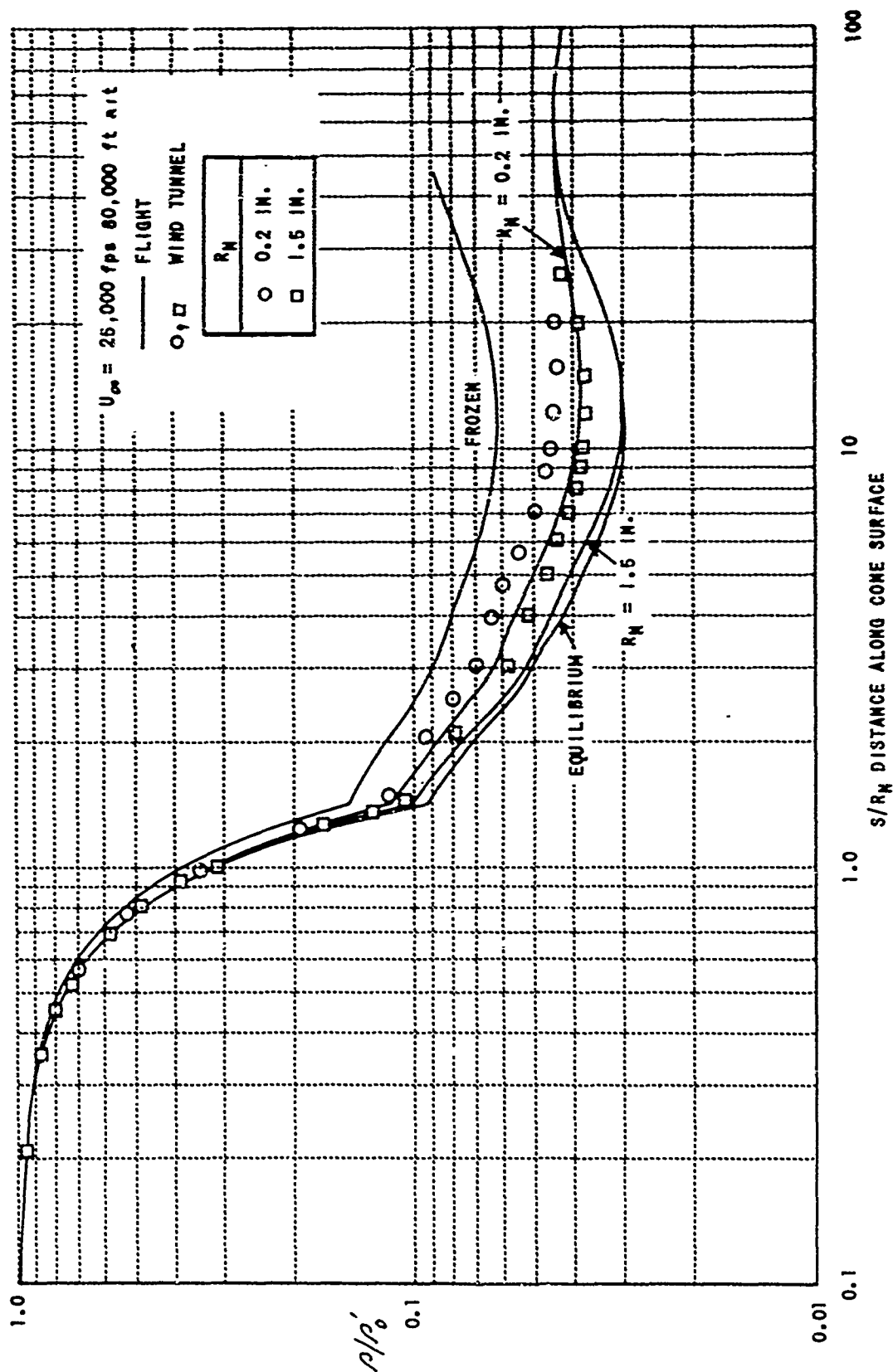


Fig. 12 Temperature Distribution on 9° Blunted Cone at $U_\infty = 25,000$ fps

Fig. 13 Density Distribution on 9° Blunted Cone at $U_\infty = 25,000$ fps

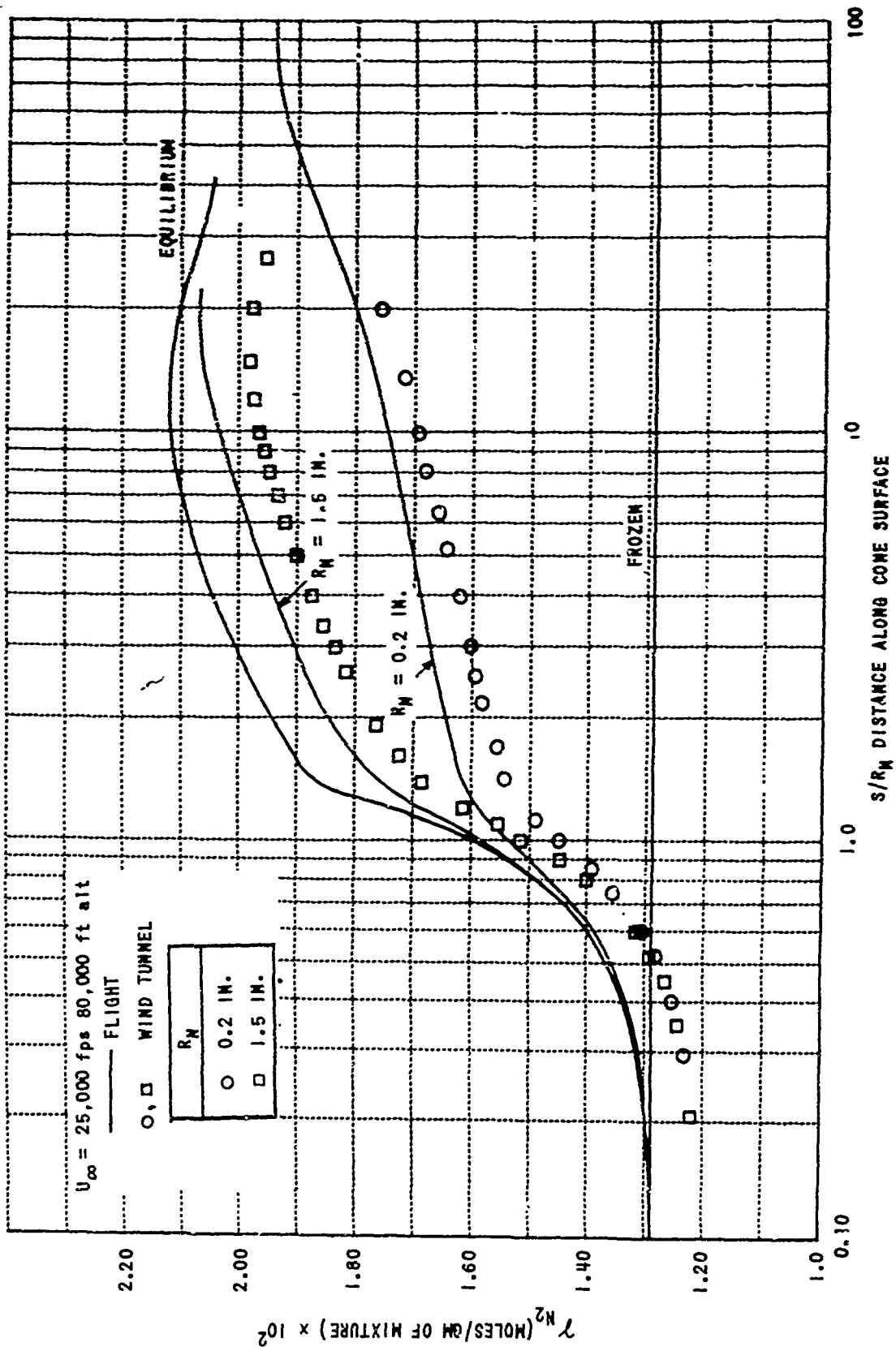
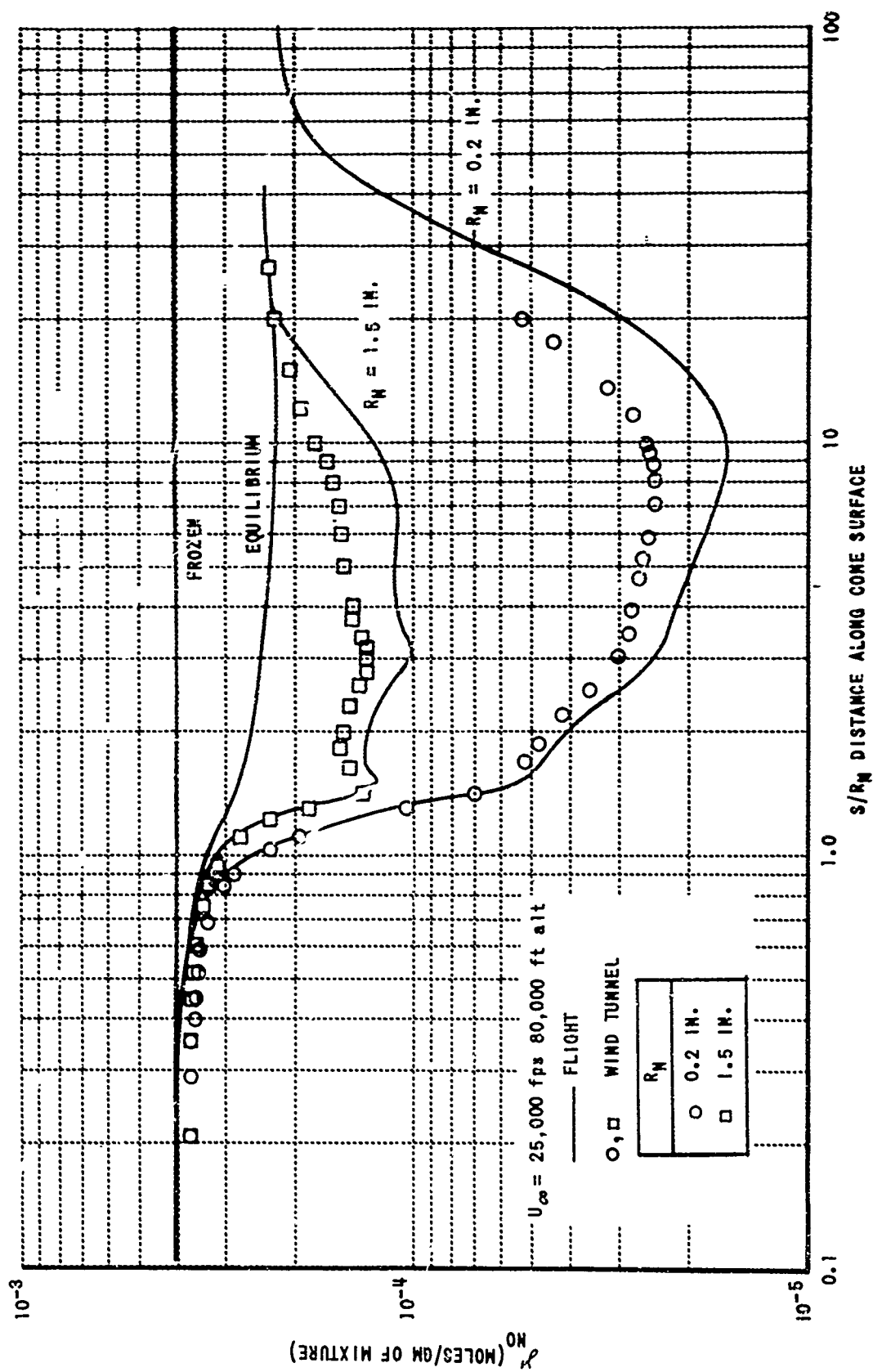
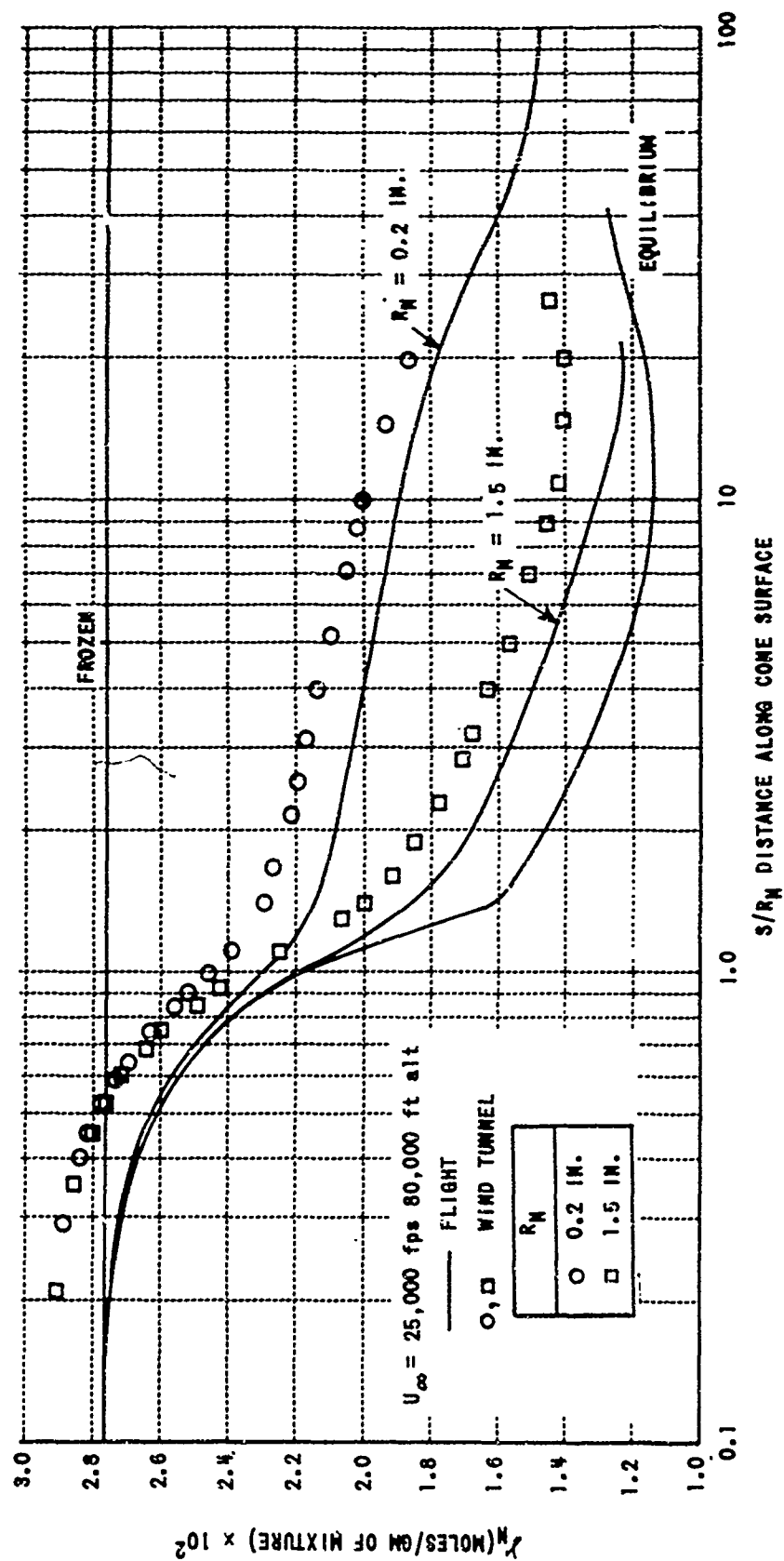
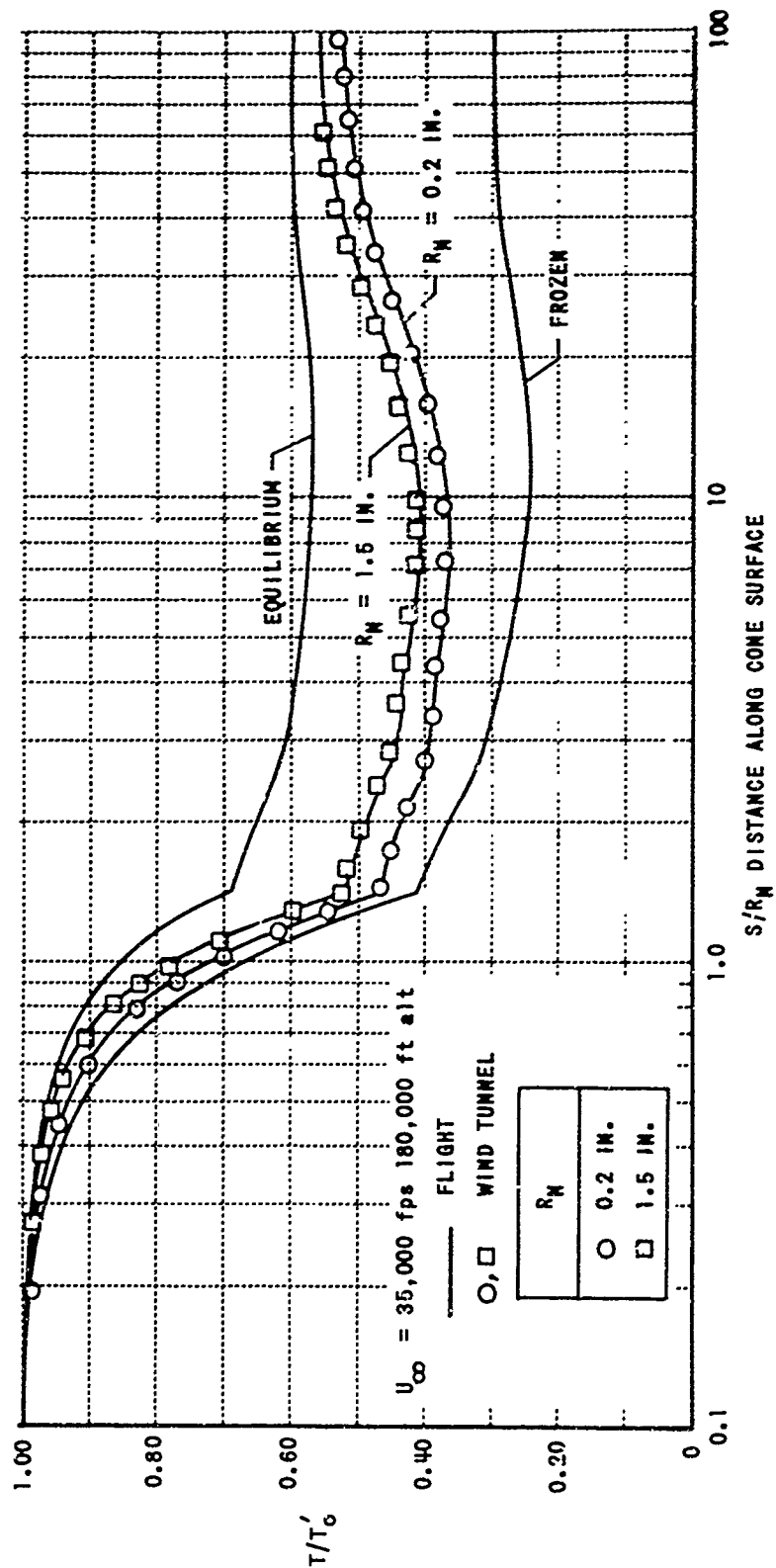


Fig. 14 Molecular Nitrogen Distribution on 9° Blunted Cone at $U_{\infty} = 25,000$ fps

Fig. 15 Nitric Oxide Distribution on 9° Blunted Cone at $U_\infty = 25,000$ fps

Fig. 16 Atomic Nitrogen Distribution on 9° Blunted Cone at U_∞ = 25,000 fps

Fig. 17 Temperature Distribution on 9° Blunted Cone at $U_\infty = 35,000 \text{ fps}$

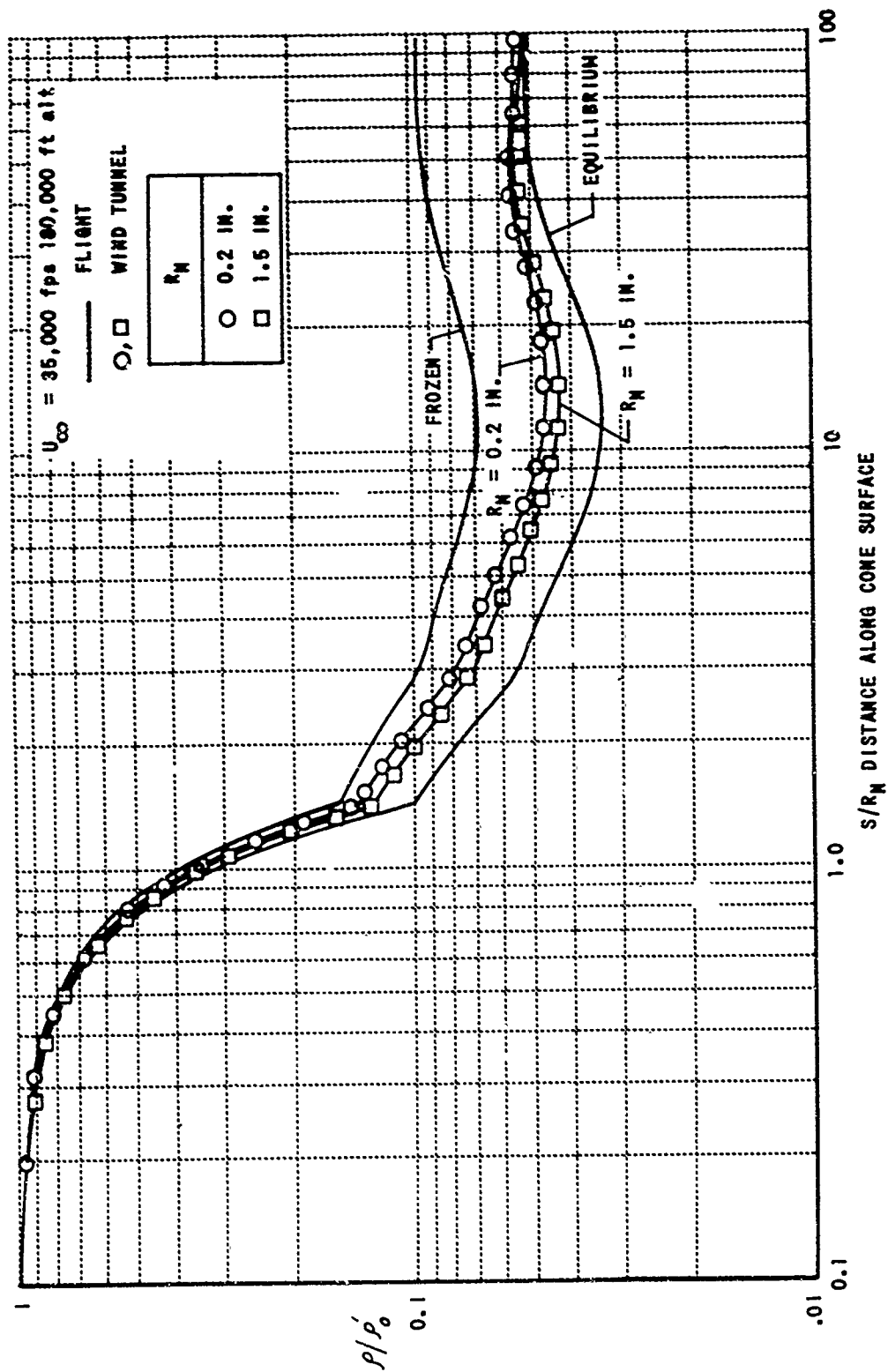
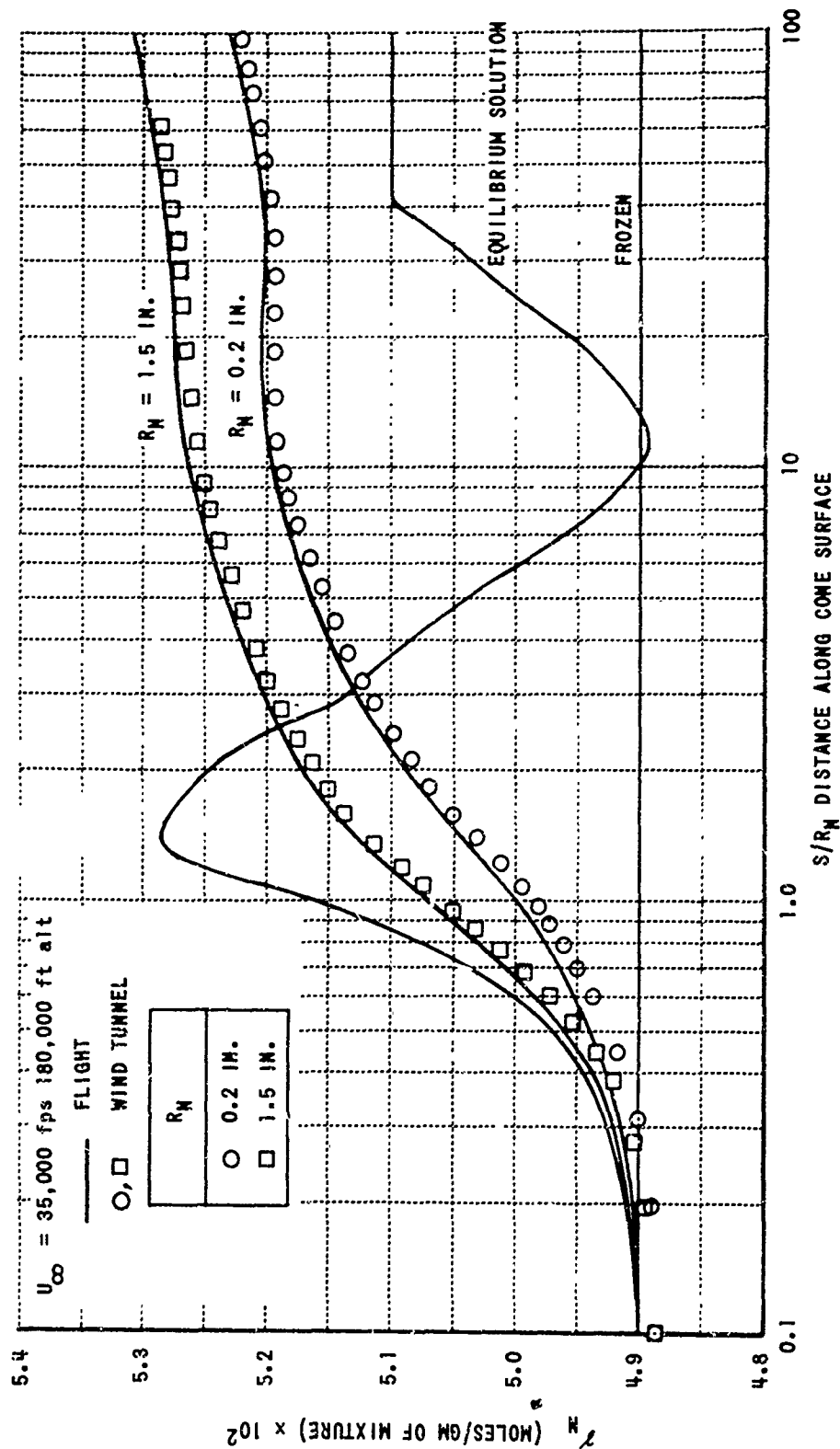
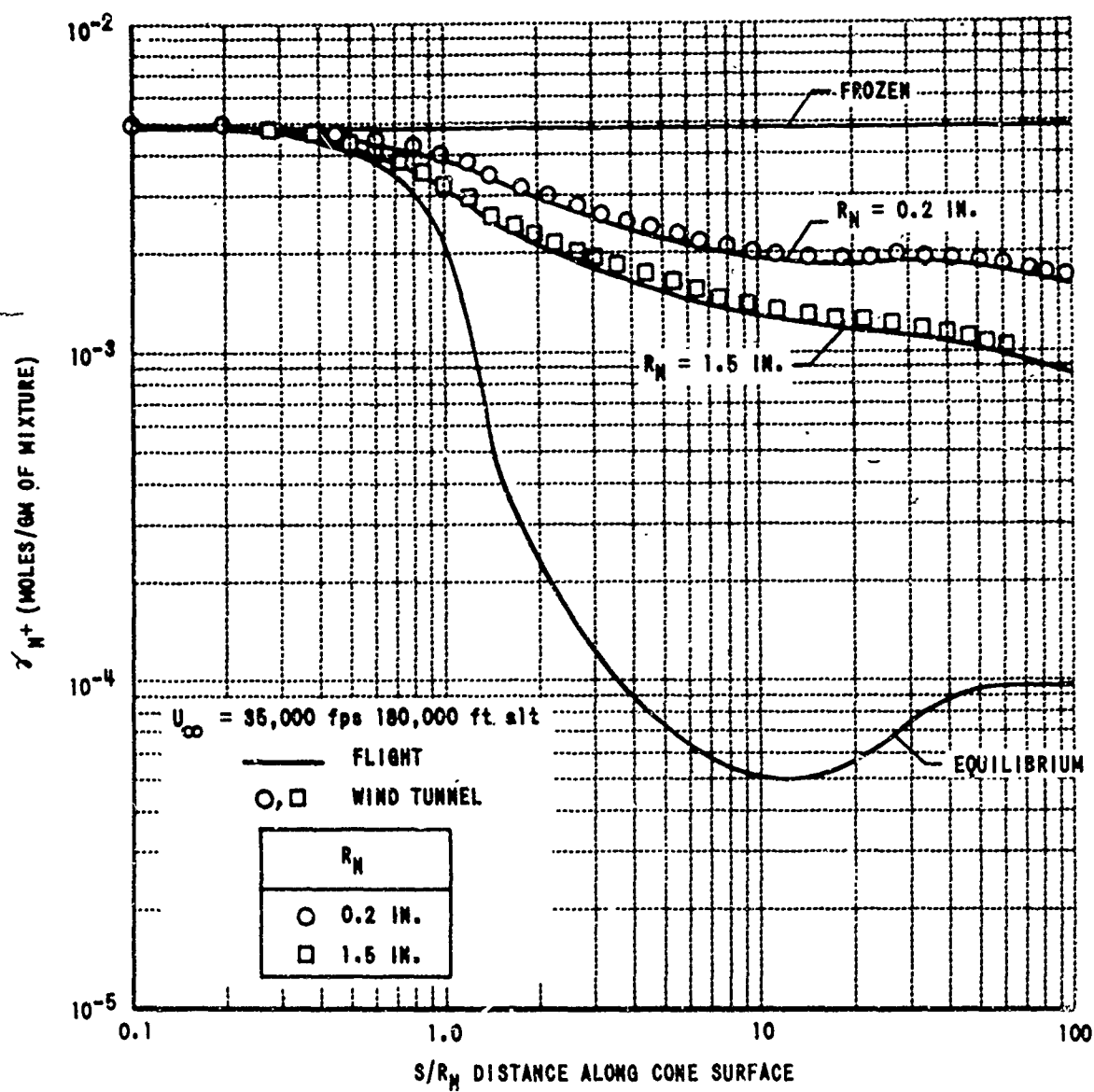
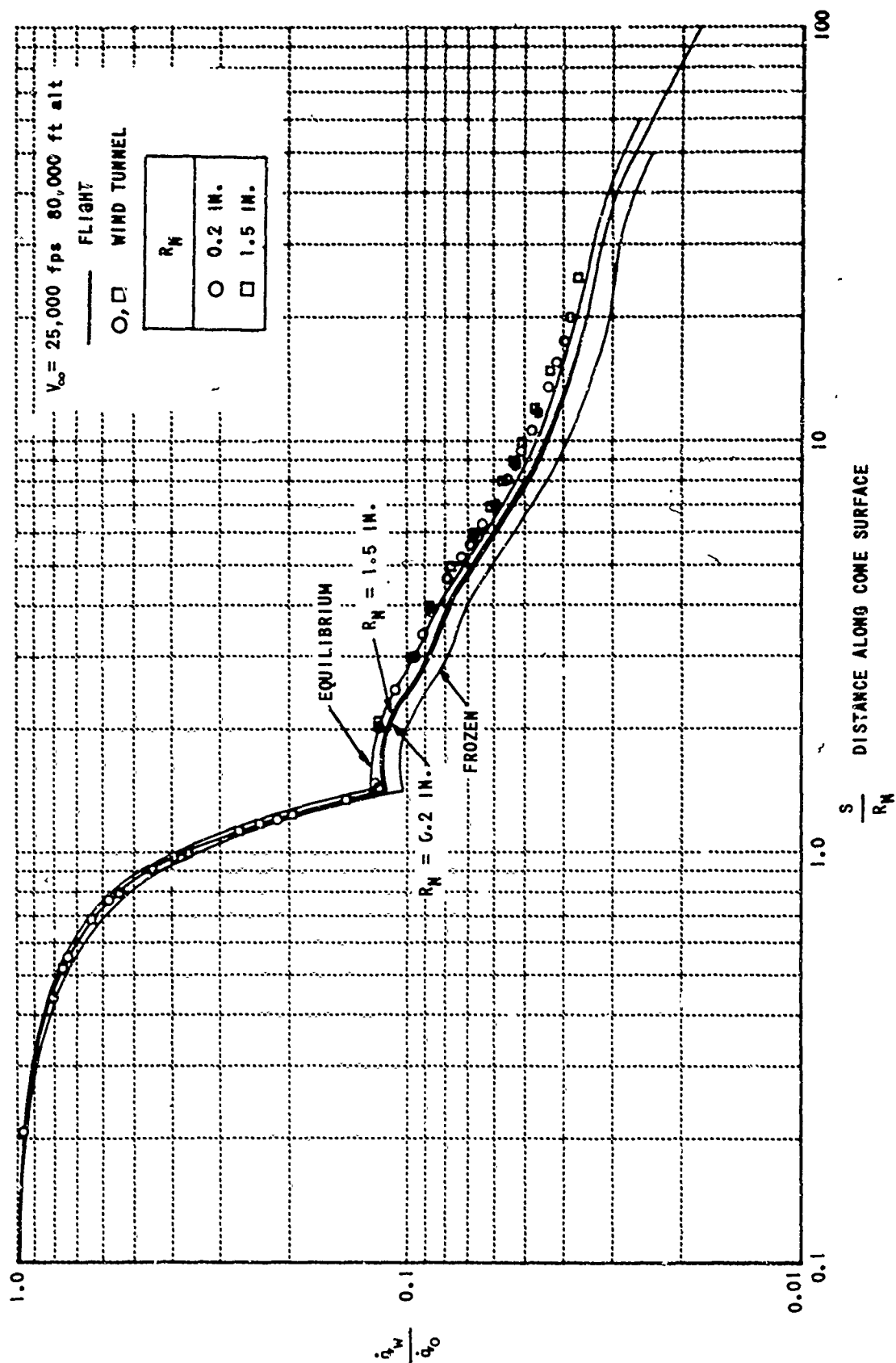


Fig. 18 Density Distribution on 9° Blunted Cone at $U_{\infty} = 35,000 \text{ fps}$

Fig. 19 Atomic Nitrogen Distribution on 9° Blunted Cone at $U_\infty = 35,000$ fps

Fig. 20 Atomic Nitrogen Ion Distribution on 9° Blunted Cone at $U_\infty = 35,000$ fps

Fig. 21a Comparison of Heat Transfer Distribution on 9° Blunted Cone at $U_\infty = 25,000$ fps

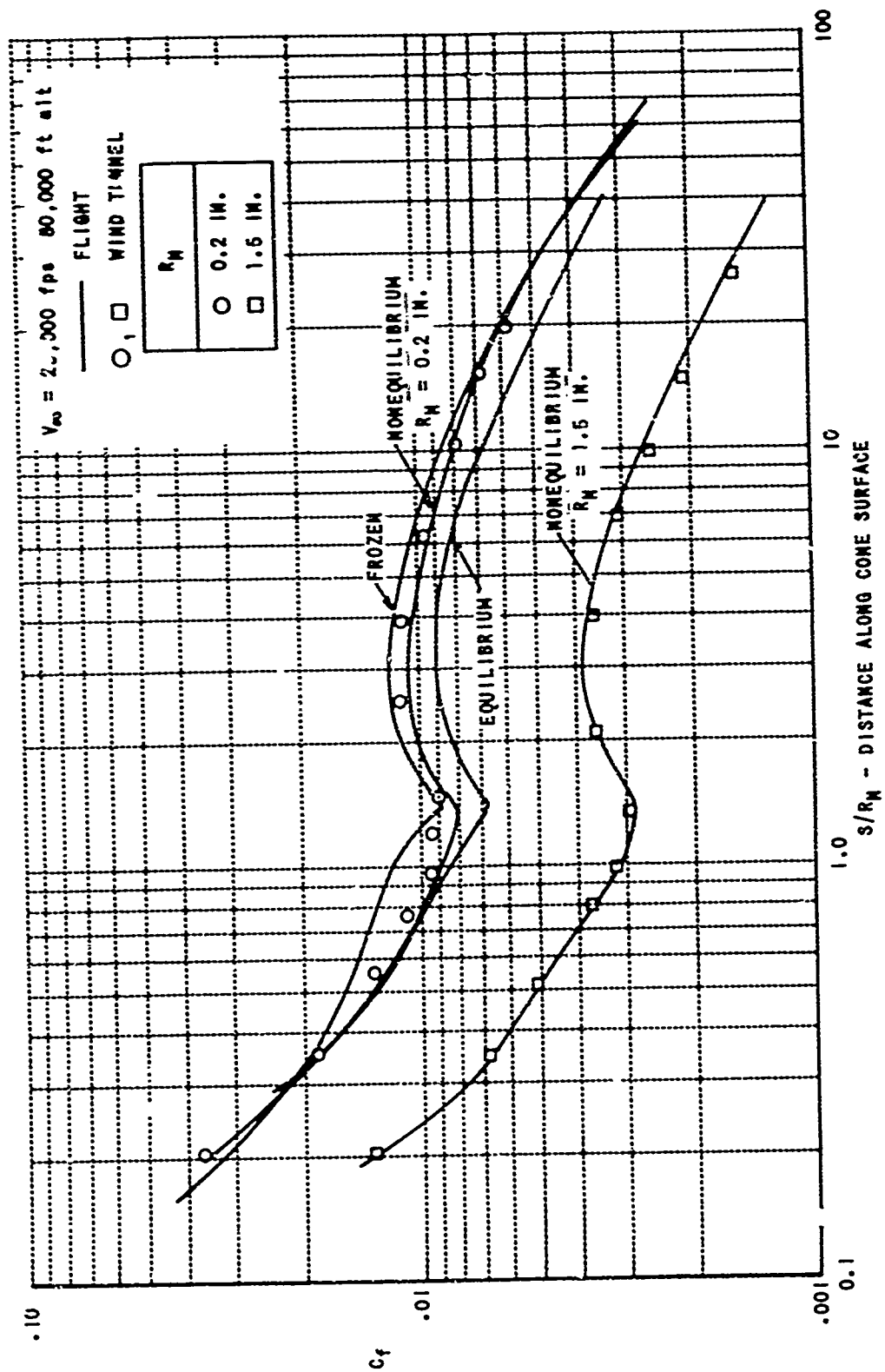
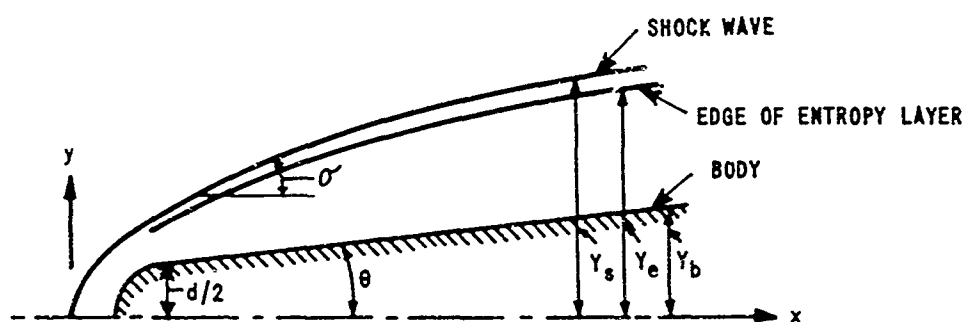


Fig. 21b Comparison of Skin Friction Distribution on 9° Blunted Cone at $U_\infty = 25,000 \text{ fps}$



FLOW ASSUMED PERFECT FOR $y_e < y < y_s$

WITHIN THE ENTROPY LAYER, $\rho \ll \rho_\infty$ AND $p \approx p_e$

Fig. 22 Schematic Representation of the Flow Field

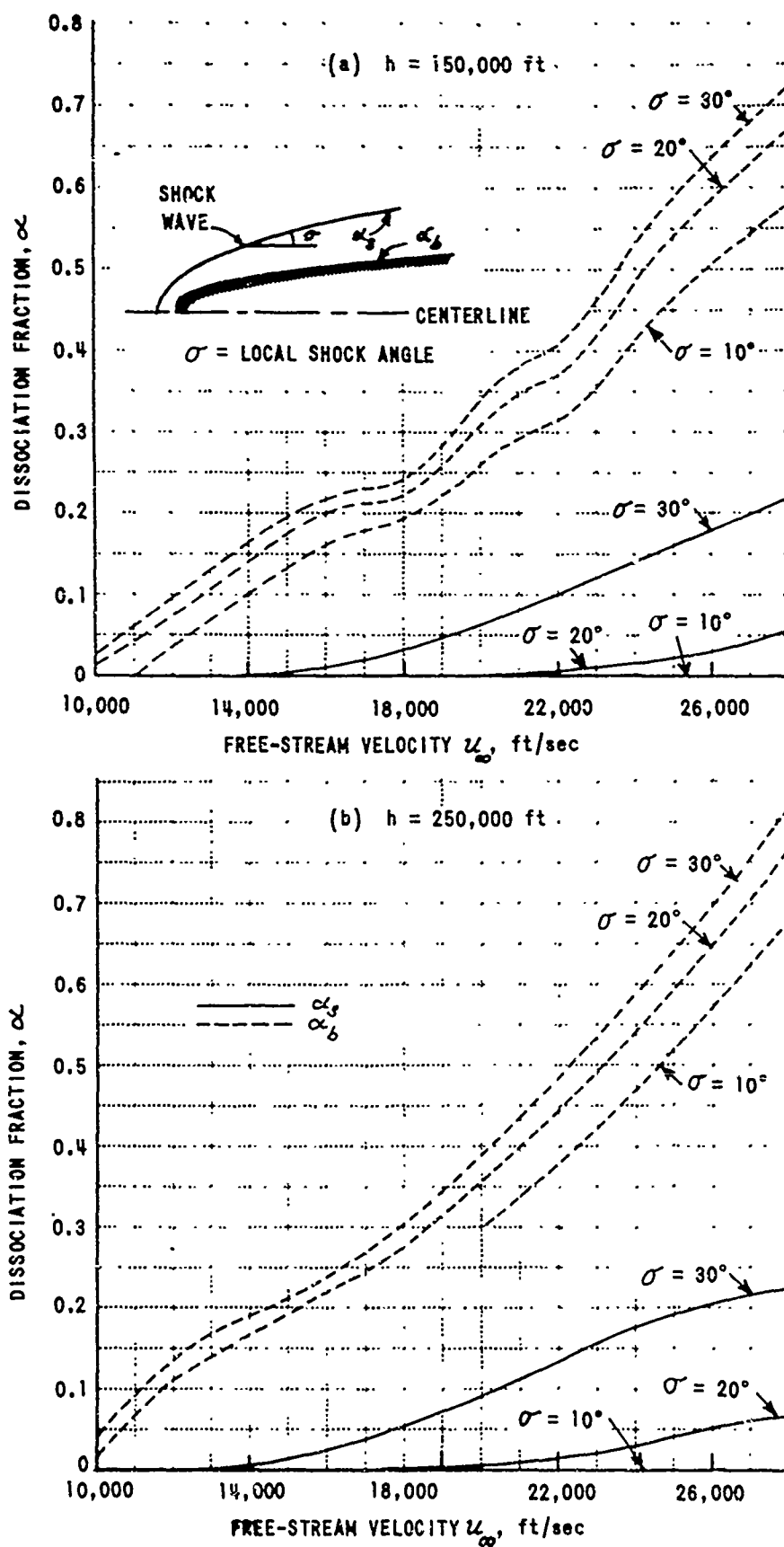


Fig. 23 Comparison of the Dissociation Fractions on the Body and Immediately Behind the Shock Wave for Equilibrium Flow

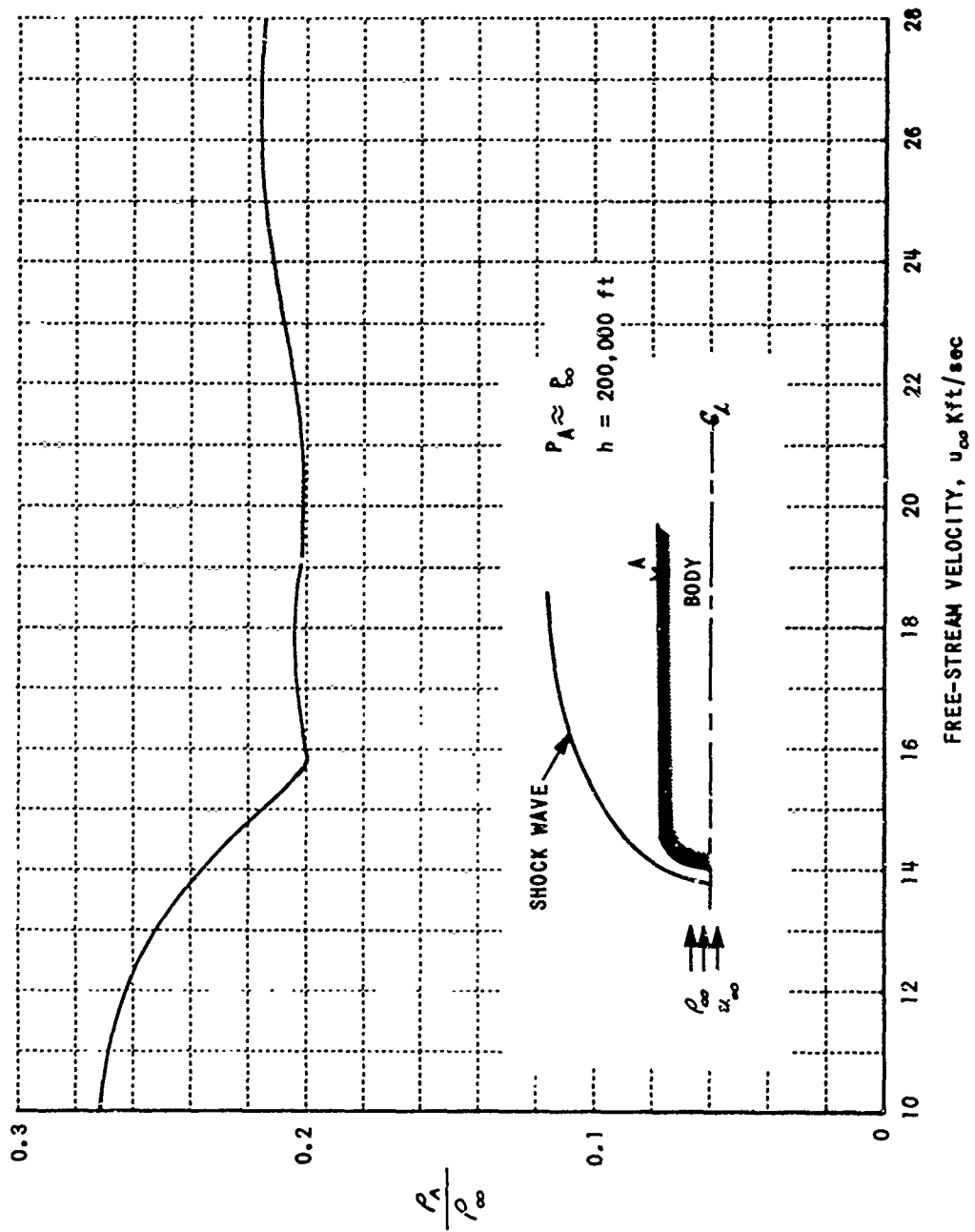


Fig. 24 Comparison of the Density on the Body with the Free-Stream Density

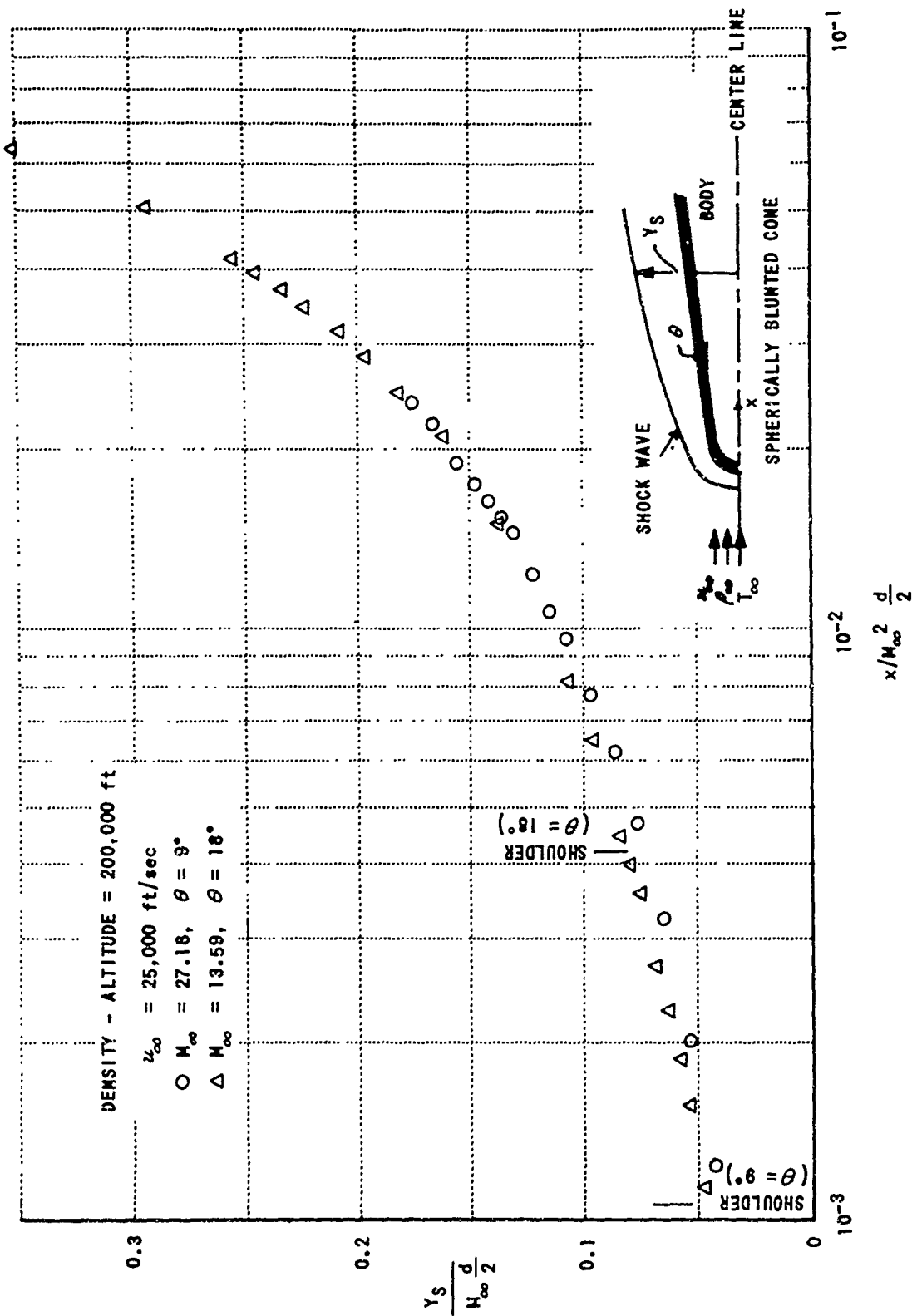


Fig. 25 Correlation of Shock Shapes in Real-Gas Flows when Free-Stream Temperature is not Duplicated

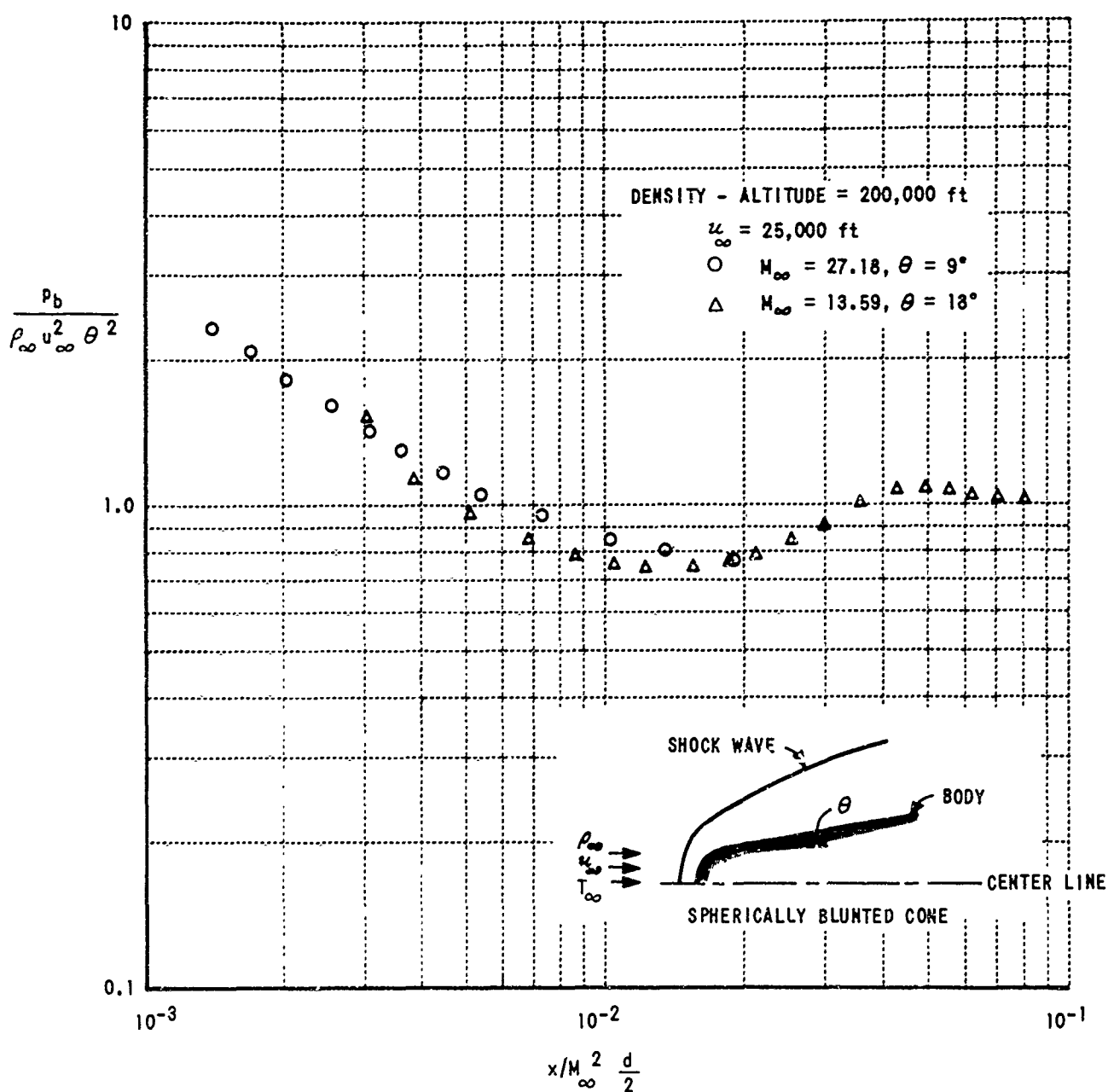


Fig. 26 Correlation of Surface Pressure Distributions for Equilibrium Flow when Free-Stream Temperature is not Duplicated

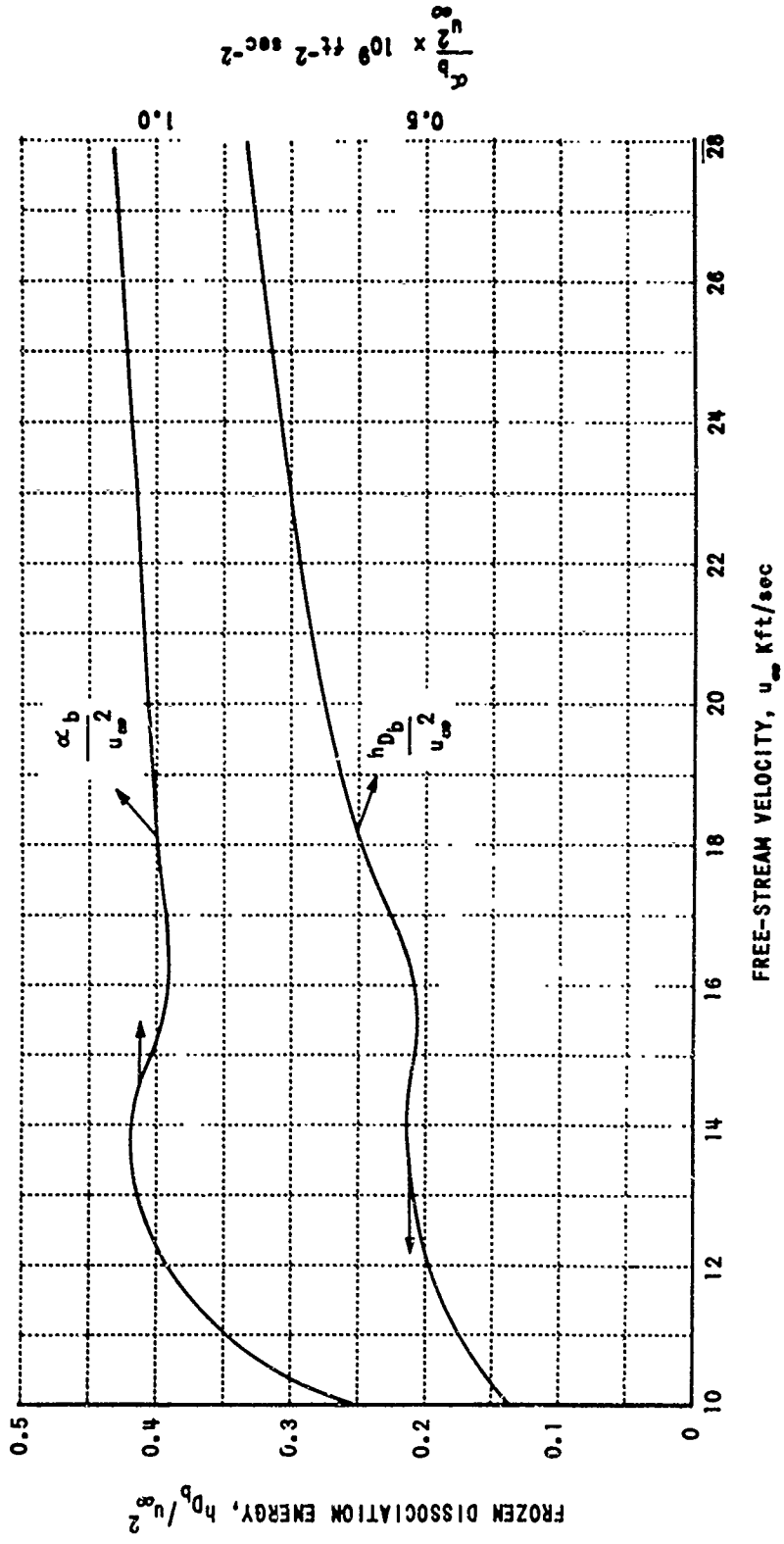


Fig. 27 Variation of the Dissociation Energy and Dissociation Fraction (in the Body Stream Tube) with Free-Stream Velocity for $h = 250,000$ ft

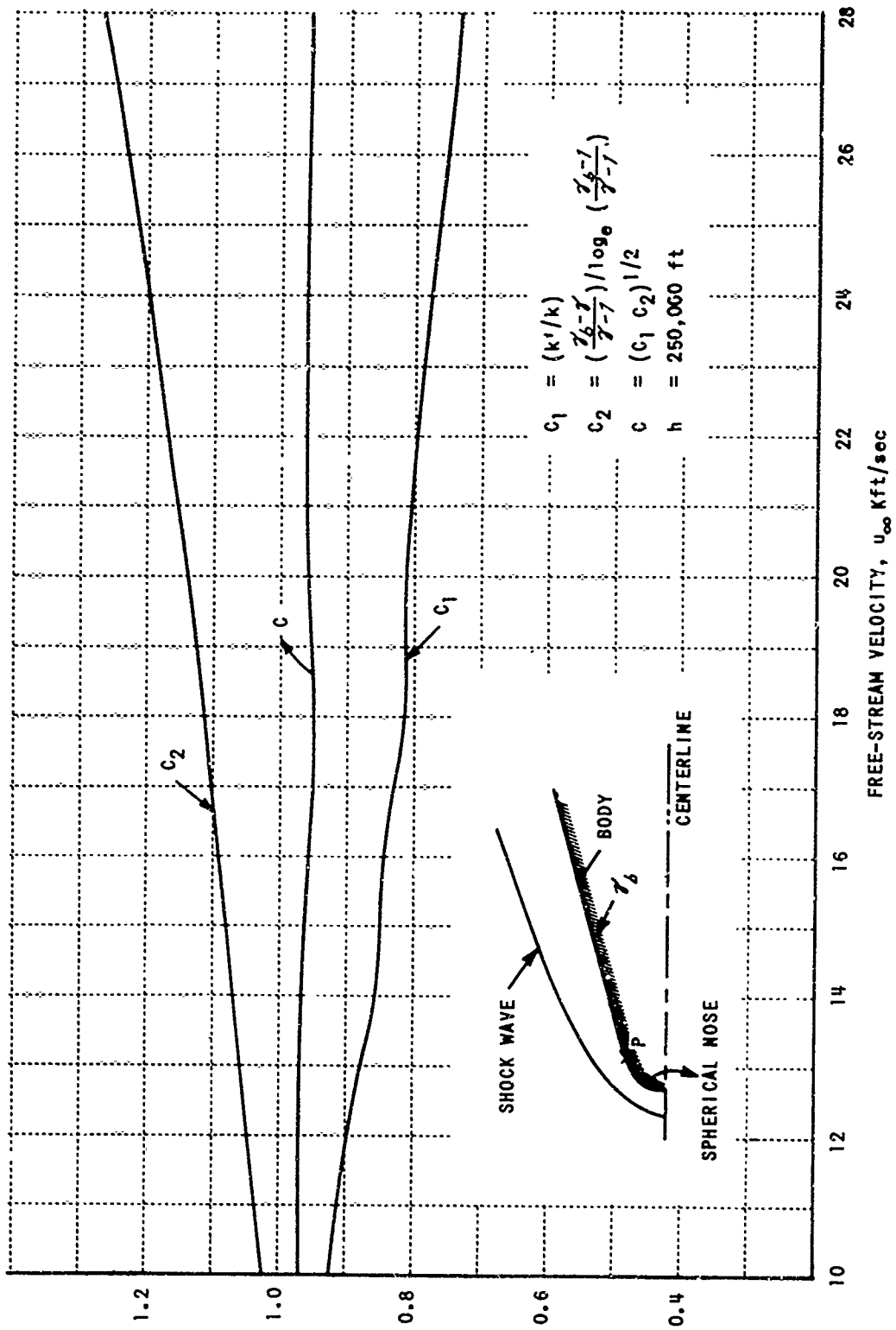


Fig. 28 Influence of Real-Gas Effects on the Downstream Influence of a Blunt Nose for a Spherically Blunted Slender Cone

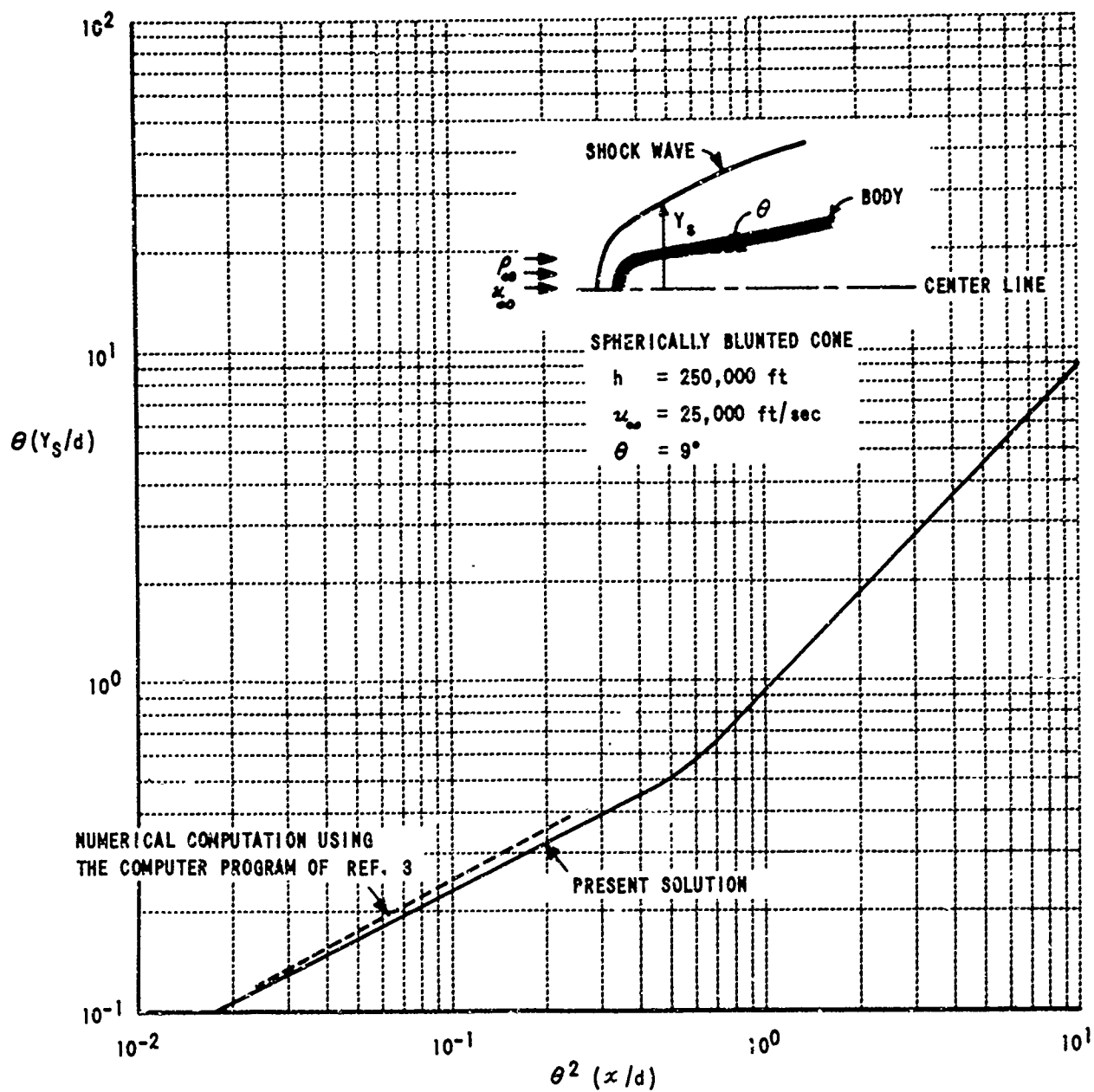


Fig. 29 Shock Shape for the Nonequilibrium Flow Past a Spherically Blunted Cone

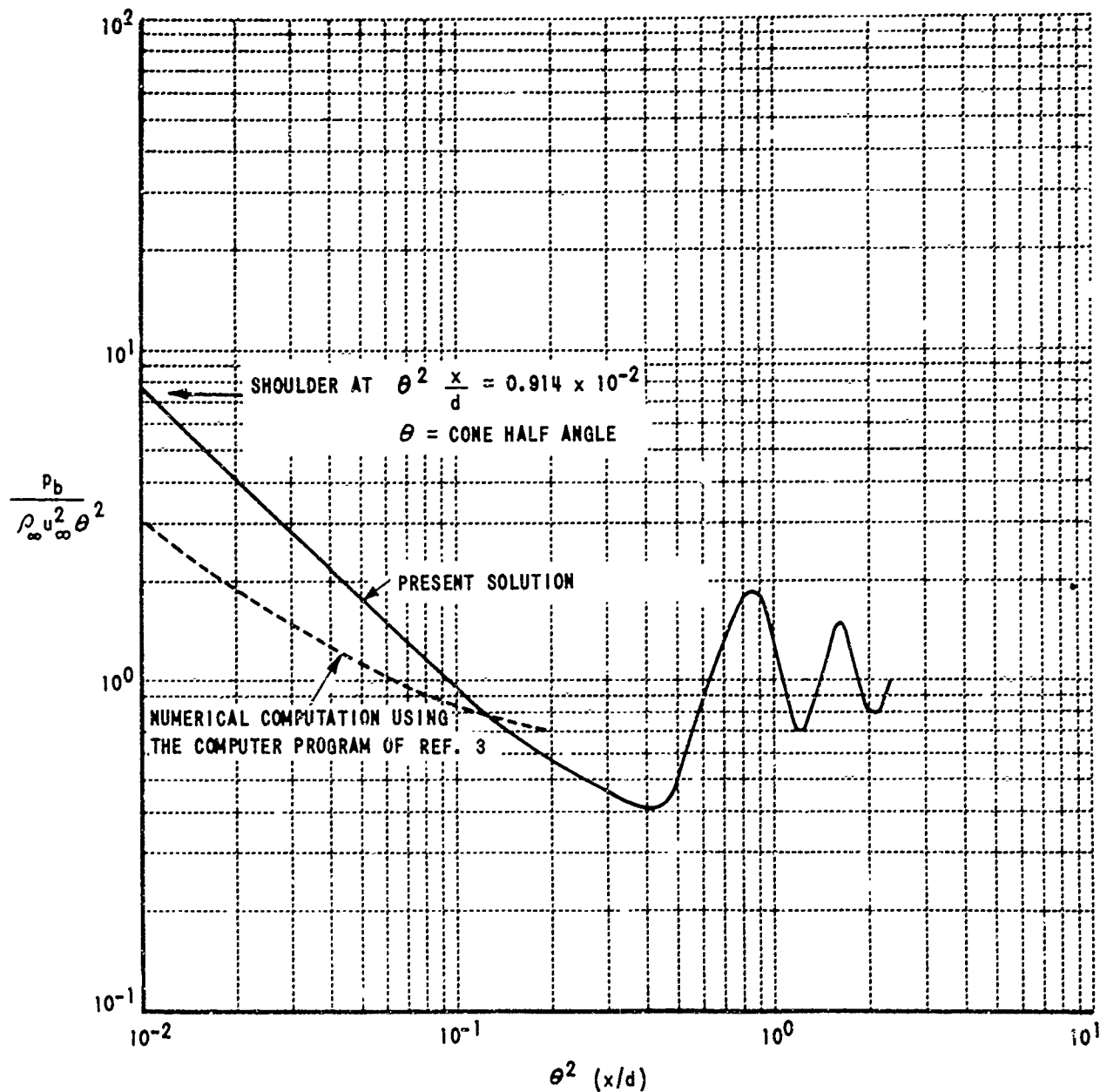


Fig. 30 Surface Pressure Distribution for the Nonequilibrium Flow Past a Spherically Blunted Cone

UNCLASSIFIED

Security Classification

DOCUMENT CONTROL DATA - R & D		
<i>(Security classification of title, body of abstract and indexing annotation must be entered when the overall report is classified)</i>		
1. ORIGINATING ACTIVITY (Corporate author) Cornell Aeronautical Laboratory, Inc. Buffalo, New York		2a. REPORT SECURITY CLASSIFICATION UNCLASSIFIED
		2b. GROUP N/A
3. REPORT TITLE A STUDY OF REAL-GAS EFFECTS ON BLUNTED CONE FLOWS		
4. DESCRIPTIVE NOTES (Type of report and inclusive dates) Final Report August 1966 through July 1968		
5. AUTHOR(S) (First name, middle initial, last name) C. E. Wittliff and T. R. Sundaram		
6. REPORT DATE January 1969	7a. TOTAL NO. OF PAGES 146	7b. NO. OF REFS 96
8a. CONTRACT OR GRANT NO AF40(600)-1131	9a. ORIGINATOR'S REPORT NUMBER(S) AEDC-TR-69-36	
b. PROJECT NO 5950		
c. Task 07	9b. OTHER REPORT NO(S) (Any other numbers that may be assigned this report) CAL Report No. AF-2081-A-2	
d. Program Element 63101F		
10. DISTRIBUTION STATEMENT This document is subject to special export controls and each transmittal to foreign governments or foreign nationals may be made only with prior approval of Arnold Engineering Development Center (AETS), Arnold Air Force Station, Tennessee 37389.		
11. SUPPLEMENTARY NOTES Available in DDC.		12. SPONSORING MILITARY ACTIVITY Arnold Engineering Development Center, Air Force Systems Command, Arnold AF Station, Tenn. 37389
13. ABSTRACT This report presents the results of a study of the combined effects of nose bluntness and real-gas phenomena on blunted slender body flows, with particular emphasis on the flows past spherically blunted cones. One of the primary objectives of the study has been to assess the effects of not matching all the similitude parameters in hypervelocity test flows about the slender bodies that are under consideration. In the first phase of the study, direct comparisons between the flight and wind-tunnel flow fields are made for a blunted slender cone for several flight cases by using a stream-tube computer program. In this part of the study the pressure distribution on the surface of the cone is assumed to be insensitive to nonequilibrium effects. In the second phase of the study, the influence of real-gas effects on blunted slender body flow fields is studied analytically by using a thin-shock-layer approach. It is found that real-gas effects on the pressure distribution and the shock shape for a blunted slender cone are small for the range of free-stream conditions of interest.		
This document is subject to special export controls and each transmittal to foreign governments or foreign nationals may be made only with prior approval of Arnold Engineering Development Center (AETS), Arnold Air Force Station, Tennessee 37389.		

DD FORM 1473
1 NOV 65UNCLASSIFIED
Security Classification

UNCLASSIFIED

Security Classification

14. KEY WORDS	LINK A		LINK B		LINK C	
	ROLE	WT	ROLE	WT	ROLE	WT
aerodynamic similitude						
hypersonic flow						
hypersonic wind tunnels						
frozen, equilibrium flow						
nonequilibrium flow						
boundary layers						

AFM
AF-11455 Form

UNCLASSIFIED

Security Classification